University of Massachusetts Amherst

ScholarWorks@UMass Amherst

Doctoral Dissertations

Dissertations and Theses

June 2021

ENGINEERING ADVANCED MATERIAL PROPERTIES FOR POLYMERIC MATERIALS THROUGH MISCIBLE AND IMMISCIBLE ADDITIVES

Chinmay M. Saraf
University of Massachusetts Amherst

Follow this and additional works at: https://scholarworks.umass.edu/dissertations_2

Part of the Polymer and Organic Materials Commons

ENGINEERING ADVANCED MATERIAL PROPERTIES FOR POLYMERIC MATERIALS THROUGH MISCIBLE AND IMMISCIBLE ADDITIVES

A Dissertation Presented

by

CHINMAY MANGESH SARAF

Submitted to the Graduate School of the
University of Massachusetts Amherst in partial fulfillment
of the requirements for the degree of

DOCTOR OF PHILOSOPHY

May 2021

Polymer Science and Engineering

ENGINEERING ADVANCED MATERIAL PROPERTIES FOR POLYMERIC MATERIALS THROUGH MISCIBLE AND IMMISCIBLE ADDITIVES

A Dissertation Presented

by

CHINMAY MANGESH SARAF

Approved as to style and content by:

_____

Alan J. Lesser, Chair

_____

E. Bryan Coughlin, Member

_____

Jae-Hwang Lee, Member

_____

David Hoagland, Department Head

Polymer Science and Engineering

DEDICATION

To my family for their unconditional support

ACKNOWLEDGEMENTS

ABSTRACT

ENGINEERING ADVANCED MATERIAL PROPERTIES FOR POLYMERIC MATERIALS THROUGH MISCIBLE AND IMMISCIBLE ADDITIVES

May 2021

CHINMAY MANGESH SARAF

Int. M.Tech., INDIAN INSTITUTE OF TECHNOLOGY ROORKEE

M.S., UNIVERSITY OF MASSACHUSETTS AMHERST

Ph.D., UNIVERSITY OF MASSACHUSETTS AMHERST

Directed by: Prof. Alan J. Lesser

This dissertation focuses on engineering polymeric formulations using additives to achieve advanced material properties. Additives provide an economic and convenient route to obtain specific material properties suitable for a given application without the need for cumbersome and precise synthesis. Specifically, this work demonstrates the use of strategically selected additives or novel processes to addresses three key challenges associated with widely used commercial polymers. First, we develop photo-curable resins for the impact modification of SLA printed glassy acrylate thermosets by taking advantage of immiscible polymeric additives. Second, we investigate the next-generation impact modification for semicrystalline thermoplastics using immiscible block copolymeric additives. Lastly, we study the fortification and flame-retardance for glassy epoxy thermosets using miscible molecular additives.

In the first chapter, we discuss state-of-the-art impact modification for semi-crystalline and glassy polymers. This chapter describes key factors that transpire into a brittle failure for polymeric materials, such as, high stresses and lack of plastic deformation

in front of the crack tip. We consider soft rubbery particles, rigid particulate fillers, and hybrid additives as impact modifiers and their mechanisms of impact modification. Specifically, we review micro-mechanics for polymeric materials engineered with a second, rubbery phase that provides soft particle toughening. These rubbery domains cavitate and provide opportunities for plastic deformation to occur. Herein, we review classical models that use the energy balance approach to provide the criterion for particle cavitation and explain the requirement of optimum particle size for effective cavitation. Further, we present an analytical solution for a porous media subjected to a hydrostatic state of stress by applying the von Mises yield criterion to elucidate how the presence of cavitated rubbery domains enables local yielding before material failure occurs. The solution shows that stress required for yield initiation decrease linearly with the concentration of pores, whereas stress required for yield percolation decreases logarithmically with the concentration of pores. Soft particle toughening relies on the optimization of size, interparticle spacing, and concentration of rubbery phase. Lastly, a dissertation outline is presented which explains in detail the scientific objectives, approach, and key findings of this work.

In the second chapter, we present impact modified stereolithography (SLA) resins engineered for the superior energy absorption of the SLA printed thermosets. SLA is a layer-by-layer fabrication technique that produces acrylate thermosets with high T_g and anisotropic mechanical properties. As a result, these thermosets demonstrate poor impact properties, especially when loaded perpendicular to the weak interface between layers. Impact modified SLA resins are prepared such that additives remain miscible in the uncured resin but undergo reaction induced phase separation (RIPS) to generate rubbery

domains after photopolymerization. Screening of different homopolymer and block copolymeric additives show that polydimethyl siloxane-polyethylene oxide/polypropylene oxide (DBP-732) brush block copolymer is the most effective impact modifier for the SLA resin. Herein, we report a thorough investigation of the effect of DBP-732 on the thermal, mechanical, and impact properties of the SLA printed thermosets. Impact modified SLA resins containing 15% of DBP-732 achieve a significant, an order of magnitude, improvement in the fracture energy release rate. This optimum concentration of 15% obtains rubbery domains of appropriate size (57 nm) and inter-particle spacing (33 nm) necessary to realize the most effective soft particle toughening. Notably, at this concentration, similar enhancements in the impact properties are achieved irrespective of the print layer orientation with respect to the loading direction and print layer thickness. Impact modification of the SLA resins produces a large-scale plastic deformation in an otherwise brittle material. Microscopic investigation of such process zone reveals that rubbery domains diffuse during the RIPS to preferentially localize at the layer interface and thereby, lead to isotropic toughness enhancements. Additionally, mechanical characterization demonstrates that a fraction of DBP-732 remains miscible in the cured thermoset and acts as a plasticizer, especially at higher concentrations.

In the third chapter, we discuss new strategies to obtain non-spherical rubbery domains for next-generation impact modification of semi-crystalline polypropylene and polyoxymethylene. These formulations are engineered in such a way that additives are miscible in the melt but demonstrate thermally induced phase separation (TIPS) to generate rubbery domains. Firstly, we explore the feasibility of blending two different block copolymeric impact modifiers with polypropylene to achieve non-spherical domains. We

present a systematic investigation of polypropylene (PP) formulations modified with SEBS (Styrene-ethylene/butylene-styrene), POE (Polyolefinic elastomer), and talc on the thermal and impact properties. These formulations show similar ellipsoidal or elongated domains when modified with only POE or only SEBS or even when modified with a combination of POE and SEBS. However, the length scale of phase-separated domains varies with the formulation. These ellipsoidal domains are further analyzed to quantify their size and shape factor. Impact properties of engineered polypropylene formulations show a strong dependence on particle size under quasi-static room temperature as well as high strain, low temperatures (extreme conditions). Notably, under extreme loading conditions, the major energy absorption occurs *via* craze nucleation and stabilization instead of particle cavitation. Polypropylene modified with SEBS generates larger (1 to 2 um) domains that are more effective in nucleating crazes and forming interconnected fibrillated crazes. Larger SEBS domains with their suitable size and shape demonstrate strong particle-particle interactions and provide the most effective toughening. A highly crystalline polyoxymethylene, in contrast with polypropylene, exhibits a brittle failure at room temperature. Herein, we investigate different homopolymer and block copolymeric additives for soft particle toughening. Polyoxymethylene shows significant improvements in the rupture energy density when modified with an optimum concentration (5%) of styrene-ethylene/butylene-styrene (SEBS) or styrene-isoprene-styrene (SIS) or maleic anhydrided functionalized SEBS (SEBS-g-MA). Alternatively, we prepare elastomeric adducts *via* reactive mixing to realize non-spherical rubbery domains. SEBS and SIS adducts obtain spherical rubbery domains. Interestingly, SEBS-g-MA adducts obtain highly irregular and unusual non-spherical domains with a shape factor of 25 (compared

with a shape factor of 1 for spherical domains). However, these non-spherical domains show large particle sizes (>10 um) which act as defects. Consequently, future studies will focus on tuning the particle size as well as shape.

In the fourth chapter, we describe multifunctional organophosphorus additives for high T_g epoxy networks which achieve both enhanced mechanical and flame-retardant properties. These molecular additives remain miscible in the cured epoxy networks and can participate in the mechanisms of fortification and flame inhibition. We characterized epoxy networks containing different organophosphorus additives to recognize that dimethyl methyl phosphonate (DMMP) reduces the rate of degradation with relatively minimal effect on the thermal stability, making it the most suitable additive. This work presents a systematic investigation of the effect of DMMP on the mechanical and heat release properties of both conventional and inherently low flammability epoxy resins. Mechanical characterization using non-standard compression testing shows 50% higher elastic modulus, and comparable yield stress, for networks containing DMMP relative to those without DMMP. Thermogravimetric analysis of DMMP-containing networks shows that DMMP promotes char formation and char residue reaches very high levels, up to 55%, for DMMP-containing deoxybenzoin networks. Microscale combustion calorimetry of all the DMMP-containing networks exhibits 50% lower heat release capacity and total heat release rate values relative to formulations without DMMP. Moreover, vertical burn testing demonstrates that epoxy networks containing DMMP burn slowly and self-extinguish without the need for halogenated flame-retardant additives. Morphological analysis of the charred DMMP-containing formulations shows a porous structure, suggesting a gas phase

flame retardance mechanism. Overall, the integration of DMMP into epoxy networks

produces materials with outstanding flame retardance and increased stiffness.

TABLE OF CONTENTS

CHAPTERS

LIST OF TABLES

LIST OF FIGURES

xxi

LIST OF ACRONYMS

TIPS: thermally induced phase separation

RIPS: reaction induced phase separation

SLA: Stereolithography 3D printing

PMMA: polymethyl methacrylate

PP: polypropylene

POE: polyolefinic elastomer

POM: polyoxymethylene

SEBS: styrene-ethylene/butylene-styrene

SEBS-*g*-MA: maleic anhydride functionalized styrene-ethylene/butylene-styrene

SIS: styrene-isoprene-styrene

DCP: dicumyl peroxide

PDMS: polydimethylsiloxane

DGEBA: diglycidyl ether of bisphenol A

BEDB: bishydroxydeoxybenzoin

DDS: diamino diphenyl sulfone

DMMP: dimethyl methyl phosphonate

TMP: trimethyl phosphate

TEP: triethyle phosphate

TPPO: triphenylphosphine oxide

D230: polyetheramine (Jeffamine)

HRC: heat release capacity

THR: total heat release

CHAPTER 1

REVIEW OF THE STATE-OF-THE-ART IMPACT MODIFICATION MECHANICS

1.1 Introduction

Additives are a powerful tool to tailor the physical and mechanical properties of polymeric materials. Synthesizing new materials with molecular architecture suitable for certain properties can be an expensive, multi-step process. In some cases, identifying the architecture needed for the desired property can be a challenging and time-consuming task. Polymer modification provides an economic and convenient route to obtain desired properties. Commercial "end-use" polymeric materials for automotive, healthcare, construction, and packaging industries are formulated using an additive package.[1, 2] In addition, additives enable material modification to make them compliant in accordance with the environmental or safety regulations. Allied market research has estimated that the global market for polymer additives was worth 57 billion dollars in 2020.[3] There are two major classes of additives that are used for polymer modifications. First, inorganic additives that include particulate fillers and fibers. Second, organic additives, such as homopolymers, block copolymer, and small molecules. Organic additives are further classified based on their molecular weight or interactions with the matrix or their miscibility in the host polymer matrix. Additives are used for a variety of reasons. They are used as heat and UV stabilizers, plasticizers, impact modifiers, flame-retardants, processing aids, surfactants, antioxidants, colorants, and antimicrobials.[2, 4]

The main goal of this dissertation is to engineer polymer formulations using additives that result in advanced material properties for semi-crystallin and amorphous

polymers. Chapter 2 and Chapter 3 investigate additives that phase separate to generate a second rubbery phase and provide effective toughening for 3D printed glasses and semi-crystalline thermoplastics, respectively. Chapter 4 focuses on the potential of using fortifiers, molecular additives that stay miscible, with high T_g epoxies to achieve enhanced mechanical and physical properties.

In this chapter, we review the micro-mechanics associated with impact modification in polymeric materials. We present the requirements for soft particle toughening within the context of the asymptotic stress field in front of a crack tip, the process of release of hydrostatic stress, and resulting dissipative processes that consume energy and delocalize the fracture event.

1.2   The need for polymer impact modification

One of the major applications of additives is impact modifiers. Polymers that exhibit poor fracture toughness under operating conditions are modified using additives to improve their fracture toughness properties. This chapter reviews micro-mechanics for effective impact modification. To develop impact modifiers, it is necessary to first understand what causes materials to fail in presence of a crack or a defect. The presence of a crack is detrimental to material performance for two main reasons.

First, the asymptotic state of stress in front of the crack tip is highly triaxial. When a material is arbitrarily loaded, the resulting stresses cause the material to undergo deformation that can be deconvoluted into a combination of volume and/or shape change. In isotropic materials, hydrostatic stresses subject the material to volume change, whereas shear stresses alter the shape of the material. The change in shape or distortion, and its

associated energy density (distortional energy density) are the basis of the von Mises yield criterion that is widely used in a modified form for polymers.[5]

Figure 1.1 shows the effect of the state of stress on mean hydrostatic stress (σ_m) and octahedral shear stress (τ_{oct}) associated with pure distortion for three different stress states. Figure 1.1-(a) shows the ratio between σ_m and τ_{oct} that occurs in a uniaxial tensile test. Under these conditions, τ_{oct} is approximately twice that of σ_m which indicates that the material is subjected to a shear stress of twice the magnitude as that of hydrostatic stress. Figure 1.1-(b) shows that the ratio between σ_m and τ_{oct} for equi-biaxial tension is dramatically different, the hydrostatic component is 40% greater than the shear component. Finally, Figure 1.1-(c) shows the ratio between hydrostatic and shear components for a region directly in front of a crack tip under a plane strain condition where hydrostatic component is 20 times greater than the shear component. Under these conditions, the material cannot readily yield (which is a shear phenomenon), and often fragments or fractures in a brittle fashion to accommodate the volume change requirements.

$$\frac{\sigma_m}{\tau_{oct}} = 0.51 \qquad \frac{\sigma_m}{\tau_{oct}} = \sqrt{2} = 1.4 \qquad \frac{\sigma_m}{\tau_{oct}} = \sqrt{2}\,\frac{1+v}{1-2v} = 20.5$$
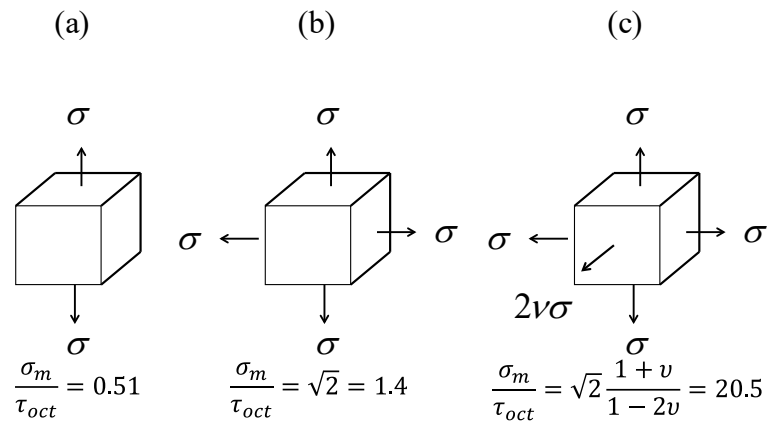
Figure 1.1: Effect of state of stress on mean hydrostatic stress (σ_m) and octahedral shear stress (τ_{oct}) for the case of a) uniaxial tension, b) equi-biaxial tension, and c) triaxial (in front of a crack tip).

During a fracture event, there arises a competition between the creation of a new surface area *via* crack propagation and energy dissipation *via* matrix yielding. However, the triaxial state of stress in front of the crack tip eliminates plastic deformation. As a result, when the energy stored in the material exceeds the energy required for the creation of a new surface area (resulting from bond breaking) material exhibits crack propagation. This, in turn, leads to catastrophic brittle failure.

A second reason is that there exists a stress singularity at the crack tip. Irwin developed a stress field solution that describes local stresses in front of the crack tip as a function of far-field applied stresses, as shown in Equation 1.1.[6] This solution was modified from Westergaard's solution published earlier in 1939.[7] It shows that stresses scale inversely with the distance from the crack tip and thereby, theoretically achieves infinite stress at the crack tip. Such high stresses result in material failure.

Equation 1.1: $\sigma_{ij} = \dfrac{K_I}{\sqrt{2\pi r}} f_{ij}(\theta)$
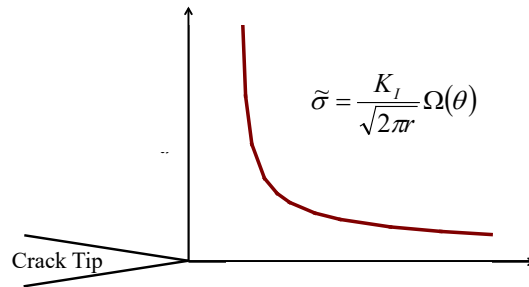
Figure 1.2: Stress field in front of the crack tip.

Additionally, extremely high stresses in front of a crack tip exceed the yield stress and thereby, results in localized small-scale yielding. Irwin, Dugdale, and Barenblatt independently estimated the size of a zone where localized yielding occurs.[6, 8, 9] These studies demonstrate that the size of the process zone inversely scales with the yield stress of the material, as shown in Equation 1.2. Materials with higher yield stresses exhibit a

smaller localized yielding in comparison with materials with lower yield stresses. Matrix yielding occurs only in a very small region localized at the crack tip for materials with high yield stresses. This minimizes energy dissipation during fracture. As a result, materials preferentially dissipate energy by creating a new surface area and thereby, fail in a brittle manner. On the other hand, a material with lower yield stress can achieve a larger plastic zone. This leads to higher energy absorption during fracture. Such materials demonstrate a more ductile fracture event.

Equation 1.2: $r_p \propto \left(\dfrac{K_I}{\sigma_y}\right)^2$

Yield stress for amorphous polymers scales with their glass transition temperature (T_g) and for semi-crystalline polymers, it scales with overall crystallinity and lamellar thickness.[10, 11] Therefore, high Tg glasses and highly crystalline semi-crystalline polymer exhibit brittle failure (Figure 1.3). Consequently, it is often necessary to improve the impact properties of polymers.
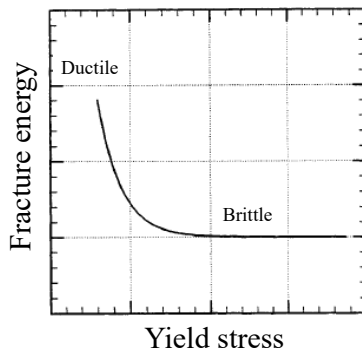
Figure 1.3: Impact properties of polymers as a function of their yield stress.[12]

Polymer impact modification is achieved by introducing a second phase in the polymer matrix. This second phase can be rigid inorganic fillers or soft rubbery domains or a hybrid combination of both.[13-17] This dissertation focuses on soft particle toughening of semi-crystalline thermoplastics and amorphous thermosets.

1.3   Soft particle toughening

Conventional soft particle toughening involves the incorporation of soft rubbery additives as a second phase. These rubbery domains are subjected to volume change under the triaxial state of stress in front of the crack tip. These domains of appropriate size cavitate at a certain threshold volumetric strain. Cavitation relieves the hydrostatic state of stress and results in a biaxial state of stress at which plastic deformation can occur. Plastic deformation involves matrix yielding, shear band formation, or biaxial stretching of cavitated rubbery domains. Further, cavitated particles act as stress concentrators when the material is loaded and when a material is engineered with appropriate interparticle spacing between the domains, matrix ligament between the domain's yields. These processes significantly enhance the energy dissipation during an event of a failure. Cavitation of rubbery domains results in particle-particle interaction through inelastic void growth, shear banding, or craze formation between particles and delocalize the fracture event, increasing the volume of material dissipating energy prior to and during the fracture event.

1.3.1   Cavitation of rubbery domains

Rubber cavitation acts as a precursor for plastic deformation processes. Many studies focus on understanding the factors that affect rubber cavitation. Dompas and Groenincks evaluated the criterion necessary for rubber cavitation.[18] They considered perfectly spherical rubbery particles with low shear modulus and assumed that cavitation of rubbery particles is an instantaneous process. Their model predicts that cavitation occurs when the strain energy stored in these particles exceeds the energy required for the creation of a new surface area. Strain energy depends on the particle volume, whereas the energy

barrier for creating a new surface scales with the surface area. This results in a scaling relationship between the stress required for the cavitation and the particle size, as shown in Equation 1.3.

Equation 1.3: : $\sigma_m = K_m \left(\dfrac{6\gamma}{R_c K_R} \right)^{3/4}$

where σ_m is the mean far-field (applied) stress; K_m and K_R are bulk modulus for the matrix and the rubber, respectively; R_c is the radius of the rubbery domain; γ is the surface energy of the rubber particle.
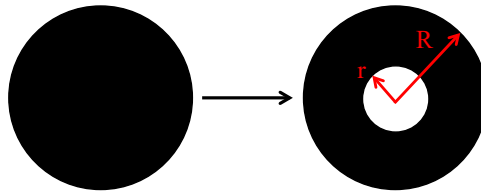
Figure 1.4: Cavitation of soft, rubbery domains in front of the crack tip.

Alternatively, Bucknall and Lazzeri derived conditions that result in cavitation of rubbery domains.[19] Their model uses a similar energy balance approach. However, it also accounts for the shear deformation of cavitated rubbery domains and thereby, it is not restricted for rubbers with low shear modulus. Nonetheless, both models demonstrate a similar relationship between the stress required (or volumetric strain) for cavitation and the particle size. These models suggest that there exists a critical particle size for cavitation. Smaller particles are not able to cavitate and larger particles act as defects. Therefore, it is necessary to achieve rubbery domains of optimum particle size that can cavitate under the given loading conditions.

1.3.2   Effect of rubber concentration

Cavitation of rubbery domains relieves the hydrostatic state of stress and allows the matrix yield to occur. Kinloch *et al.* studied the effect of particle cavitation on stress fields using finite element modeling.[20] They compared von Mises stresses before and after the cavitation of rubbery domains when a material is loaded under a uniaxial or triaxial state of stress. von Mises stresses remain comparable even after the cavitation of rubbery domains when a material is under uniaxial tension. On the other hand, von Mises stresses increase significantly after the cavitation of domains when a material is under triaxial loading. These results demonstrate that cavitation is necessary for shear yielding to occur in front of the crack tip where the state of stress is highly triaxial. Cavitation promotes the growth of shear bands and results in matrix yielding.

The modulus mismatch between the rubbery domains and the matrix results in stress concentration at the rubber-matrix interface. During the failure event, after the cavitation of rubbery domains, yielding is initiated at the interface, followed by a radially outward propagation. These propagating yield fronts percolate when a material is engineered with appropriate inter-particle spacing. This results in pseudo-macroscopic yielding in front of the crack tip and thereby, improves impact properties.

Herein, we derive a yield criterion for a model porous material containing pores of an identical size which are equally distributed and subjected to pure hydrostatic tension. This criterion demonstrates conditions when yielding initiates at the surface of the pores (i.e., after rubber cavitation) and when gross yielding or percolation occurs. The analytical solution is derived for a model porous media containing pores of uniform size "a" and uniform inter-particle spacing of "2b". The system is assumed to be under a hydrostatic

state of stress. We apply the von Mises yield criterion to evaluate the applied far-field stress required for the initiation and yield percolation (complete derivation is included in the Appendix).

Analytical solution results show that the stress required for yield initiation decreases linearly with the concentration of pores (Equation 1.4). Even in the presence of an isolated pore matrix yields at 2/3rd of the yield stress of the matrix (σ_y). Further, the solution also shows that the far-field stress required for yield percolation to occur decreases logarithmically as a function of pore concentration (Equation 1.5). Yield percolation is defined to occur when the yield fronts from each pore reach a radial distance of "b". These results show that complete matrix yielding can be achieved at stresses much lower than the yield stress of the matrix at a higher pore concentration, as shown in Figure 1.5.

Equation 1.4: $\sigma_\infty = \dfrac{2}{3}\sigma_y[1 - c]$

Equation 1.5: $\sigma_\infty = 2\sigma_y \ln c^{\frac{-1}{3}}$
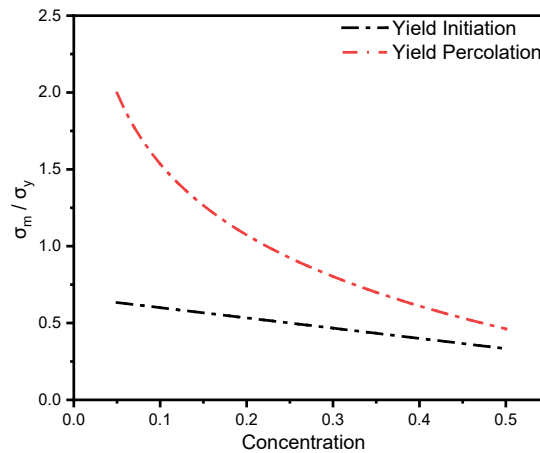
Figure 1.5: Effect of pore concentration on far-field stress required for yield initiation and yield percolation.

1.3.3   Mechanisms of enhanced energy absorption

Impact modified polymers demonstrate superior impact properties when engineered with rubbery domains of optimum size, optimum inter-particle spacing, and optimum concentration. Rubbery domains enable plastic deformation during the failure by promoting shear yielding and, in some cases, crazing.[5, 21]

In front of the crack tip, there exists a plane strain condition where plastic deformation is difficult to occur. Cavitation of rubbery domains relieves these constraints and obtains a plane stress condition where shear deformation occurs more readily.[22] For example, ethylene propylene diene monomer (EPDM) rubbery domains present in semi-crystalline polypropylene cavitates and allows the matrix to undergo shear yielding, thereby improving the impact properties.[23] Tang *et al.* attributed high impact properties of rubber modified polypropylene to extensive shear yielding that occurs between cavitated domains.[24] Even for glassy epoxies, energy absorbing shear yielding often precedes the cavitation of rubbery domains.[25] In the case of semi-crystalline polyamides, cavitation of tetrablock copolymer domains induces shear deformation and results in improved toughness.[26] Specifically, ductile failure for polyamide occurs only when engineered with an optimum concentration of elastomeric domains. Further, Wu describes that impact properties depend on critical interparticle spacing, an inherent matrix property, in addition to the particle size and concentration.[27] When the interparticle spacing is smaller than the critical value, stress fields around the cavitated domains overlap and thereby, results in the formation of shear bands.[28] During a failure event, rubbery domains of appropriate particle sizes present in the polymer matrix cavitate and act as a precursor for shear yielding. These

domains must have an optimum interparticle spacing to involve a large matrix volume in plastic deformation and thereby, achieve superior energy absorption.

Crazing is another failure mechanism commonly observed for rubber-modified polymers.[29-31] Crazing also incorporates volume change, unlike shear yielding. Rubbery domains serve two primary functions for materials that exhibit craze formation. These domains provide sites for craze nucleation to occur, and also, terminate the propagating crazes to prevent detrimental craze to crack transitions. Rubbery domains are a heterogeneous phase that creates high stress concentration at its interface. Crazes are nucleated at this interface *via* a void formation and propagate in a direction perpendicular to the principal loading direction. These load-bearing crazes grow as the material is drawn to form fibrillated crazes. Further, higher stress concentration in the vicinity of rubbery domains is necessary for stable craze growth. The spatial region where stresses are high scales with the particle size and as a result, large rubbery domains are more effective for craze nucleation.[32, 33] Consequently, craze length for crazes nucleated at the rubbery domains also scales with domain sizes.[33] McCutcheon *et al.* observed a similar effect of particle size on crazing for impact modified PLA.[34] They demonstrated that craze initiation stresses are lower for larger block copolymeric domains. As a result, the architecture of block copolymer that results in particles with appropriate sizes is necessary to achieve effective toughening *via* crazing. In some cases, cavitation of rubbery domains results in the formation of multiple arrays of crazes in conjunction with shear banding.[31] Additionally, crazes are terminated at the surface of rubbery domains as well. Terminating crazes before craze to crack transition occurs is necessary to prevent a catastrophic failure.

1.4   Rigid particle toughening

In addition to soft particles, rigid particulate fillers are often used as impact modifiers for polymeric materials. Rigid particles improve the fracture toughness of polymers *via* two primary mechanisms.[35] First, these particles are assumed to contribute towards crack pinning and bifurcation.[36] Rigid particle present in the crack propagation path resists further crack propagation. As a result, the crack front gets pinned at the particle, changes its direction, and propagates in between two particles, termed as "bowing".[37] This increases the energy consumed in the crack propagation and improves fracture toughness. This phenomenon is primarily observed in glassy polymers, but it is not uncommon in semi-crystalline polymers.[38, 39] Second, rigid particles de-bond from the matrix during the failure event and result in a similar effect as that of cavitation of rubbery domains.[40] De-bonding creates voids in the matrix, relieves hydrostatic stress, and promotes shear yielding. These plastic deformation processes absorb energy. De-bonding of these fillers depends on the interfacial adhesion with the matrix. If the interfacial adhesion is weak, energy absorption occurs during the de-bonding of these particles. Similarly, recent studies show that the impact properties of polypropylene modified with inorganic fillers depend on the ability of fillers to de-bond and generate voids of appropriate size and spacing.[41] Epoxy composites modified with glass beads demonstrated the formation of diffuse shear bands and microscopic yielding.[42] On the other hand, if the interfacial adhesion is strong, these particles provide stress concentration sites where craze nucleation occurs. Heterogeneous rigid particles have a higher elastic modulus than polymers. During a failure event, these particles are not deformed when the matrix in the vicinity accumulates elastic strain. This results in a stress concentration at the interface. The magnitude of stress

concentration depends on a variety of factors. These factors include particle size, shape (spherical or elongated or fibrous), and interfacial adhesion with the matrix. Jung *et al.* observed that crazing is the energy absorption mechanism for rubber modified semi-crystalline polypropylene.[43] Incorporating talc resulted in the formation of these crazes, followed by shear yielding that leads to improved impact properties. In another example, Polypropylene modified with inorganic calcium carbonate leads to craze formation *via* repeated debonding of filler particles.[44] Even in the case of rigid particulate fillers, impact properties depend on particle size, interparticle spacing, and concentration.[45]

Rigid particulate fillers enhance the energy absorption processes, in addition to improving the stiffness of the matrix. However, rigid inorganic additives tend to agglomerate and act as defects. On contrary, soft rubbery domains can improve the impact properties at the expense of matrix rigidity. Additionally, cavitated rubbery domains can deform and thereby, stabilize the void growth and absorbs energy, unlike rigid additives. Therefore, polymeric materials are often modified with a combination of soft rubbery domains and inorganic fillers to achieve balanced toughness and stiffness properties.[46] The ternary blend of polymer, soft, and rigid particles provides opportunities to create a filler network with overlapping stress fields.[15] This reduces the interparticle distance and results in synergistic improvements in the fracture toughness properties. Interestingly, in some cases, inorganic fillers reduce the rubbery domain sizes and it is advantageous when rubber domains are larger than the optimum in the absence of an inorganic filler.[43]

Overall, in a hybrid composite material, cavitation of rubbery domains and de-bonding of inorganic fillers relieves the triaxial state of stress and allows matrix yielding to occur. The interconnected network between these additives maximizes the volume of

the matrix involved in the plastic deformation. Additionally, inorganic fillers also result in crack deflection or craze nucleation, whereas rubbery domains can nucleate crazes or undergo shear deformation. For both types of additives, impact properties strongly depend on particle size, interparticle spacing, concentration, and interface with the matrix. Nevertheless, hybrid composites provide opportunities to achieve synergistic toughness improvements.

1.5   Dissertation outline

This dissertation investigates additives for polymeric materials to achieve advanced material properties, such as impact and flame-retardant properties. Specifically, we deal with semi-crystalline thermoplastics polypropylene and polyoxymethylene, and glassy thermosets acrylates and epoxies. Herein, polymer formulations are engineered using strategically selected additives that obtain desired material properties *via* an economic and convenient approach.

In chapter 2, we investigate soft particle toughening for glassy acrylate thermosets fabricated using stereolithographic (SLA) 3D printing. The main objective of this work is to improve the fracture toughness of inherently brittle SLA printed materials. Our approach is to develop resin formulations that generate rubbery domains of optimum size and interparticle spacing in SLA printed materials for effective soft particle toughening. These SLA resins are prepared using additives that are miscible in the SLA resin but exhibits reaction induced phase separation (RIPS) to generate phase-separated rubbery domains upon photopolymerization. We investigate the effects of particle size, interparticle spacing, and concentration on the impact properties. Additionally, SLA printed thermosets exhibit

strength anisotropy and consequently, show poor impact properties when loaded perpendicular to the printed interfaces. Hence, we also evaluate the effect of print anisotropy and print layer thickness on fracture toughness. Further, fractographic analysis is conducted to understand the energy absorption mechanisms for impact modified SLA resins. Lastly, the mechanical and thermal properties of SLA printed thermosets are characterized.

Chapter 3 presents strategies to obtain non-spherical phase-separated rubbery domains for next-generation impact modification of semi-crystalline polypropylene (PP) and polyoxymethylene (POM). Impact modification of polypropylene and polyoxymethylene offers different sets of challenges. Polypropylene is ductile at room temperature, however, exhibits brittle failure at subzero temperatures. On the other hand, polyoxymethylene demonstrates high crystallinity and consequently, fails in a brittle manner even at room temperature. As a result, these thermoplastic materials are engineered for soft particle toughening using additives that remain miscible during the melt processing but generate rubbery particles upon cooling *via* thermally induced phase separation (TIPS). For polypropylene, we implement the strategy of blending two block copolymeric additives to obtain non-spherical domains. Impact properties of polypropylene are evaluated using quasi-static room temperature fracture toughness tests and high strain rate, low temperature (extreme conditions) instrumented impact testing. Further, we investigate the failure mechanisms that occur under extreme loading conditions. In another approach, we develop elastomeric adducts *via* reactive mixing to realize non-spherical domains for polyoxymethylene. Impact properties of polyoxymethylene are characterized using tensile testing. In both cases, we evaluate the shape factor associated with these irregular and non-

spherical domains. This chapter describes the effect of particle shape, size, and concentration on the impact properties of polypropylene and polyoxymethylene. We discuss the morphological features of the rubbery phase necessary to achieve superior energy absorption.

Chapter 4 describes multifunctional molecular additives for high T_g epoxy composites which improve mechanical and flame-retardant properties. This work aims at overcoming the drawbacks of conventional halogenated flame-retardant additives which produce toxic gases during the decomposition and reduce the mechanical properties. We utilize environmentally friendly, organophosphorus fortifiers as additives and low-flammability deoxybenzoin-based epoxy resins to combine materials chemistry with mechanical enhancement mechanisms. Further, we investigate the possible synergisms between organophosphorus moieties and deoxybenzoin-based epoxy resins for enhanced flame retardance. Herein, we illustrate the effect of organophosphorus dimethyl methylphosphonate (DMMP) concentration on the mechanical, thermal, and flame-retardant properties of conventional bisphenol A-based and deoxybenzoin-based epoxy resins. Additionally, we also hypothesize the flame inhibition mechanism and the interactions between DMMP and the epoxy networks using solid state nuclear magnetic resonance (ssNMR) and scanning electron microscopy (SEM).

CHAPTER 2

IMPACT MODIFICATION OF SLA PRINTED ACRYLATE THERMOSETS USING REACTION INDUCED PHASE SEPARATION OF ADDITIVES

2.1   Introduction

Additive manufacturing, also known as 3D printing, is a rapidly expanding industry sector that is expected to capture a 21-billion-dollar market by 2021. Stereolithography (SLA) is one major 3D manufacturing technique that intrinsically fabricates parts through a layer-by-layer process transforming a liquid resin into a solid portion of the object using photopolymerization.[47-49] The stereolithographic process was first patented by Charles Hull in 1984 and it has developed tremendously over the last few decades. SLA printing has numerous advantages that include, high resolution, smooth surface finish, ability to construct complex geometries, and relatively rapid fabrication within the context of 3D printing. Consequently, SLA printing is widely implemented in prototyping and production of customized parts (for example, dental and biomedical applications).[49, 50]

SLA resins are primarily comprised of acrylate-functionalized epoxy, polyurethane or polyether monomers, oligomers, diluents, and a photo-initiator. The resins are primarily formulated to meet the viscosity requirements for the process as well as enable crosslinking *via* laser-induced polymerization. The SLA manufacturing process is compatible with a variety of resins and provides some opportunities for resin modification suitable for specific applications.[47, 51] However, SLA, like all other 3D printing processes, generates interfaces at each layer of printing. This interface has intrinsically lower crosslink density or other characteristics that result in a reduction in the strength of the printed part if loaded

17

perpendicular to the printed interfaces. This reduction in strength when loaded in this specific direction is referred to as strength anisotropy and results in poor impact properties in comparison with injection molded parts.[52-54]

During fracture of any material, there is an inherent competition that arises between the creation of a new surface area *via* crack propagation and plastic deformation *via* matrix yielding in front of the crack tip. Consequently, materials that have a relatively low yield stress when compared to their fracture energy tend to dissipate more energy with yielding at the crack tip before catastrophic failure occurs.

In general, stereolithographic 3D printing presents two unique challenges. First, they are glassy thermosets with a glass-transition temperature (T_g) in the range of 60 to 100 °C. Since the yield stress scales with the T_g, yielding and associated energy dissipation are limited.[12, 52, 55] Additionally, the intrinsic reduction of crosslink density between print layers lowers the fracture energy at that interface. Consequently, localized fracture along one or two interfaces occurs before a yield/process zone can develop and results in low fracture energy when loaded perpendicular to the print layer direction. This, in turn, produces the widely observed strength anisotropy commonly reported from this manufacturing process.

Initial attempts to address this issue in SLA formulations have incorporated functionalized nanoparticles in the form of graphene nanosheets, calcium sulfate whiskers, and carbon nanotubes.[56] However, these attempts have largely proven unsuccessful for a variety of reasons. First, good nanoparticle dispersion is difficult and intrinsically increases the resin viscosity, affecting print fidelity. Additionally, nanoparticle agglomeration is common and produces scattering of the UV laser light limiting the ability to fully cure the

resins creating a challenging problem to achieve impact modification with rigid inorganic fillers.[56-58]

Despite the extensive research on SLA printed nanocomposites, there are limited reports on soft particle toughening of SLA printing resin formulations.[59, 60] Soft particle impact modification is achieved by engineering a formulation in such a way that soft rubbery particles are formed at an optimum size and interparticle distance during the manufacturing process. Prior to fracture of the material, these particles cavitate to relieve the hydrostatic stress, promote yielding, and delocalize the fracture event through particle-particle interaction to increase the volume of material dissipating energy during the fracture event.[61-64] This improves the energy absorption that occurs during a failure. The mechanics of this process is discussed in detail in Chapter 1 of this dissertation.

For SLA formulations, it is necessary to identify additives that are initially miscible in the resin prior to cure, thereby allowing for full cure using the UV laser. Upon curing, rapid reaction induced phase separation (RIPS) must happen to generate rubbery domains of the appropriate size and spacing to provide the optimum template for effective toughening. Block copolymers are commonly used additives for impact modification owing to their flexibility of synthesizing one block with a rubbery backbone and the other with a backbone compatible with the resin. Bates *et al.* showed that block-copolymers self-assemble during the phase-separation in spherical, cylindrical, or worm-like structures and enhance the fracture toughness of thermosetting epoxy.[25] Further, Bucknall and Heckman observed that even a small concentration of silicone oil improves the cavitation mechanism and greatly enhances the impact properties of polystyrene modified with rubber.[65, 66] In addition, many research groups demonstrated the application of

polydimethylsiloxane-based liquid rubber, core-shell rubber particles, and block copolymers as impact modifiers.[67]

In this chapter, homopolymer and block copolymeric additives are investigated for their performance as impact modifiers in a commercial SLA resin formulation. The goal of this study is to achieve significant improvements in the fracture toughness properties of SLA printed acrylate thermosets *via* resin formulations developed for soft particle toughening and eliminate or otherwise reduce the strength anisotropy in SLA print materials. Specifically, we investigate the effect of polydimethylsiloxane, polypropylene/polyethylene oxide-based block copolymers on the impact properties of SLA printed thermosets. The thermal and mechanical properties are characterized by differential scanning calorimetry (DSC), dynamic mechanical analysis (DMA), compression tests, and conventional fracture toughness tests. The morphological investigation and fractographic studies incorporate both optical microscopy and scanning electron microscopy (SEM). A systematic study is presented to illustrate the effect of concentration of the impact modifier on the fracture toughness, non-linear mechanical properties, morphology, and glass transition temperature of the matrix. In addition, the influence of SLA print parameters including print layer orientation (e.g., strength anisotropy) and print layer thickness is investigated.

2.2   Experimental

2.2.1   Materials

SLA resin Clear V4 was purchased from Formlab. Polydimethylsiloxane (PDMS)-based homopolymers including carbinol terminated PDMS, acryloxy terminated PDMS,

and block copolymers including polydimethylsiloxane-polyethylene oxide (PDMS-PEO), polydimethylsiloxane-polyethylene oxide-polypropylene oxide (PDMS-PEO-PPO), and polydimethylsiloxane-polyethylene oxide-polypropylene oxide-polyvinylmethylsiloxane (PDMS-PEO-PPO-PVMS) were obtained from Gelest chemicals. Block copolymers polymethylmethacrylate-polybutylacrylate-polymethylmethacrylate (PMMA-PBuA-PMMA) was purchased from Arkema. Pluronic block copolymers (PEO-PPO-PEO), polyethylene-polyethylene oxide (PE-PEO), and other block copolymers were procured from Sigma Aldrich. Table 2.1 shows the chemical structures and Table A2.1 (Appendix) provides commercial grades and compositions of homopolymers and block copolymers. All the chemicals were used without further purification unless mentioned otherwise.

2.2.2   Sample preparation

The general procedure for making SLA printing resins involved mixing an appropriate amount of additive, either a homopolymer or a block copolymer, with SLA resin at temperatures of up to 65 °C. Necessary caution was exercised during mixing to avoid any direct sunlight by using amber color vials and covering them with aluminum foil. Specifically, SLA resins containing 0 to 20 % concentrations of DBP-732 block copolymers were prepared. These SLA resins were prepared by mixing Clear V4 with DBP-732 at 65 °C for 30 mins. These formulated SLA resins were used for SLA printing.

SLA printing was performed using Formlab's desktop 3D printer - Form 2. It operates at room temperature and uses a 250 mW laser with a wavelength of 405 nm and a spot size of 140 um. Mechanical testing specimens, such as compact tension for fracture toughness testing and cylindrical billets for compression testing, were fabricated using the

Form 2 printer in open mode. This enables printing using customized resin formulations. Additionally, Matt Lampe, a lesser group student, modified the printer bath with a PDMS mold which eliminates the need to fill the entire resin bath with SLA resin. As a result, SLA printing with smaller resin volumes of 30 ml was made possible.
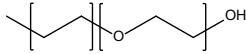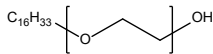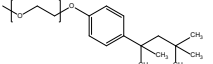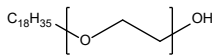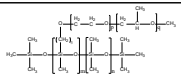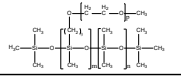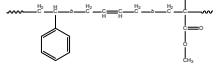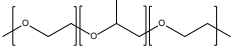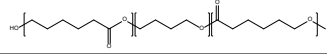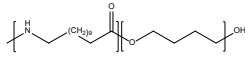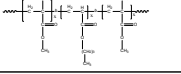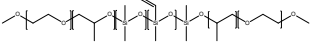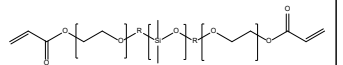
	Block copolymer	Chemical structure
1	PE-PEO	
2	PEO-hexadecyl ether	
3	PEO-nonylphenyl ether	
4	PEO-oleyl ether	
5	PDMS-[65-70%(60%PPO-40%PEO)]	
6	PDMS-PEO	
7	PS-PB-PMMA	
8	PEO-PPO-PEO	
9	PCL-PTHF-PCL	
10	Polylauryllactam-PTHF	
11	PMMA-PBuA-PMMA	
12	PEO-PPO-PDMS-PVMS	
13	Carbinol(-OH) terminated PDMS	
14	Acryloxyl terminated PDMS	

Table 2.1 Chemical structures for homopolymers and block-copolymers used as additives in stereolithographic resin formulations.

Form 2 facilitates SLA printing with a layer thickness of 25 um, 50 um, and 100um. Samples for mechanical and thermal characterization were printed using 100 um as a layer

thickness unless mentioned otherwise. All printed samples were rinsed with isopropanol to remove any unreacted resin, followed by post-curing at 65 °C for 12 hours. These samples were stored in a dry nitrogen environment before and after testing.

2.2.3   Fracture toughness testing

Fracture toughness measurements were conducted according to ASTM standard D5045-99 using compact tension specimens with dimensions of 25 x 24 x 3.2 mm.[68] After printing, holes were drilled using a milling machine. These specimens were further notched using a diamond wafering blade, followed by pre-cracking. These notched samples were dipped in liquid nitrogen for few minutes, followed by sliding a razor blade in the notch and gently tapping it with a wrench to create a sharp pre-crack.

These mini compact tension specimens satisfy the condition of plain strain as $B \geq 2.5 (K_q/\sigma_y)^2$, where B is the thickness, K_q is the linear elastic fracture toughness, and σ_y is the yield stress. Load-displacement curves were recorded using Instron 5800 installed with a 1 kN load cell at a crosshead speed of 0.5 mm/min. Fracture toughness was determined using Equation 2.1.

Equation 2.1: $K_q = \frac{P_c f(x)}{BW^{1/2}}$

where P_c is the critical load, B is the specimen thickness, W is specimen width. Herein, we are reporting K_q instead of K_{IC} owing to the use of a mini-CT specimen.[69, 70] The geometric factor f(x) is a dimensionless power function in terms of x, which is equal to the ratio of the pre-crack length to specimen width (a/W), given by Equation 2.2.

Equation 2.2: $f(x) = \frac{(2+x)(0.886 + 4.64x - 13.32x^2 + 14.72x^3 - 5.6x^4)}{(1-x)^{3/2}}$

Linear fracture energy release rate (G_q) was determined for resin formulations with the linear load-displacement response using Equation 2.3 and non-linear fracture energy release rate (J_q) was evaluated for resin formulations with non-linear load-displacement curve using Equation 2.4.

Equation 2.3: $G_q = \frac{K_q^2}{E}$

Equation 2.4: $J_q = \frac{K_q^2}{E} + \frac{nA}{B(a-w)}$

where n denotes geometry factor with a value of 2.15 for compact tension specimens and A represents the area under load versus displacement curve up to the maximum load. All values reported here are an average of at least 3 specimens.

2.2.4 Thermal analysis

Differential scanning calorimetry (DSC) was performed using TA instruments Q200 to measure the glass transition temperature (T_g). Samples were evaluated in the temperature range of -50 °C to 200 °C with a consecutive heat-cool-heat cycle at a heating rate of 10 °C min^{-1}. T_g was defined as the inflection point of the transition observed during the 2nd heat cycle.

TA Instruments Q800 was used for Dynamic mechanical analysis (DMA) in the temperature range of -140 °C to 150 °C with a heating rate of 3 °C min^{-1} and a frequency of 1 Hz under constant strain mode. T_g was defined as the temperature corresponding to the maximum of the tan delta. Rubbery plateau modulus was defined as the storage modulus at T_g + 40 °C.

2.2.5 Compression testing

Mechanical properties of 3D printed acrylate thermosets including elastic modulus, yield stress, and strain hardening modulus were determined using non-standard compression testing. The testing was performed using SLA printed cylindrical specimens with a diameter-to-height ratio of 1:1 and a diameter of 10 mm to prevent buckling of the samples. These cylindrical specimens were tested using an Instron 5800 at a constant crosshead rate of 2 mm min^{-1}. The top and bottom surfaces of the specimens were lubricated with silicone oil and Teflon tape. The recorded data was corrected for the compliance of the system and reported values of mechanical properties are average of at least three identically evaluated specimens.

2.2.6 Scanning electron microscopy

The morphology of SLA printed samples was determined using a Magellan 400 scanning electron microscope equipped with a field emission gun having a maximum operative voltage of 30 kV. Samples for SEM were prepared by cryofracturing, where a sample was dipped in liquid nitrogen and then fractured. These cryofractured surfaces were sputter-coated with a thin layer of gold before SEM imaging.

2.2.7 Optical microscopy

SLA printed acrylate thermosets were microtomed and characterized using an Olympus BX51 optical microscope under transmitted light. Microtoming was performed, on the region in front of the crack tip (process zone) of compact tension specimens, using an RJ Ultramicrotome with a diamond knife at room temperature.

2.3 Results and Discussion

2.3.1 Fracture toughness comparison for various polymeric additives

Impact modified SLA resins were prepared by blending the commercially available Clear V4 resin with approximately 50 different additives in order to screen them as potential candidates. We used two criteria to screen these additives. First, Clear V4 resin modified with the additive should be homogeneous and have suitable resin viscosity. This is necessary to ensure that SLA printed parts have desired resolution and fidelity. Second, the additive should be miscible in the uncured SLA resin and should generate phase-separated domains in the cured SLA printed thermoset. An additive that stays completely miscible, even in the cured thermoset, results in a transparent sample and can act as a plasticizer. On the other hand, phase-separated domains scatter light, and therefore, an additive that forms phase-separated domains in the cured thermoset results in a translucent or opaque sample. We screened different homopolymers and block copolymers with different chemical structures, relative fractions of each block, and molecular weight. These additives were incorporated at a concentration of 10% in the Clear V4 resin. Impact properties for SLA resins modified with screened additives were evaluated using fracture toughness test.

Table 2.2 shows the screening results for impact modified SLA resins. Miscibility of homopolymer and block copolymer additives in the uncured Clear V4 resin depends on their molecular weight, architecture, and functionality. For example, Pluronic block copolymers with lower molecular weights are miscible in the Clear V4 resin, however, they are immiscible at higher molecular weights (>10,000 g/mol). Similarly, polydimethylsiloxane-polyethylene oxide block copolymers are miscible only up to the

molecular weight of 1000 g/mol. Alternatively, PDMS-PEO and PMMA-PBuA-PMMA block copolymers are miscible in the uncured Clear V4 resin. On contrary, analogous unsaturated block copolymers, such as SBM or PDMS-PVMS, are immiscible in the uncured Clear V4 resin.

Block copolymer (Commercial Name)	Solubility in Clear V4 resin	Appearance after 3D printing
PE-PEO	No	
PE-PEO (Brij 93)	Yes	Transparent
PE-PEO (Brij L4)	Yes	Transparent
PE-PEO (Brij S10)	Yes	Transparent
PE-PEO (Brij S20)	Yes	Transparent
PEO-hexadecyl ether(Brij C10)	Yes	Transparent
PEO-nonylphenyl ether(IGEPAL CO-720)	Yes	Transparent
PEO-oleyl ether(Brij O20)	Yes	Transparent
PDMS-[65-70%(60%PPO-40%PEO)] (DBP 732)	Yes	Translucent
PDMS-PEO (DBE-814)	Yes	Transparent
PDMS-PEO (DBE-712)	Yes	Transparent
PDMS-PEO (DBE-411)	Yes	Transparent
PDMS-PEO (DBE-921)	No	
PDMS-PEO (DBE-621)	No	
PDMS-PEO (DBE-311)	No	
PDMS-PEO (DBE-224)	No	
Styrene-butadiene-methacrylate (SBM)	No	
PEO-PPO-PEO(M_w = 5800)	Yes	Translucent
PEO-PPO-PEO(M_w = 14600)	No	
PEO-PPO-PEO(M_w = 2800)	Yes	Translucent
PEO-PPO-PEO(M_w = 1900)	Yes	Translucent
PCL-PTHF-PCL	Yes	Opaque
Polylauryllactam-PTHF	Yes	Transparent
PMMA-PBuA-PMMA (M51)	Yes	Translucent
PMMA-PBuA-PMMA (M52)	Yes	Transparent
PMMA-PBuA-PMMA (M53)	Yes	Translucent
PEO-PPO-PDMS-PVMS (DBP-V102)	No	
Carbinol(-OH) terminated PDMS (DBE-C25)	Yes	Translucent
Acryloxyl terminated PDMS (DBE-U12)	No	

Table 2.2 Solubility and phase-separation results for homopolymers and block-copolymers used as additives in stereolithographic resin formulations.

Interestingly, a high molecular weight (20,000 g/mol) PDMS-PEO-PPO block copolymer is miscible in the uncured Clear V4 resin. It is a brush block copolymer with a backbone of polydimethylsiloxane grafted with polyethylene oxide. Polyethylene oxide accounts for 70% of its weight. Commercial SLA resins often consist of reactive diluents, such as tripropylene glycol diacrylate (TPGDA) or hexanediol diacrylate (HDDA), that

reduce the viscosity and increase the reactivity.[71, 72] Polyethylene oxide has a chemical structure and solubility parameter similar to diluents. Consequently, the presence of polyethylene oxide enhances the miscibility of the block copolymer in the SLA resin. According to Flory-Huggin's theory for a polymer-monomer blend, the entropic contribution to the free energy of mixing is negligible and the miscibility of polymer-monomer blend depends mainly on the enthalpic contribution. Polymer and monomers with comparable solubility parameters have favorable enthalpic interactions and are miscible.[73] As a result, lower molecular weight block copolymers are readily miscible in the Clear V4 resin, whereas higher molecular weight block copolymers are miscible only when compatible functional groups are present.

Moreover, most of these additives also remain miscible in the cured Clear V4 resin and result in transparent samples after SLA printing. Only a few block copolymers generate phase-separated domains in the SLA printed thermoset and these samples appear translucent. These selected block copolymers, highlighted in Table 2.2, were evaluated further as potential impact modifiers using fracture toughness testing.

Figure 2.1-(a) shows the linear elastic fracture toughness (K_q) for acrylate thermosets SLA printed using the impact modified resins. SLA printed materials exhibit strength anisotropy where failure can occur preferentially along the interface between layers. Therefore, impact properties were investigated using compact tension specimen such that loading direction is perpendicular to the interface and pre-crack is parallel to the interface. This allows evaluation of fracture toughness when a crack propagates along the weaker interface.

The unmodified Clear V4 resin shows a catastrophic brittle failure with a fracture toughness of 0.75 MPam$^{1/2}$. Fracture toughness improves by 20 to 60% for SLA resins modified with the screened impact modifiers. Notably, impact modified SLA resin with block copolymer DBP-732 shows the most significant improvement of 60%. This improvement results from DBP-732 phase-separating into domains with the appropriate size and interparticle spacing, providing effective soft particle toughening.[25]
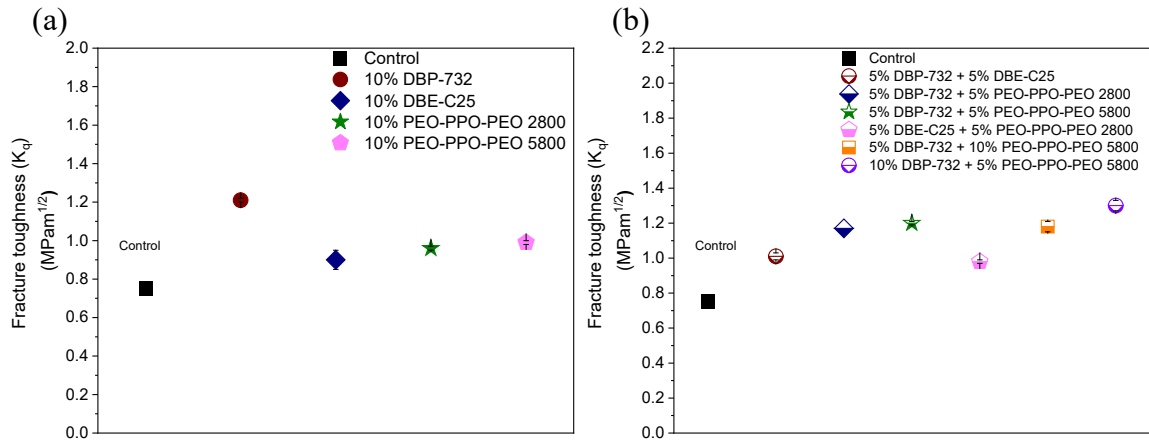
Figure 2.1 Linear elastic fracture toughness (K$_q$)values for Clear V4 resin formulations containing homopolymer and block-copolymeric additives.

Block copolymers self-assemble in ordered, micellar structures upon phase-separation from the matrix.[74] The morphology of phase-separated domains affects the impact properties. In addition to optimizing the particle size and interparticle spacing, altering the particle shape provides opportunities to further improve the impact properties and is discussed in detail in Chapter 3. Recent studies have demonstrated that irregular micellar particles, such as disk-sphere or disk-cylinder, can be obtained by blending two block copolymers in a solution.[75, 76] Blending of two additives in Clear V4 resin can provide unusual phase-separated domains that facilitate enhanced particle-particle interactions and thereby, improved impact properties. Figure 2.1-(b) shows the fracture toughness for impact modified SLA resins prepared by blending the commercially available Clear V4

resin with a combination of two additives. Incorporation of two additives results in similar enhancements in the impact properties as that of a single additive, suggesting a lack of synergistic performance between the additives investigated here. Investigation of different additives indicates that DBP-732 is the most suitable candidate as an impact modifier. As a result, consequent studies focus on the effect of the concentration of DBP-732 on the impact, thermal, and mechanical properties of SLA printed acrylate thermosets.

2.3.2 Impact properties of DBP-732-containing SLA printed acrylate thermosets

Impact modified SLA resins were prepared by mixing the Clear V4 resin with 0 to 20% concentrations of the block copolymer DBP-732. Figure 2.2 shows the linear elastic fracture toughness (K_q) for acrylate thermosets as a function of the concentration of DBP-732. Fracture toughness increases proportionally with the concentration of DBP-732 up to 15% concentration and steadily declines with further increase in the concentration. SLA resin modified with 15% of DBP-732 obtains the highest improvement in the fracture toughness (1.31 MPam$^{1/2}$) compared to the unmodified resin (0.75 MPam$^{1/2}$). Size, interparticle spacing, and concentration of phase-separated domains are interdependent.[77] Increase in the concentration of DBP-732 results in an increase in the size of phase-separated rubbery domains and a decrease in the inter-particle spacing. Particles smaller than the optimum size are difficult to cavitate and cavitation of domains is necessary to initiate the energy absorption processes, such as matrix yielding. Particles larger than the optimum size act as defects. Therefore, impact properties depend on the particle size and typically reach a maximum at an optimum particle size.[78] SLA resins modified with DBP-732 show similar particle size dependence on the impact properties and achieve the highest

fracture toughness at an optimum concentration that generates the optimum size and interparticle spacing of phase-separated rubbery domains.
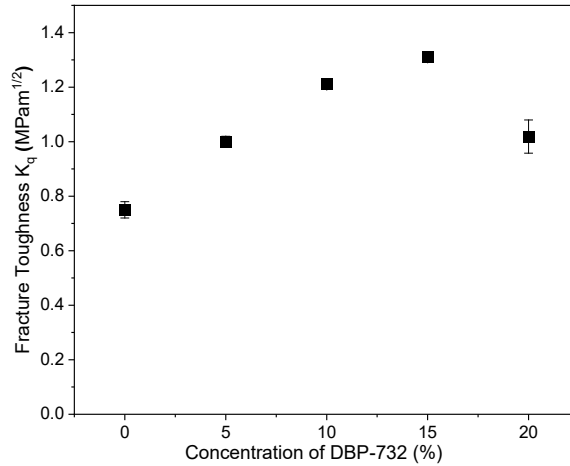
Figure 2.2 Linear elastic fracture toughness (K_q) measured for SLA printed acrylate thermosets as a function of DBP-732 concentration.

Additionally, acrylate thermosets when SLA printed using the unmodified Clear V4 resin appear transparent, and when printed using the impact modified Clear V4 resin appear opaque. After fracture toughness testing, the unmodified samples show a crack formation and the modified samples show a white color region in front of the crack tip, as shown in Figure 2.3. During the failure event, rubbery domains in front of the crack tip cavitate and relieve the triaxial state of stress. It allows surrounding matrix material to yield and undergo plastic deformation *via* formation of crazes or shear bands. These cavitated domains scatter light and form a diffuse white color process zone.[79]
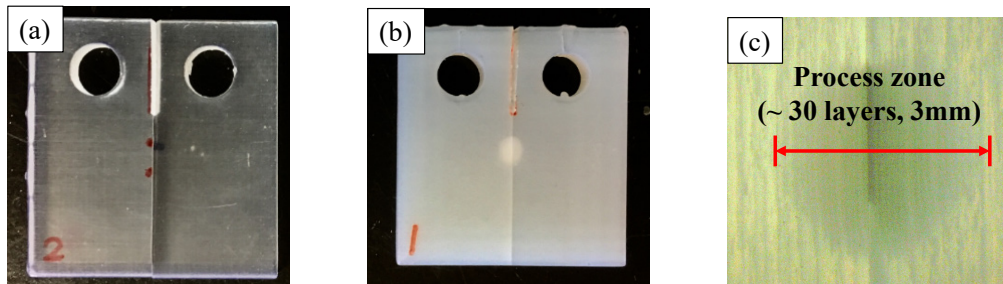
Figure 2.3 Compact tension tested specimen for (a) unmodified Clear V4 resin, (b) Clear V4 resin containing 15% of DBP-732, and (c) Optical micrograph of process zone for acrylate thermoset printed using Clear V4 resin containing 15% of DBP-732.

Figure 2.3-(c) shows the process zone in front of the crack tip characterized using optical microscopy. Process zone appears darker compared with the surrounding matrix and it involves 30 layers (~3 mm, 30 layers of 100 um each). This shows that a large volume of the matrix material is involved in the energy dissipation processes and leads to the enhanced energy absorption. Optical microscopy allows the qualitative observation of the plastic deformation that occurs in the impact modified materials.

Additionally, Figure 2.4 shows load versus extension curves for SLA printed acrylate thermosets and describes the effect of DBP-732 concentration on the sample failure. Impact modified SLA resins exhibit higher maximum load and fail at two times higher strains compared with the unmodified SLA resins. Notably, SLA resins modified with 15% or 20% of DBP-732 show linear elastic as well as non-linear plastic regions.
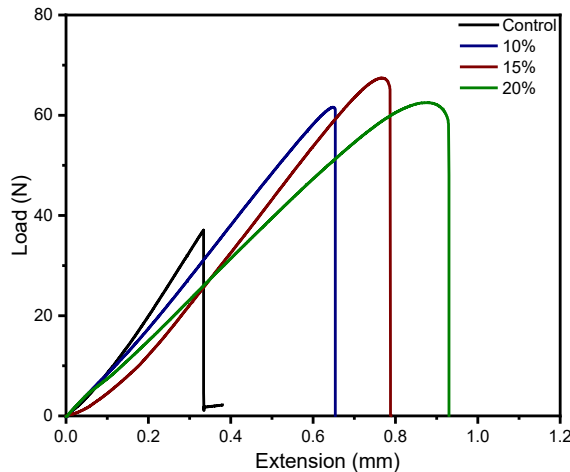
Figure 2.4 Representative load versus extension curves recorded for SLA printed acrylate thermosets at increasing concentrations of DBP-732.

Such non-linear mechanical response results from irreversible plastic deformation. Suitable particle size and interparticle spacing is required for plastic deformation to occur and therefore, it occurs only when the impact modified SLA resins contain optimum 15% or higher concentrations of DBP-732. Unmodified SLA resin exhibits brittle failure in the

linear elastic regime and energy dissipation occurs only *via* creation of a new surface area. Impact modified SLA resins fail in a ductile manner and dissipate energy in creation of a new surface area and matrix yielding. To take into account this plastic deformation, it is necessary to evaluate the non-linear fracture energy release rate for impact modified SLA printed thermosets.[80]

Figure 2.5 shows the fracture energy release rate (G_q or J_q) for impact modified SLA printed acrylate thermosets. Linear fracture energy release rate (G_q) was evaluated when printed using the unmodified Clear V4 resin or Clear V4 resin modified with 5% or 10% of DBP-732. Non-linear fracture energy release rate (J_q) was determined for SLA resins modified with 15% or 20% of DBP-732. It considers linear elastic as well as non-linear plastic energy consumption that occurs during the failure of these samples.[80]
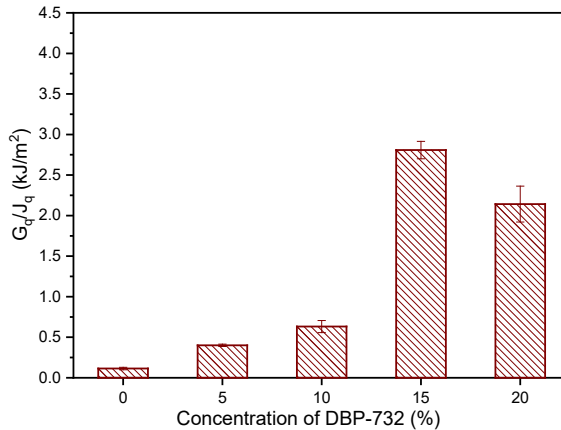
Figure 2.5 Fracture energy release rate (G_q or J_q) for 3D printed acrylate thermosets as a function of DBP-732 concentration.

Fracture energy release rate increases with an increase in the concentration of DBP-732 up to 15% concentration and declines with further increase in the concentration. Notably, impact modified SLA resin containing 15% of DBP-732 obtains an order of magnitude higher J_q of 2.8 kJ/m^2 compared with G_q of 0.1 kJ/m^2 for the unmodified SLA resin. J_q shows a similar trend as K_q where particle size, concentration, and inter-particle

spacing govern the energy absorption. Incorporation of a second, rubbery phase decreases the matrix yield stress and reduces the energy barrier for yielding.[28] Specifically, the applied stress required for yield initiation decreases linearly and stress required for yield percolation decreases logarithmically with the concentration of the rubbery phase, as discussed in Chapter 1. As a result, SLA thermosets when modified with the optimum concentration achieves the percolation of yield fronts which originate at the surface of cavitated domains and enhanced particle-particle interactions. Further, matrix yielding is a thermally activated stress-induced phenomenon.[81] Matrix yielding in front of the crack tip increases the local temperature that enables the surrounding matrix to flow and yield. It results in a pseudo-macroscopic yielding that involves a larger volume of the matrix material. Engineering the SLA printed thermosets with appropriate morphology for rubbery domains results in plastic deformation and thereby, significant improvements in the impact properties.

The mechanical properties of SLA printed materials depend on printing parameters including the layer thickness, orientation, laser intensity, and laser spot size.[82] These parameters are selected based on the desired print accuracy, print time, and mechanical properties.[83] SLA process makes materials by layer-by-layer assembly of UV cured layers and generates interfaces between the layers. These interfaces have intrinsically lower cohesive strength compared with the bulk of the layer and lead to anisotropic strength.[53] This manifests in poor mechanical properties in the print direction in comparison with the print plane. Further, mechanically weaker interfaces are more prone to catastrophic crack propagation *via* layer delamination or fracture.[84] Therefore, when the material is loaded perpendicular to the interface, crack propagation can occur along the interface before the

localized matrix yielding. The key challenge for the impact modification of SLA printed materials is to achieve improved fracture toughness even when a material is loaded parallel or perpendicular to the interface.

To investigate the anisotropy associated with the impact properties of SLA printed thermosets, fracture toughness tests were conducted for compact tension specimens printed with pre-crack parallel, perpendicular, or at 45° angle with respect to the interface, as shown in Figure 2.6. These samples were printed with a layer thickness of 25 um and 100 um.

Parallel   Perpendicular   45°
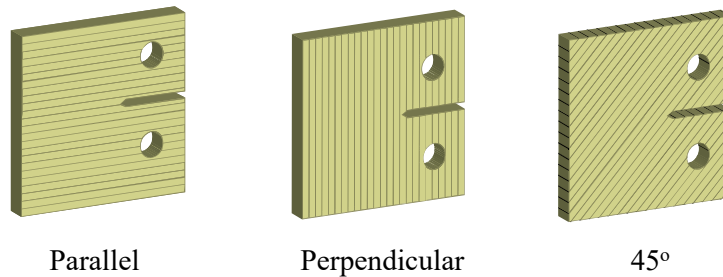
Figure 2.6 Compact tension specimens with pre-crack oriented parallel, perpendicular, and at 45° with respect to the print interface, respectively.

Figure 2.7 shows the fracture energy release rate for the unmodified SLA resin and the SLA resin modified with the optimum concentration (15%) of DBP-732 as a function of print layer orientation and thickness. SLA printed thermosets using the unmodified Clear V4 resin at 100 um layer thickness achieve G_q of 0.1 kJ/m^2 (parallel orientation), 0.2 kJ/m^2 (perpendicular orientation), and 0.18 kJ/m^2 (45° orientation). These samples show anisotropic properties where the lowest impact properties are observed when a crack propagates parallel to the interface. These thermosets are thermally post-cured after the SLA printing to ensure complete curing. Post-curing also improves the cohesion between the layers and minimizes the anisotropy of strength. Therefore, the variations in the impact

properties for the unmodified SLA resins when printed at different orientations are marginal.

Notably, impact modified SLA resins exhibit comparable, an order of magnitude improvements in the impact properties irrespective of the layer orientation and thickness. Impact modified SLA resins when printed with 25 um layer thickness generates more interfaces and thereby, more regions of weaker cohesion. These interfaces with lower free energy provide the least resistance path for crack propagation, especially when loaded in parallel and 45° configuration. As a result, thermosets printed with 25 um layer using the impact modified resins show more pronounced anisotropic impact properties, where J_q increases from parallel (2.3 kJ/m^2) to 45° (2.6 kJ/m^2) to perpendicular (2.8 kJ/m^2) orientation. Nonetheless, impact modified SLA resins form the process zone in front of the crack tip and show non-linear load versus extension response. It shows that these materials yield before the rapid crack propagation. Optimized particle concentration, size, and inter-particle spacing results in isotropic toughness enhancement for the SLA printed materials.
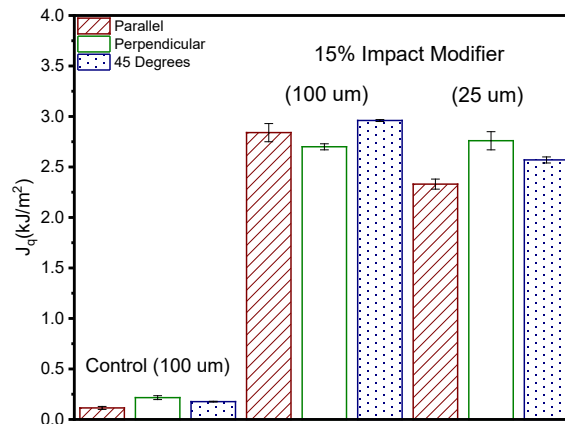
Figure 2.7 Fracture energy release rate (J_q) for acrylate thermoset printed using Clear V4 resin containing 15% of DBP-732 as a function of print layer thickness and print layer orientation with respect to the pre-crack.

2.3.3 Morphological and fractographic characterization of impact modified SLA printed acrylate thermosets

Figure 2.8 shows the scanning electron micrographs for thermosets printed using the SLA resins modified with 10%, 15%, and 20% of the DBP-732 and with a layer thickness of 100 um. Darker voids in the micrograph cross-section represent the phase-separated domains. DBP-732 phase-separates in smaller domains with sizes ranging from 100 to 150 nm.
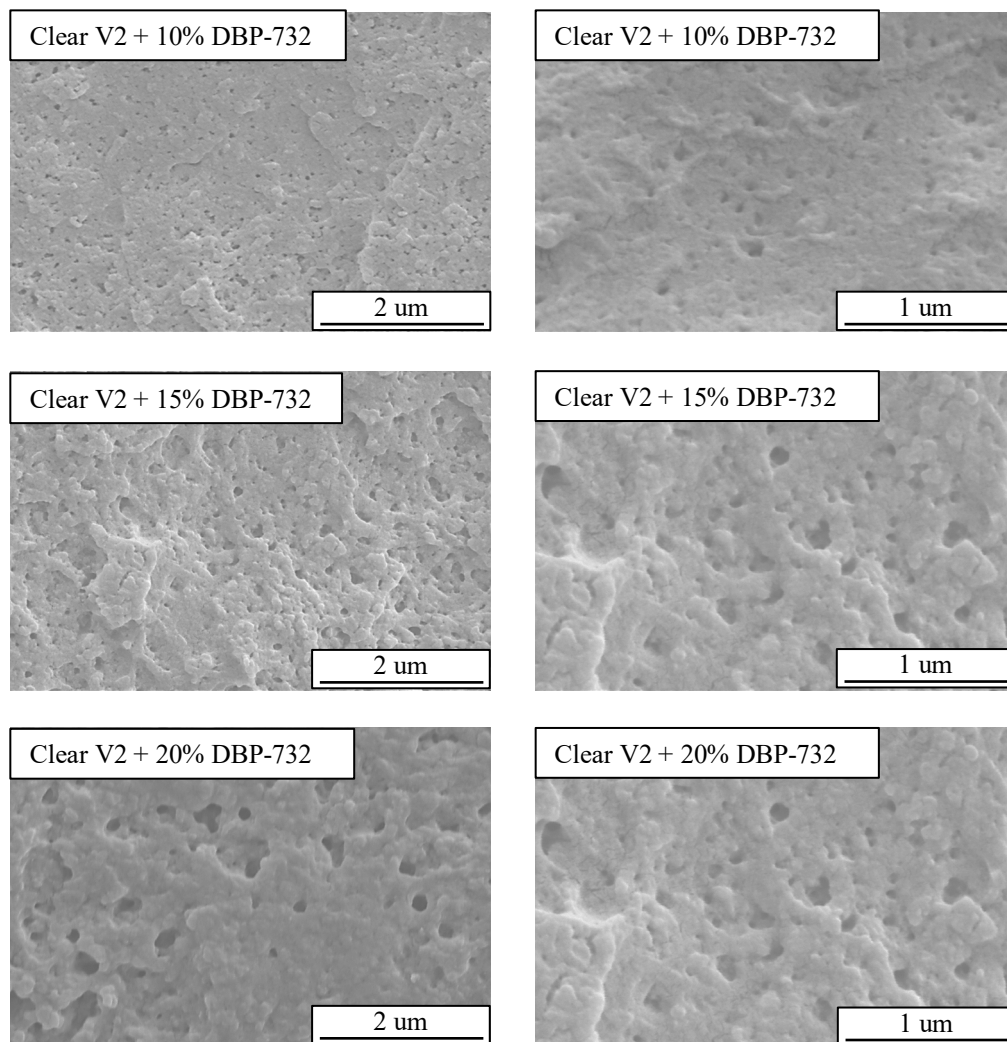
Figure 2.8 Morphology for acrylate thermosets printed using Clear V4 resin containing 10%, 15%, and 20% of DBP-732, respectively.

The length scale of phase-separated domains depends on the curing kinetics, mismatch in the solubility parameter, molecular weight of the additive, and the concentration.[85, 86] SLA printing is a rapid photo-curing process. DBP-732 is miscible in the SLA resin before curing and undergoes reaction induced phase-separation to generate domains during the photopolymerization. These submicron size domains get kinetically trapped as the surrounding material crosslinks. Further, the size of phase-separated domains increases with the concentration of DBP-732. The coalescence of domains *via* Ostwald ripening results in larger domain sizes at higher concentrations.[87] These domains are primarily spherical and some domains also exhibit ellipsoidal, distorted, and irregular shapes. Notably, non-spherical domains are more apparent at higher concentrations. These domains form when the coalescence of domains gets kinetically trapped during the photopolymerization.

These SEM images were further analyzed using Image-J to quantify the effect of the concentration of DBP-732 on domain sizes. For each formulation, the perimeter for approximately 200 domains was measured and radius R_p was determined using Equation 2.5. Figure 2.9 shows the size (R_p) distribution for acrylate thermosets printed using the SLA resin containing 10%, 15%, and 20% of DBP-732. R_p for phase-separated domains ranges from 25 to 100 um for the SLA resin modified with 10% of DBP-732. At higher concentrations of 15% and 20%, domains with R_p up to 200 um are present. Impact modified SLA resins exhibit the average R_p of 50 nm at 10%, 57 nm at 15%, and 64 nm at 20% concentration of the DBP-732. The average particle size ($R_{p\text{-avg}}$) increases with the concentration of the DBP-732.

Equation 2.5: $R_p = \frac{P}{2\pi}$ (where P is the perimeter of the particle)
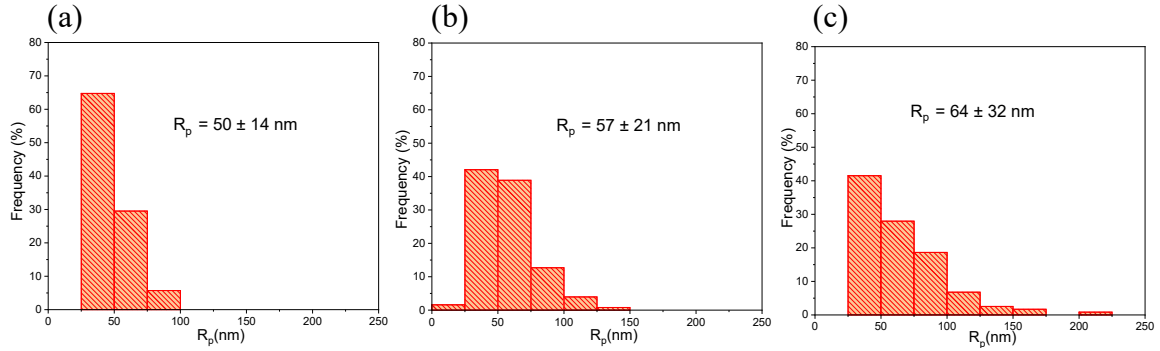
Figure 2.9 Particle size (R_p) distribution for acrylate thermosets printed using Clear V4 resin containing (a)10%, (b)15%, and (c) 20% of DBP-732, respectively.

We assume that the phase-separated domains are dispersed in the matrix in a simple orthogonal model. Therefore, the interparticle spacing between the domains was determined using Equation 2.6.[77] The domain size, the interparticle spacing between the domains, and the concentration of the impact modifier are interdependent variables.[77] Particle size of rubbery domains increases and the interparticle spacing between the domains decreases with an increase in the concentration of the impact modifier DBP-732, as tabulated in Table 2.3.

Equation 2.6: $\dfrac{S}{D} = \left(\dfrac{\pi}{6C}\right)^{\frac{1}{3}} - 1$

Concentration of DBP-732 (%)	Average particle size (R_P) (nm)	Interparticle spacing (nm)
10 %	50	39
15 %	57	33
20 %	64	29

Table 2.3 Average particle size (R_p) and interparticle spacing for acrylate thermosets printed using the Clear V4 resin containing10%, 15%, and 20% of DBP-732.

Morphology analysis for impact modified SLA printed thermosets shows the highest improvement in the fracture toughness performance occurs with the optimum particle size of 57 nm, the optimum interparticle spacing of 33 nm, and the optimum concentration of 15%. This particle size results in the cavitation of rubbery domains before

39

the material failure. Once these domains are cavitated, yield initiates at the surface of these domains. Optimum inter-particle spacing improves the particle-particle interactions and allows the yield fronts to percolate. The phase-separated domains must have the appropriate particle size and spacing such that a large volume of the matrix is involved in energy dissipation. For SLA printed thermosets it occurs when the SLA resin is modified with 15 % of DBP-732.

Impact modified SLA resins exhibit comparable improvements in the impact properties irrespective of the layer orientation and thickness when engineered with the optimized domain morphology. Alharbi *et al.* observed comparable flexural strengths for vertically and horizontally printed SLA parts as well. However, these vertically and horizontally printed parts showed variation in their failure processes.[84] Therefore, a fractographic analysis was performed on SLA printed thermosets to understand the effect of strength anisotropy on failure mechanisms that occur. Figure 2.10 shows the optical images of the process zone for SLA printed thermosets when printed with a crack orientation parallel or perpendicular or 45° with respect to the print interface and with a 100 um layer thickness.

During a failure, phase-separated domains in front of the crack tip cavitate or de-bond to relieve the hydrostatic state of stress. These cavitated or de-bonded rubbery domains scatter light and therefore, the process zone appears darker under the optical microscope. Interestingly, the process zone appears to have advanced along the layer interfaces. For example, the process zone spans top to bottom for parallel orientation, left to right for perpendicular orientation, and at an angle for 45° orientation. It indicates that damage mainly occurs at an interface or in the vicinity of an interface. Pseudo-macroscopic

40

process zone results from a stable crack growth as the surrounding material yields unlike catastrophic brittle failure for the unmodified SLA resin.
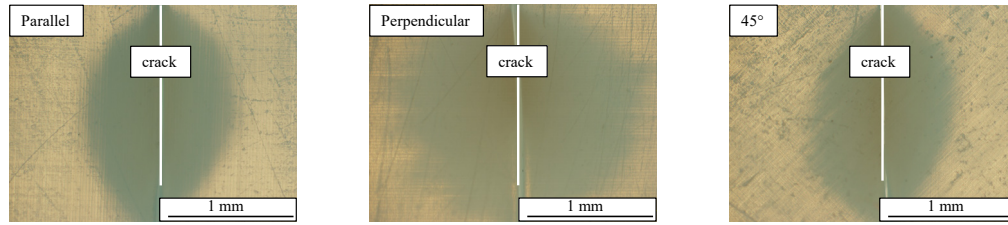
Figure 2.10 Optical micrographs of process zone for acrylate thermosets printed using Clear V4 resin containing 15% of DBP-732 when pre-crack is oriented parallel, perpendicular, and 45° with respect to the printed interface, respectively.

These process zones were isolated, microtomed, and imaged to probe the failure processes that occur at the interface. Microtoming gives a cleaner surface which when looked under the optical microscope shows individual SLA printed layers. It allows us to determine the role of an interface in energy absorption. Additionally, the damage that occurs at the interface farthest from the crack tip resembles the early-stage damage onset that occurs in front of the crack tip. Figure 2.11 shows the process zone for thermoset printed using the SLA resin containing 15% of DBP-732 with a layer thickness of 100 um. In this compact tension specimen, pre-crack is parallel to the printed interface. Figure 2.11-(a) represents the part closer to the support, whereas Figure 2.11-(b) shows the part farthest from the support. These images clearly show individual layers with a thickness of 100 um. The darker regions denote the de-bonded or cavitated rubbery domains. This darker region represents the location of the phase-separated domains. Interestingly, phase-separated domains appear to have preferentially localized on the one side of an individual layer. These domains are localized on the side of a layer that is closer to the support and along the interface adjacent to the previously printed layer. The stress field in front of the crack tip is symmetric. However, preferential localization of domains is not symmetric rather it

41

is always on the support side of a layer. This suggests that localization of these domains results from the print process.
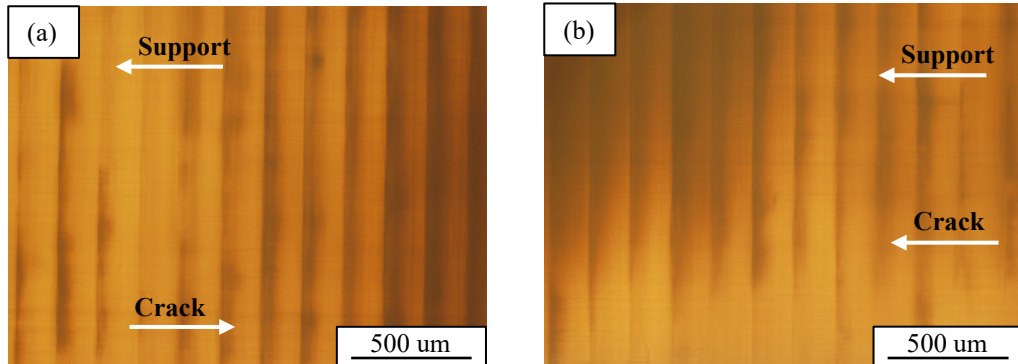
Figure 2.11 Optical micrographs for acrylate thermosets printed using Clear V4 resin containing 15% of DBP-732 with pre-crack oriented parallel with the printed interface (a) process zone closer to the support (left) with a crack on right, (b) process zone farther from the support (left) with a crack on left.

Further, Figure 2.12 and Figure 2.13 show the process zone for thermosets printed using the impact modified SLA resin at a layer thickness of 25 um and 100 um and with a pre-crack orientation parallel, perpendicular, and at 45° with respect to the interface. Phase-separated domains localize along one side of an interface irrespective of layer thickness and pre-crack orientation.
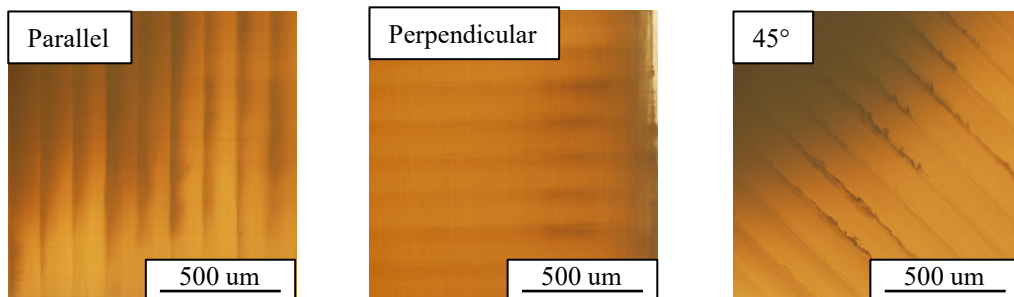
Figure 2.12 Microtomed process zone for acrylate thermosets printed with 100 um layer thickness using Clear V4 resin containing 15% of DBP-732 when pre-crack is oriented parallel, perpendicular, and 45° with respect to the printed interface, respectively.
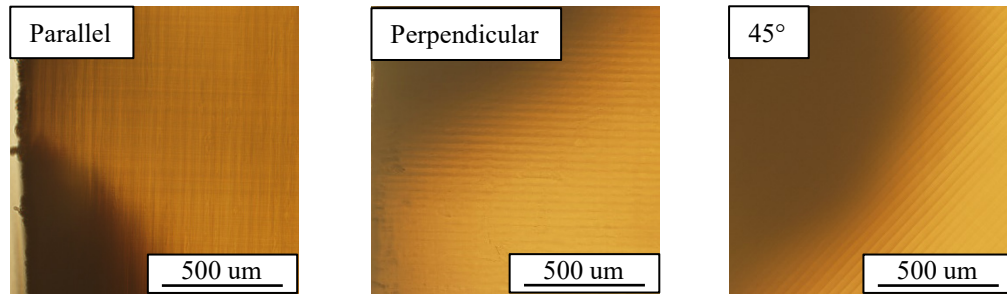
Figure 2.13 Microtomed process zone for acrylate thermosets printed with 25 um layer thickness using Clear V4 resin containing 15% of DBP-732 when pre-crack is oriented parallel, perpendicular, and 45° with respect to the printed interface, respectively.

Block copolymer DBP-732 is miscible in the uncured SLA resins. The process of SLA printing creates a mismatch in the solubility parameter between the impact modifier and the partially/completely cured matrix. As a result, there is a driving force for DBP-732 to phase-separate. Additionally, DBP-732 is a liquid at room temperature. It has a lower density than a completely cured acrylate thermoset. As a result, we hypothesis that phase-separated domains migrate to the top of a layer (closer to the support) as a layer starts to cure from the laser below, as shown in schematic 2.14. These domains get trapped at the top of a layer as the surrounding matrix cures.
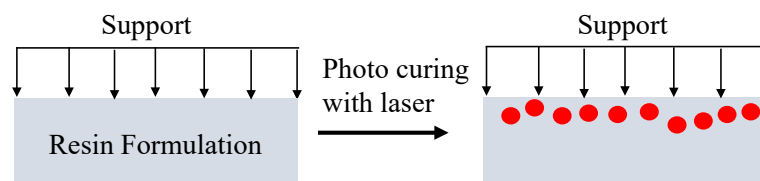
Figure 2.14 Schematic for hypothesized SLA printing process during the formation of each layer that results in the localization of phase-separated domains.

2.3.4 Thermal and mechanical properties of impact modified acrylate thermosets

DMA differentiates between the elastic and the viscous properties of a material. It provides a macroscopic mechanical response. Whereas DSC utilizes microscopic specific heat measurements to determine the transition temperatures. Therefore, DMA is a more

sensitive characterization technique than DSC and it was used to measure the T_g for impact modified SLA printed thermosets. Figure 2.15 shows the tan delta as a function of temperature for thermosets printed using the SLA resins modified with 5%, 10%, 15%, and 20% of DBP-732. The temperature corresponding to the tan delta peak was ascribed as the T_g.

T_g scales with the extent of curing for crosslinked amorphous polymers.[88] Unmodified SLA resin shows the T_g of 115 °C and it is comparable with the T_g of thermoplastic polyacrylates, such as polymethyl methacrylate (PMMA).[89] This confirms complete curing for the SLA printed thermosets. T_g for impact modified SLA resins marginally decreases with an increase in the concentration of DBP-732 up to 15%. T_g decreases dramatically (~15 °C) at a higher concentration (20%) of DBP-732, as shown in Table 2.4. Further, DBP-732 exhibits a very low T_g and it lies outside the operating temperature range for DMA.[90]
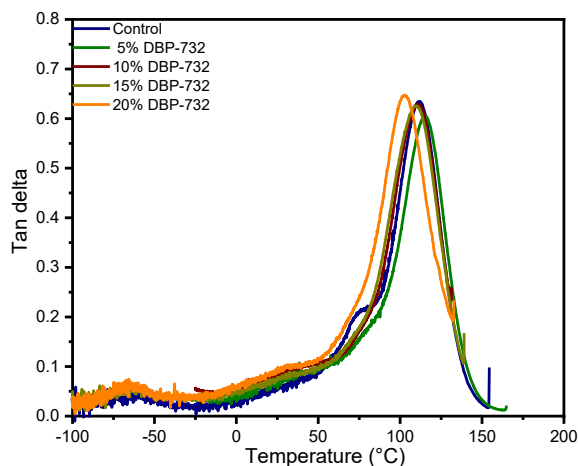
Figure 2.15 Tan delta as a function of temperature measured for SLA printed acrylate thermosets printed using Clear V4 resins modified with DBP-732.

Completely phase-separated polymer blends show two distinct T_g's corresponding to each phase. Plasticization of a polymer matrix with an additive reduces its T_g. Morphological characterization shows phase-separated DBP-732 domains and DMA

44

analysis shows comparable T_g's for the SLA resin modified with up to 15% of DBP-732.

DBP-732 when incorporated at concentrations of up to 15% primarily present as a second, rubbery phase. However, at higher concentrations (>15%), some fraction of DBP-732 remains miscible in the crosslinked matrix and acts as a plasticizer.

Concentration of DBP-732 (%)	Glass transition temperature (T_g) (°C)
Control	115
5 %	115
10 %	108
15 %	111
20 %	102

Table 2.4 Glass transition temperatures (T_g) determined using DMA for acrylate thermosets printed using Clear V4 resins modified with DBP-732.

Impact modified SLA thermosets were characterized using non-standard compression testing. Mechanical properties, such as elastic modulus, yield stress, and strain hardening modulus were determined from the recorded stress versus strain response, as shown in Figure 2.16.
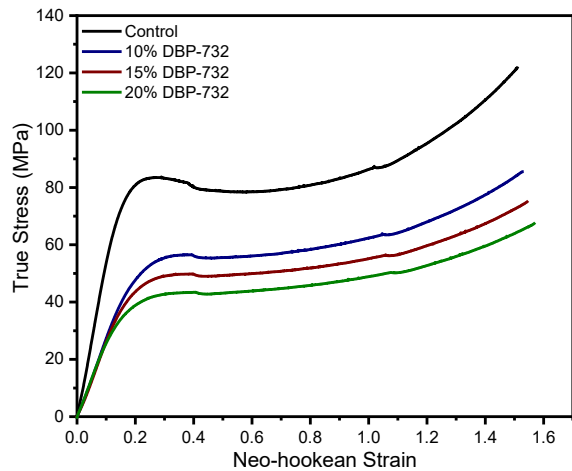
Figure 2.16 Representative true stress versus neo-Hookean strain curves recorded for SLA printed acrylate thermosets at increasing concentrations of DBP-732.

Impact modified SLA thermosets show poor mechanical properties in comparison with SLA printed thermosets using the unmodified SLA resins. Elastic modulus and yield stress decrease with the concentration of DBP-732, as shown in Figure 2.17-(a). Values

reported here are normalized with respect to the weight fraction of the matrix to consider only the matrix contribution. These properties show a significant reduction (40%) even at the smallest concentration (10%) of DBP-732 and reduce further with an additional increase in the concentration. Although a reduction in yield stress inherently increases the material toughness, lower stiffness values are undesirable.[55]

Plasticizer reduces the elastic modulus and the yield stress in proportion with its concentration.[91, 92] Concentration of DBP-732 that stays miscible in the cured thermoset increases with its concentration in the uncured SLA resin. The fraction of DBP-732 that remains miscible in the cured thermoset plasticizes the network and reduces the elastic modulus and the yield stress. Besides, numerical simulation studies demonstrate that voids or pores decrease the elastic stiffness and the yield stress in proportion with their volume fraction.[93] DBP-732 is a liquid block copolymer with negligible stiffness and yield stress. It can be considered as a void. Thus, the presence of these voids further reduces the mechanical properties.
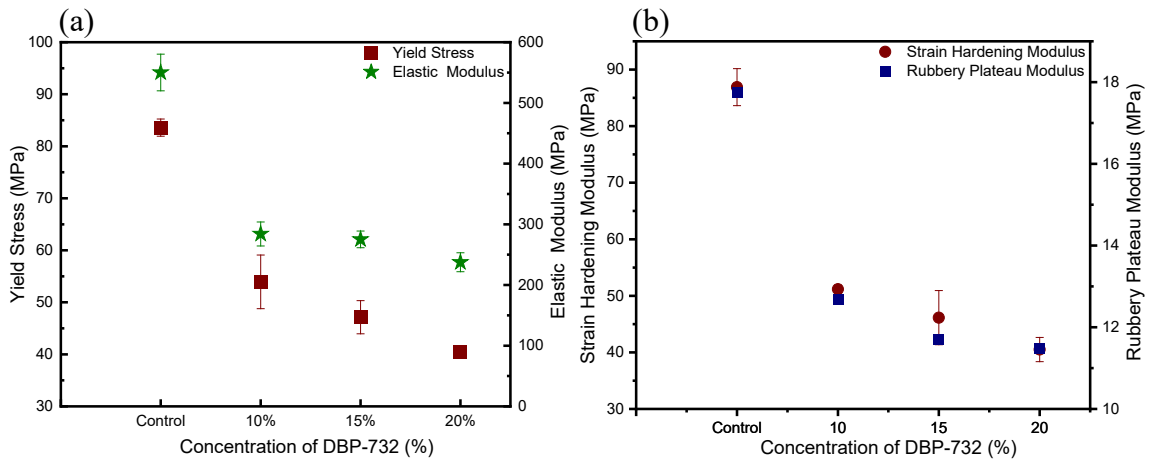
Figure 2.17 Mechanical properties measured for SLA printed acrylate thermosets at increasing concentrations of DBP-732 (a) Elastic modulus and yield stress; (b) Strain hardening modulus and rubbery plateau modulus.

Compression testing is beneficial to probe non-linear mechanical properties of glassy polymers which are inaccessible in tensile testing. In tensile testing, flaws or defects are activated and glassy materials fail in the linear regime. Figure 2.17-(b) shows strain hardening modulus and rubbery plateau modulus for the impact modified SLA thermosets. Rubbery plateau modulus was determined as the storage modulus value at T_g + 40 °C recorded during DMA. Even the non-linear properties significantly decrease at the smallest concentration (10%) of DBP-732 and reduce further with an increase in the concentration. These non-linear properties reflect network connectivity and scale inversely with the molecular weight between crosslinks.[94] Reduction in strain hardening modulus results from the higher molecular weight between the crosslinks. Network connectivity or molecular weight between crosslinks depends on the extent of curing. For complete curing to occur during the SLA printing, all the photo-initiators must dissociate into reactive radicals. These radicals must react with oligomers and monomers to form a crosslinked network. This process of photopolymerization depends on various factors, such as laser absorption, competing reactions, and rate of reaction.[95] Impact modifier DBP-732 dilutes the concentrations of reacting species in the SLA resin. This can result in lower crosslink density and thereby, strain hardening modulus. In addition, the precise interaction between the impact modifier DBP-732 and the photo-initiator is unknown. Possible interference of DBP-732 with photo-polymerization can lead to incomplete photo-curing.

Uniaxial compression test also provides insights into the intrinsic deformation behavior of glassy thermosets. Materials that can undergo stable local deformation fail in a ductile manner. Materials that undergo homogeneous deformation fail in a brittle manner.

The ability of the material to undergo stable macroscopic deformations can be predicted using the post-yield response generated during the compression test.

Recent studies consider the effect of strain softening and strain hardening to predict whether material exhibits homogeneous deformation or stabilized local deformation.[94, 96, 97] They described a strain localization criterion. It estimates the draw ratio (λ) required to achieve a stable neck formation. For example, thermal annealing or physical aging increases the strain softening. Therefore, material needs to be drawn significantly before a stable neck can form. In such cases, materials might fail before the stabilized local deformation. Glassy thermosets primarily exhibit plastic deformation *via* shear band formation instead of geometric necking during the compression testing. Therefore, the strain localization criterion was modified for shear band stability, as shown by Equation 2.7.[98] Strain softening (post-yield stress drop) induces the strain localization. Strain hardening stabilizes the plastic deformation, such as yielding, necking, and crazing. The balance between strain softening and strain hardening dictates the shear band stability.

Equation 2.7: $\dfrac{\sqrt{2}\sigma_r}{3G} = \dfrac{\left(\lambda - \frac{1}{\lambda}\right)}{\left(K_y - 1\right)}$

where, σ_r is the rejuvenated stress; G is the shear modulus; K_y is the ratio of yield stress to rejuvenated stress; draw ratio (λ) is the ductility parameter.

Figure 2.18 shows the draw ratio (λ) for impact modified SLA thermosets. Strain softening decreases with the concentration of DBP-732. It reduces the draw ratio (λ) for impact modified SLA thermosets. This means a stable neck or shear band forms at lower strains for impact modified SLA thermosets. This behavior is similar to ductile

polycarbonate. Further studies are necessary to decipher the role of DBP-732 in network deformation.
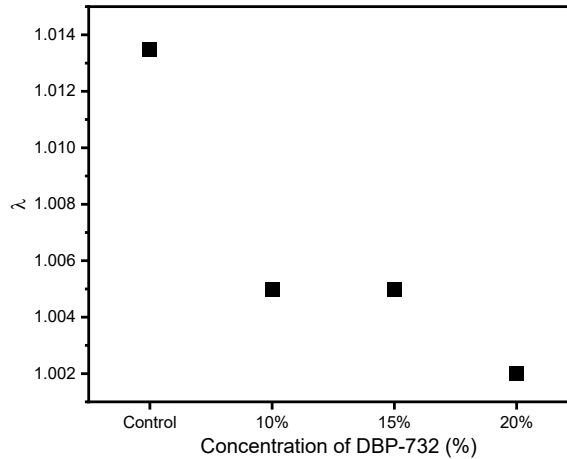
Figure 2.18 Draw ratio (λ) for SLA printed acrylate thermosets at increasing concentrations of DBP-732.

2.4 Conclusions

We identified different homopolymer and block copolymeric additives that achieve soft particle toughening for SLA printed acrylate thermosets. These additives are engineered to undergo RIPS that results in the phase-separated domains of appropriate size and interparticle spacing.

Specifically, SLA resins modified with a brush block copolymer DBP-732 results in an order of magnitude (~10 times) higher fracture energy release rate in comparison with the unmodified resin. This impressive toughness enhancement results from the plastic deformation that occurs during the failure and it is engineered by modifying the SLA resin with an optimum concentration (15%) of DBP-732. This concentration generates phase-separated rubbery domains with an optimum particle size of 57 nm and an optimum interparticle spacing of 33 nm necessary for effective toughening.

In addition, the SLA printing process appears to result in the localization of these domains at the interface between the layers. This possibly leads to the strengthening of the interface. Notably, impact modified SLA resins achieve isotropic toughness enhancements. Superior impact properties are achieved irrespective of the layer orientation and layer thickness. Thermal and mechanical characterization reveals that DBP-732 affects photopolymerization and may plasticize the network when incorporated at high concentrations.

Overall, incorporation of the impact modifier DBP-732 increases the ductility of SLA printed materials and eliminates the strength anisotropy to make the SLA process more suitable for demanding applications.

2.5   Future work

This chapter investigated the soft particle toughening for stereolithographic 3D printing and showed that significant toughness enhancements are achieved for optimized morphology of rubbery domains. However, SLA technology is still in its early stages and there remain a lot of opportunities to make it as applicable as injection molding. Therefore, future studies will be required to further develop the understanding of the SLA process and to identify novel routes for improving the mechanical properties of SLA printed parts.

Morphological investigation for impact modified SLA resins suggests that the phase-separated domains generated during the SLA printing localize at the interface between the layers. This phenomenon can be studied for different additives that are miscible in the SLA resin before curing but phase-separates during photopolymerization to form interesting morphologies. For example, recent studies have shown that desoxyanisoin

is miscible in an epoxy resin but phase-separates *via* RIPS to form needle-like, highly anisotropic crystals.[99] Future studies can focus on developing additives that will result in the formation of such needle-like crystals at the interface. This will improve the stiffness of SLA printed materials and find use in applications where anisotropic strength is required.

SLA printers with a high resolution can achieve a smaller spot size than the Form 2 printer. This spot size determines the extent of details that a printer can print. With SLA printing, it is possible to print material with voids. Dimensions of this void primarily depend on laser spot size among other factors. A high-resolution printer can print materials with submicron or even 100 nm voids. In the case of impact modified SLA resins studied here, toughness improvements are achieved with ~100 nm domains. Future work can focus on templated toughening *via* fabricating a material with such voids. A systematic investigation should be conducted to evaluate the effect of size, interparticle spacing, and concentration of voids on mechanical properties, such as modulus and toughness. Previous studies have studied epoxy composites containing glass beads. They observed diffuse shear yielding around the glass beads.[42] Similar effects can be studied for SLA printed glassy thermosets with templated voids.

CHAPTER 3

ENGINEERING NEXT-GENERATION IMPACT MODIFICATION FOR SEMI-CRYSTALLINE THERMOPLASTICS

3.1   Introduction

Semi-crystalline thermoplastics are a major class of polymeric materials. The most common semi-crystalline polymers are polyolefins, polyamides, and polyesters which are used extensively in the transportation, manufacturing, industrial, and agricultural sectors.[100-102] These polymers contain crystalline regions and amorphous regions where crystalline regions are composed of ordered, lamellar structures, and amorphous regions are comprised of entangled polymer chains. Mechanical properties of semi-crystalline materials depend on overall crystallinity, lamellar thickness, and crystal phase.[10, 103] The orientation of crystal grains results in anisotropic mechanical properties.[104] In addition, semi-crystalline polymers provide better chemical resistance, lower coefficient of friction, and superior electrical properties than amorphous polymers.[105, 106] It results in better suitability of semi-crystalline polymers for certain applications, for example bearing, wear, and structural applications.

However, semi-crystalline materials demonstrate poor impact properties. Their yield stress scales with the percent crystallinity and lamellar thickness.[10] During a failure event, a competition arises between the creation of a new surface area and matrix yielding.[12] Materials with high yield stresses tend to undergo catastrophic failure before the matrix can yield.[107] As a result, semi-crystalline materials with high yield stresses are at risk of a brittle failure. This makes it necessary to investigate the impact modification of semi-crystalline thermoplastics.

During any fracture event, a triaxial state of stress is present in front of a crack tip. The magnitude of these stresses inversely scales with the distance from the crack tip. Thus, high stresses are present near the crack tip.[108] This stress state subjects the material for volume change where octahedral shear stresses in front of the crack tip are insignificant.[63] This makes it challenging for the material to dissipate energy *via* matrix yielding. Without any plastic deformation, materials fail catastrophically under high stresses.

Impact properties of polymers are often improved *via* soft particle toughening. It involves the incorporation of a second, soft, rubbery phase in the matrix. These rubbery domains act as a stress concentrator under the plane strain loading condition (triaxial state of stress) present in front of the crack tip. They cavitate and relieve hydrostatic stress. It allows the matrix to deform, yield and undergo plastic deformation.[20] Plastic deformation results in energy absorption and improves the impact properties.

Cavitation acts as a precursor for energy absorption. It depends on the domain size as well as modulus mismatch between the rubbery domains and the matrix, as indicated by Equation 1.3 (Chapter 1).[18] Domains that are too small are difficult to cavitate and domains that are too large act as defects. Optimum domain size results in the most significant improvement in the impact properties.[63] In addition to the domain size, many research groups studied the effect of rubber concentration, rubber modulus, and interparticle distance between the domains on fracture toughness.[109] Chapter 2 describes in detail that materials when engineered with optimum size, concentration, and inter-particle spacing for rubbery domains achieve the most significant toughness enhancement.

More recently, our (Lesser) group showed that the far-field stress (σ_m) required for the cavitation of rubbery domains depends on both domain size and shape.[88] Equation 3.1 describes the σ_m required for the cavitation of non-spherical ellipsoidal domains.

$$\text{Equation 3.1}: \sigma_m \sim K_m \left(\frac{\gamma}{K_R}\right)^{\frac{3}{4}} \frac{1^{\frac{3}{4}}}{a_c} \left(\frac{r}{a_c}\right)^{\frac{3\alpha}{4}}$$

where σ_m is the mean far-field (applied) stress; K_m and K_R are bulk modulus for the matrix and the rubber, respectively; γ is the surface energy of rubber particle; a_c is the semi-major axis for the ellipsoidal domain; α is the shape factor and for ellipsoidal domains, it is equivalent to their aspect ratio (a/b). α is evaluated either experimentally or numerically.

σ_m depends on the semi-major axis (a_c), the local radius of curvature (r), and shape factor (α). For spherical particles, values for the local radius of curvature (r) and semi-major axis (a_c) are equivalent with the particle radius (R_c). Upon substituting these values, Equation 3.1 reduces to Equation 1.3 (Chapter 1) which shows that cavitation stress for spherical particles inversely scales with the particle size and it is independent of the shape factor (shape factor α is 1 for spherical domains). Even for non-spherical domains, σ_m inversely scales with the domain size (a_c). It follows that domains must have optimum size to achieve improved impact properties. Further, σ_m decreases with the radius of curvature, as shown in Figure 3.1. Domains with a smaller radius of curvature (higher curvature) cavitate at lower stresses than spherical domains. α for ellipsoidal domains is their aspect ratio (a/b). Asymptotic analyses indicate that that the shape factor (α) is bounded between $2/3 \leq \alpha \leq 2$. Cavitation stress for a spherical particle is independent of the shape factor intensity since $a_c = r = R_c$. Moreover, Equation 3.1 shows that both size and shape are

important for cavitation. This means that the lower bound that exists from spherical modification does not exist for non-spherical geometries. Figure 3.1 shows the σ_m as a function of the shape factor (α). α for perfectly spherical domains is 1 and its magnitude increases as domains become more elongated or non-spherical. Comparison of the cavitation stress (σ_m) for domains with similar semi-major axis but different shape factor shows that domains with higher shape factor (α) cavitate at lower stresses and demonstrates that σ_m decreases with the shape factor.
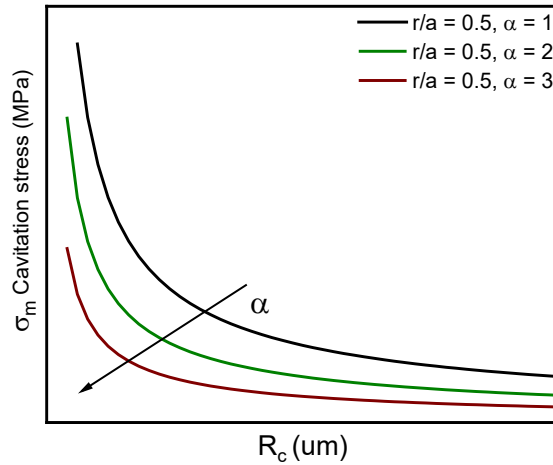
Figure 3.1 Cavitation stress as a function of particle size (R_c) and shape factor (α).

For a thin plate under uniaxial tension, Equation 3.2 describes local stress at the particle-matrix interface. Materials containing spherical domains when loaded in uniaxial tension create a stress concentration (σ_θ / σ_m) of 3 at the interface. For ellipsoidal domains, local stress depends on domain size (a_c) and local radius of curvature (r). As a result, stress concentration is higher than 3 for non-spherical, ellipsoidal domains and depends on the ratio a_c/r. The highest stress concentration is present at the tip of the major axis for ellipsoidal domains where the radius of curvature is the smallest.

Equation 3.2: $\sigma_\theta = \sigma_m \left(1 + 2\sqrt{\dfrac{a_c}{r}} \right)$

55

where σ_θ is the local stress; σ_m is the applied far-field stress; a_c is the semi-major axis for ellipsoidal domains; r is the local radius of curvature.

The stress concentration for spherical domains also depends on the state of stress. For example, stress concentration is 3 under uniaxial loading, 2 under biaxial loading, and 1.5 under triaxial loading (as discussed in detail in Chapter 1). On the other hand, subjecting a material with a penny-shaped crack (a large semi-major axis and a very small local radius of curvature at the edge) to a triaxial state of stress results in infinite stresses at the crack tip.[6] Consequently, the stress concentration for non-spherical or ellipsoidal domains under a triaxial state of stress is highly complex. Nevertheless, non-spherical domains exhibit higher stress concentration than spherical domains and it depends on the local radius of curvature and semi-major axis.

Even in the vicinity of heterogeneous domains, stresses are higher than the far-field applied stress which causes the surrounding matrix to yield. Moreover, when two or more domains with appropriate inter-particle spacing are present, the yield fronts initiated at these domains percolate and involve a large volume of the matrix in the yielding process. Such particle-particle interactions increase the energy absorption during a failure. Notably, non-spherical domains with higher stress concentrations demonstrate more localized and stronger particle-particle interactions. To understand this phenomenon further, our collaborators at BASF, Germany performed finite element modeling to map the von Mises stresses generated upon deformation of a rigid matrix containing voids where void shape and volume are systematically changed. Figure 3.2 shows an example of von Mises stresses in a deformed material containing void in the shape of 3-axial ellipsoidal domains. Herein, the highest stress concentration present at the tip of ellipsoidal domains results in

significant particle-particle interactions and achieves the highest von Mises stresses where the local stress fields overlap. Overall, non-spherical and small radius of curvature (high-curvature) domains with optimum particle size and inter-particle spacing are desired to obtain improved, next-generation impact modification.
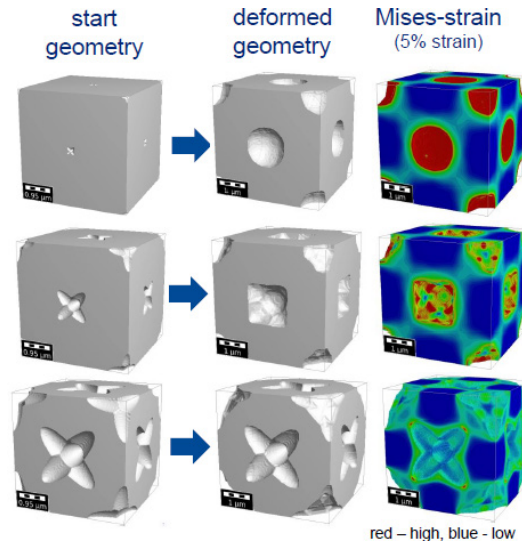
Figure 3.2 von Mises stresses for a material containing void in the shape of 3-axial ellipsoids.

Previous work in the Lesser group showed that non-spherical rubbery domains are more effective in impact modification of glassy epoxy thermoset than conventional spherical domains.[88] However, non-spherical impact modification for semi-crystalline thermoplastics is not yet studied. This chapter focuses on next-generation, non-spherical impact modification for semi-crystalline thermoplastics. Herein, we demonstrate novel strategies to obtain non-spherical rubbery domains and investigate their effect on impact properties. In this work, we consider two different semi-crystalline polymers, polypropylene and polyoxymethylene.

Polypropylene is a semi-crystalline commodity thermoplastic used in a variety of industrial sectors. Impact modification of polypropylene presents a unique challenge. Polypropylene has a glass transition temperature (T_g) of approximately 15 °C. It is in a rubbery regime at room temperature and exhibits an inherently ductile failure.[110, 111] However, it is in a glassy regime at subzero temperatures and it further increases the difficulty to achieve improved impact properties. The yield stress of a material depends on temperature and strain rate and it increases dramatically with a decrease in test temperature.[112] Materials with higher yield stresses are often more brittle, as discussed previously in Chapter 1. As a result, polypropylene shows poor impact properties at subzero temperatures.[113, 114] It cannot be used in applications where operating conditions are below the room temperature, for example, the automotive industry. In this chapter, we focus on the impact properties of polypropylene under subzero temperatures and high strain rates.

Soft particle toughening has been extensively studied for polypropylene. It is achieved by engineering a formulation in such a way that soft rubbery particles are formed at an optimum size and interparticle distance during the manufacturing process. It is necessary to identify additives that are miscible in the polypropylene melt. Upon melt cooling, thermally induced phase separation (TIPS) must occur to generate rubbery domains of appropriate morphology to provide effective toughening. Elastomers and block copolymers are the most common additives for the soft particle toughening of polypropylene.[13, 23, 115] Some of the most common impact modifiers are styrene-ethylene/butylene-styrene (SEBS), Polyolefinic elastomer (POE), Ethylene-propylene diene monomer (EPDM), and Ethylene-propylene rubber (EPR). Conventional soft particle

toughening only investigates the effect of particle size, concentration, and inter-particle spacing. The effect of particle shape remains an open question.

Various routes are discussed in the literature that generate non-spherical domains. Recently, Bates' group synthesized precise block copolymers that generate unusual and non-spherical phase-separated domains in epoxy.[116] Surface functionalization or compatibilization of an additive often alters its morphology.[117] Wooley's group obtained highly complex, multi-geometry nanoparticles blending block copolymers in a solution.[75] Epoxy resin mixed with two block copolymers forms non-spherical domains *via* reaction-induced phase separation (RIPS) upon complete curing.[88] Blending two or more impact modifiers have obtained synergistic toughness improvements and have proven to be a cost-effective approach.[43, 118] Taking motivation from these recent reports, we investigate the strategy of blending two block copolymers with polypropylene melt to obtain non-spherical phase-separated domains.

Block copolymers that phase separate in a polymer matrix generate micellar domains. The morphology of these domains depends on thermodynamic and kinetic factors. Thermodynamic factors include the molecular weight, chemical structure of each block and its interaction parameter (χ) with the matrix, and relative weight fraction of blocks. For TIPS, kinetic factors include the rate of cooling, mixing speed, and mixing temperature. Polymer melt containing two block copolymers is a complex system. There exists an enthalpic driving force for each block copolymer to phase separate from the matrix and also from the other block copolymer. This process can get trapped during a rapid cooling cycle that occurs in an injection molding process. This makes blending two block copolymers a viable strategy to obtain trapped, unusual domain shapes.

59

In semi-crystalline materials, amorphous chains are present in the inter-spherulitic region. Amorphous elastomers and block copolymers localize in this region. A nucleating agent alters the spherulite size and percent crystallinity. This can further frustrate the morphology of phase-separated domains present in the inter-spherulitic region. Talc is a heterogenous nucleating agent and a reinforcement for polypropylene. Incorporating talc provides opportunities to alter the domain shapes. Additionally, combining talc with rubbery additives can achieve balanced toughness and stiffness properties.[119, 120]

Herein, polypropylene formulations are engineered using block copolymeric impact modifiers POE and SEBS, and talc. In this chapter, a systematic investigation is conducted to illustrate the effect of blending block copolymer with or without talc on the morphology, thermal, and impact properties of polypropylene. Impact properties are studied using quasi-static room temperature fracture toughness tests and high strain rate, low-temperature instrumented impact tests. The thermal properties are characterized by differential scanning calorimetry (DSC) and dynamic mechanical analysis (DMA). The morphological investigation and fractographic studies are performed using scanning electron microscopy (SEM). In addition, the failure mechanisms that occur under extreme loading conditions (high strain rates, low temperatures) are discussed.

3.2   Experimental

3.2.1   Materials

Polyoxymethylene pellets were provided by BASF. Styrene-ethylene/butylene-styrene block copolymer (G-1645) was provided by Kraton polymers. Maleic anhydride functionalized SEBS (SEBS-*g*-MA), styrene-isoprene-styrene (SIS), dicumyl peroxide, and antioxidant Irganox 1010 were purchased from Sigma Aldrich.

3.2.2   Polypropylene sample preparation

Impact modified polypropylene samples for mechanical testing were provided by Kraton polymers. These formulations were prepared using polypropylene copolymer, polyolefin-based elastomer (POE), styrene-ethylene/butadiene-styrene block copolymer (SEBS), and talc. First, these formulations were compounded using a twin-screw extruder, passed through a strand die, and pelletized. During compounding, 0.4 wt.% of antioxidants were used to prevent thermal degradation. Polypropylene formulations were further injection molded with a melt temperature of 220 °C and a mold temperature of 40 °C to obtain samples for single edge notch bend test (SENB) and instrumented impact testing. Table 3.1 shows the compositions for polypropylene formulations.

Formulation	PP (wt.%)	POE (wt.%)	SEBS (wt.%)	Talc (wt.%)
POE	75	25	0	
POE+SEBS	75	22	3	
SEBS	75	0	25	
POE+Talc	60	25	0	15
POE+SEBS+Talc	60	22	3	15
SEBS+Talc	60	0	25	15

Table 3.1 Composition for polypropylene formulations

3.2.3 Polyoxymethylene sample preparation

Polyoxymethylene (POM) formulations comprising of polyoxymethylene and an additive were prepared using batch mixing. Polyoxymethylene pellets and additives were dried in a vacuum oven at 80 ℃ for 4 hours before the batch mixing. Batch mixing was performed on Brabender's Intelli-Torque Plasti-Coder. In a standard procedure, an appropriate amount of polyoxymethylene pellets, additive, and Irganox 1010 antioxidant (0.5 wt.%) were added to the batch mixer. Batch mixing was performed for 20 mins at 180 ℃ with 70 rpm. The batch mixed material is then compression molded at 200 ℃ for 10 mins under 0.125 MN to afford a plaque which was utilized for the thermal, mechanical, and morphological characterization of the formulations.

3.2.3.1 Preparation of polyoxymethylene-elastomer adduct

Polyoxymethylene-elastomeric adducts were prepared to evaluate their performance as an impact modifier or as a compatibilizer. These adducts were prepared using SEBS, SEBS-*g*-MA, and SIS. Adducts were prepared using the batch mixer in the absence of antioxidants or stabilizers. In a standard procedure, an appropriate amount of dried polyoxymethylene pellets and elastomeric pellets were added to the batch mixer and mixed at 180 ℃ for 10 mins, followed by the addition of dicumyl peroxide (DCP) (0.25 wt.%), and mixing continued for further 10 mins. The prepared adducts were used as an additive with polyoxymethylene pellets for further characterization. These adducts are denoted with "elastomer_Ax", where elastomer indicates the name of the elastomer in a given adduct and x indicates the weight fraction of the elastomer in that adduct. For

example, SEBS_A80 denotes adduct prepared using 80 wt.% of SEBS and 20 wt.% of polyoxymethylene.

3.2.4 Thermal analysis

Differential scanning calorimetry was performed using TA instruments Q200 to measure the crystallization temperature, melting temperature, and percent crystallinity for semi-crystalline polypropylene and polyoxymethylene. Samples were run in the temperature range of -30 °C to 210 °C at a heating rate of 10 °C min^{-1} during a consecutive heat-cool-heat cycle. Crystallization temperature (T_c) was determined from 1st cooling cycle. Melting temperature (T_m) and percent crystallinity were evaluated from 2nd heating cycle. Percent crystallinity values are normalized with a fraction of the matrix (polypropylene or polyoxymethylene).

Dynamic mechanical analysis (DMA) was performed using TA instruments Q800 in the temperature range of -50 °C to 50 °C with a heating rate of 3 K min^{-1} and a frequency of 1 Hz under constant strain mode to determine the storage modulus and tan delta as a function of temperature.

Thermogravimetric analysis (TGA) was performed using TA instruments Q50. Samples were heated from room temperature to 700 °C using a platinum pan in the nitrogen atmosphere and at a heating rate of 10 K min^{-1} to estimate the concentration of talc present in the formulations.

3.2.5 Fracture toughness of polypropylene formulations

Fracture toughness measurements were conducted on polypropylene formulations using Single Edge Notch Bend (SENB) test, following ASTM D5045. Injection-molded samples with dimensions of 80 x 10 x 4 mm were used for SENB measurements. Samples were notched using a diamond wafering blade. Samples were dipped in liquid nitrogen for few minutes, followed by inserting a razor blade in the notch and tapping it with a wrench to create a sharp pre-crack. Room temperature SENB testing was conducted using Instron 5800 equipped with a 1 kN load cell and SENB assembly with a span length of 44 mm at a constant crosshead speed of 50 mm/min. Fracture toughness was determined using Equation 3.3.

Equation 3.3: $K_q = \frac{P_c f(x)}{BW^{1/2}}$

where P_c is the critical load, B is the specimen thickness, W is the width of the specimen, K_q is the fracture toughness in MPam$^{1/2}$, and f(x) is the geometric factor given by dimensionless power function in terms of x (where x = a/W, a ratio of pre-crack length to the specimen width), as shown in Equation 3.4.

Equation 3.4: $f(x) = 6x^{1/2} \frac{[1.99 - x(1-x)(2.15 - 3.93x + 2.7x^2]}{(1+2x)(1-x)^{3/2}}$

The non-linear fracture energy release rate (J_q) for polypropylene formulations was determined using Equation 3.5.

Equation 3.5: $J_q = \frac{K_q^2}{E} + \frac{\eta * A}{B * (W - a)}$

where K_q is the fracture toughness determined from single edge notch bend test, E is Young's modulus, B is the thickness of the sample, W is the width of the specimen, a is

the pre-crack length, and A is the area under the linear region of the load versus deflection curve. The fracture energy release rate reported is an average of at least 3 samples.

3.2.6 Instrumented impact testing on polypropylene formulations

Instrumented impact testing was conducted using Dynatup 8250 to determine the impact energy absorption for polypropylene formulations at -15 °C and -30 °C. The drop weight test was performed using a hemispherical tup with 12.7 mm diameter and a hammer mass of 5.7 Kg (12.5 lbs). Square samples with 10 cm sides and 2 mm thickness were secured using a pneumatic valve with a diameter of 40 mm and the tup was released from 1 m height above the sample, generating an impact velocity of 4.42 m/sec. The load versus displacement data recorded during the event of an impact was utilized to determine the total energy absorption. Samples were conditioned for 15 minutes at the test temperature using the environmental chamber prior to the test.

3.2.7 Scanning electron microscopy

The morphology of the phase-separated domains was determined using scanning electron microscope Magellan 400 equipped with a field emission gun. Samples for SEM were prepared by cryofracturing, briefly, samples were cooled using liquid nitrogen and then fractured. The fracture surfaces were then sputter-coated with a thin layer of gold before imaging. In the case of polypropylene formulations, samples for scanning electron microscopy were prepared by cryofracturing, followed by etching with xylene for 30 minutes at room temperature and vacuum drying. Morphology of the phase-separated

domains was further analyzed using Image J to estimate the average particle size and the shape factor.

3.2.8   Fractographic analysis of polypropylene formulations

Samples tested using instrumented impact testing were further utilized for failure analysis. The process zone of these samples was isolated and etched using an etching solution comprising potassium permanganate, concentrated sulphuric acid, and phosphoric acid.[121, 122] Etching solution forms magnesium heptoxide, a potent agent, that preferentially degrades the amorphous regions in polymeric materials. Sample surfaces were etched for 24 hours at room temperature, followed by washing with DI water for 3 times and vacuum drying. These samples were sputter-coated with a thin layer of gold before SEM imaging.

3.2.9   Tensile testing for polyoxymethylene formulations

Mechanical properties of the polyoxymethylene formulations were determined using an Instron 5800. Dogbone-shaped samples with an approximate thickness of 2 mm were punched from a compression molded plaque and tested with a uniaxial tension method at a crosshead speed of 10 mm/min. Data recorded during the tensile testing was used to determine the elastic modulus from the linear low strain regime (strain range – 0 to 0.05), yield stress, and the rupture energy density from the area under the stress-strain curve.

3.3   Results and Discussion

3.3.1   Thermal properties of impact modified polypropylene formulations

Engineered polypropylene formulations were characterized for their thermal properties using DSC. These formulations show a melting temperature of ~165 °C and percent crystallinity between 40% to 46%, as shown in Table 3.2. Notably, the thermal characteristics are independent of the identity of the impact modifier. Impact properties of polypropylene depend on overall crystallinity.[119, 123, 124] These formulations are prepared with the exact same processing parameters, such as temperature profile and cooling rate. It results in comparable crystallinity. This allows us to investigate the role of POE and SEBS on impact properties.

Additives	T_m (°C)	T_c (°C)	Overall crystallinity (%)	Modulus (MPa)
POE	163	119	46.1	725
POE+SEBS	163	121	42.4	600
SEBS	164	116	44.4	550
POE+Talc	165	125	41.4	1030
POE+SEBS+Talc	166	124	39.4	880
SEBS+Talc	165	127	43.1	830

Table 3.2 Thermal and mechanical properties of polypropylene formulations.

Incorporating talc increases the crystallization temperature. Talc is a heterogenous nucleating agent for polypropylene. It lowers the energy barrier for crystallization. This allows crystal nucleation to occur at higher temperatures.[124, 125] However, talc does not affect the melting temperatures and percent crystallinities. These formulations contain a high fraction of impact modifiers (25 wt.%). These impact modifiers might affect the nucleation and growth of polypropylene spherulites. This results in similar crystallinities even in the presence of a nucleating agent.

The thermal stability of polypropylene formulations was investigated using TGA, as shown in Figure 3.3. Formulations containing only impact modifiers exhibit the onset of degradation at 300 °C. Both the impact modifiers are organic hydrocarbons. As a result, they show similar degradation characteristics and achieve complete degradation. The thermal stability of these formulations improves with the incorporation of talc. Talc-containing formulations exhibit a higher onset of thermal degradation (450 °C) and a char residue of 15 wt.% at 700 °C. Char residue confirms the weight fraction (15%) of inorganic talc present.
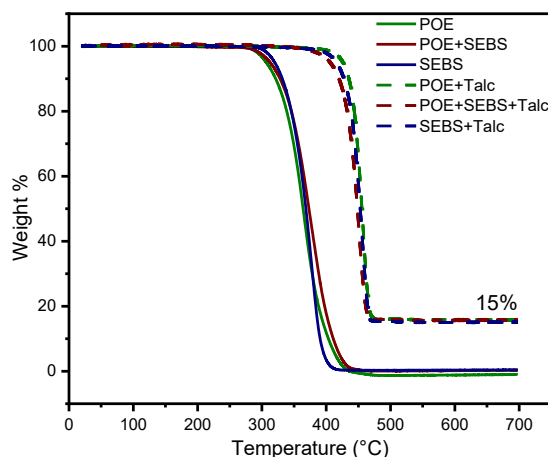
Figure 3.3 Thermal degradation and char residue for polypropylene formulations.

Matrix stiffness is an important parameter in formulating polymeric materials and therefore, it was evaluated using DMA. Storage modulus values at 25 °C are ascribed as the modulus for the corresponding formulation and are tabulated in Table 3.2. Modulus values for impact modified polypropylene are lower than the reported modulus for polypropylene.[126] These additives improve the impact properties at the expense of matrix rigidity. Further, SEBS results in a more significant reduction in stiffness than POE. Formulations containing both SEBS and POE show modulus values in between only SEBS- and only POE-containing formulations. The modulus of a composite system scales

with the weight fraction and modulus of each phase.[103] This suggests that amorphous SEBS has a lower modulus in comparison with the semi-crystalline POE. Incorporating talc enhances the modulus for these formulations. Talc acts as a rigid particulate reinforcement. This shows that talc when used in combination with impact modifiers can achieve balanced toughness and stiffness properties.

3.3.2   Morphology for impact modified polypropylene formulations

Polypropylene formulations are engineered with impact modifiers POE and SEBS. These additives are such that they remain miscible in the melt but phase-separate upon cooling. Morphology of these phase-separated domains is investigated using SEM, as shown in Figure 3.4. These domains are etched using a solvent before imaging and therefore, appear as darker voids. POE phase-separates to generate domains in the range of 200-300 nm. A blend of POE and SEBS results in similar, few hundred-nanometer domains. Interestingly, SEBS exhibits the bimodal distribution of domain sizes. It forms larger, micron-size domains (~1 um) and smaller, hundreds of nanometer size domains (~200 nm). Polypropylene formulations exhibit a variety of domain shapes and some of them are non-spherical. POE generates spherical, prolate ellipsoidal, and some irregular domains. Whereas SEBS forms spherical and ellipsoidal domains and some highly elongated rod-like domains. A combination of POE and SEBS results in shapes similar to only POE domains.
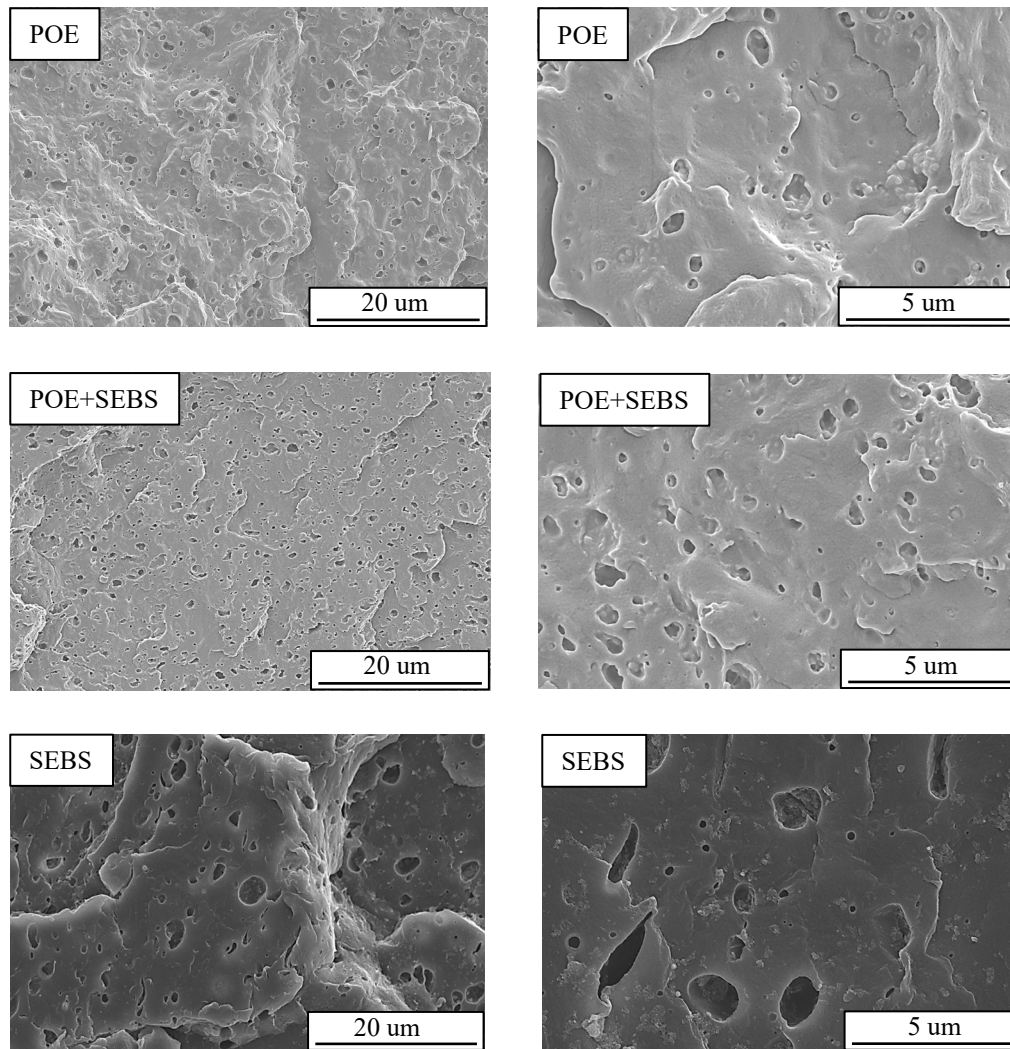
Figure 3.4 Morphology for polypropylene formulations containing POE, a combination of POE and SEBS, and SEBS, respectively.

The size and shape of these domains depend on thermodynamic and kinetic factors.[127-129] POE and SEBS have inherent differences in their molecular architecture, compatibility with polypropylene, and viscosity. This results in variation in domain sizes and shapes. SEBS phase-separates to generate smaller 200 nm domains. During the TIPS, SEBS chains diffuse from smaller domains to larger domains to achieve thermodynamic equilibrium. This process, termed Ostwald ripening, gives rise to a two-phase system and bimodal size distribution.[87] Polypropylene formulation with a blend of impact modifiers contains POE as a major fraction (22%) and SEBS as a minor fraction (3%). As a result,

domain sizes are akin to only POE domains. Although the precise morphology is not investigated during this work, the formation of a core-shell morphology is very likely. In this case, an impact modifier with higher compatibility with the matrix forms a shell.
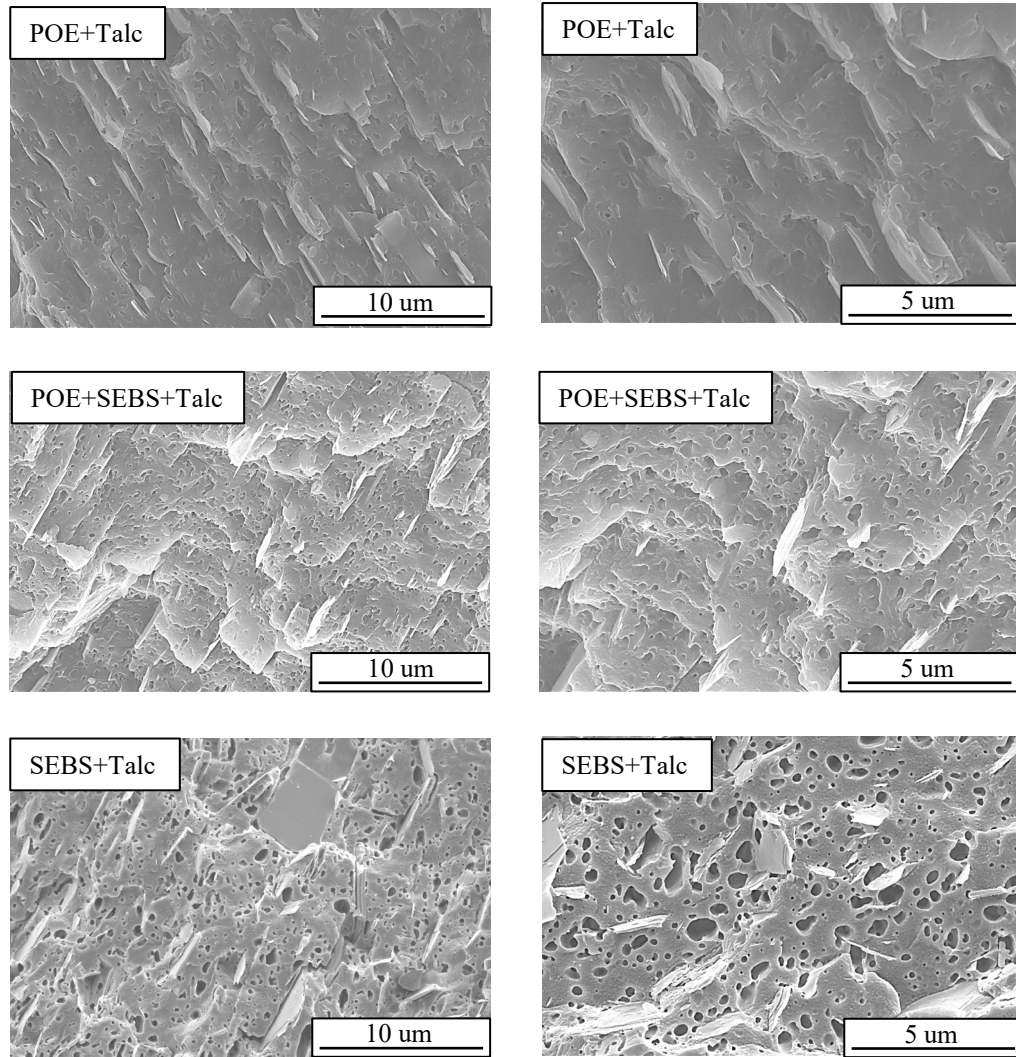
Figure 3.5 Morphology for talc-containing polypropylene formulations comprising of POE, a combination of POE and SEBS, and SEBS, respectively.

Figure 3.5 shows the morphology of talc-containing impact modified polypropylene formulations. These images show a uniform dispersion of 2 to 4 um large, white color talc flakes. Incorporating talc reduces the size of domains. Size of domains, when only POE or both POE and SEBS are present, decrease from 300 nm to 150 nm. Whereas SEBS shows the most significant reduction in domain sizes where sizes decrease

from 1 um to 150 nm. Even with smaller domain sizes, these formulations still exhibit non-spherical, ellipsoidal domains. Incorporating talc alters the thermodynamic and kinetic factors associated with the TIPS. Talc increases the process viscosity. This results in higher shear stresses during the processing and a lower diffusion rate for impact modifiers. Further, impact modifier chains localize in the inter-spherulitic region. Talc also acts as a nucleating agent and thereby, reduces the size of spherulites and increases the crystallization temperature. This effect is similar to rapid quenching. As a result, the surrounding matrix cools rapidly when the phase-separation occurs. Reduction in diffusion rate and diffusion time limits coarsening of domains and achieves smaller domain sizes when talc is present.

Engineered polypropylene formulations exhibit non-spherical and irregular domains. Most of these domains are spherical or ellipsoidal. These domains produce a circular or elliptical shape on a 2-dimensional cross-section and are analyzed by treating them as an ellipse. Image J was used to measure the perimeter and area of these domains. Equation 3.6 and Equation 3.7 describe perimeter and area as a function of semi-major axis "a" and semi-minor axis "b" of an ellipse. These equations were solved to determine the semi-major axis "a", semi-minor axis "b", and aspect ratio (shape factor) "a/b", as shown in Table 3.3. Most importantly, this analysis allows us to determine the aspect ratio (shape factor α) of these domains. The aspect ratio quantifies the non-sphericity associated with domains.

Equation 3.6: $\text{P} \cong 2\pi\sqrt{\dfrac{a^2+b^2}{2}}$

Equation 3.7: $\text{A} = \pi ab$

where P is the perimeter and A is the area for an ellipse.

Formulation	"a" (um)	"b" (um)	"a/b"
POE	0.41 ± 0.2	0.23 ± 0.1	1.7
POE+SEBS	0.27 ± 0.1	0.14 ± 0.1	1.9
SEBS	1.31 ± 0.6	0.63 ± 0.3	2.1
POE+Talc	0.20 ± 0.1	0.09 ± 0.1	2.2
POE+SEBS+Talc	0.19 ± 0.1	0.09 ± 0.1	2.2
SEBS+Talc	0.17 ± 0.1	0.08 ± 0.1	2

Table 3.3 Average semi-major axis (a), semi-minor axis (b), and aspect ratio (a/b) for phase-separated domains of polypropylene formulations analyzed as ellipses.

This analysis shows that only POE and a blend of POE and SEBS generate smaller domains with an average semi-major axis of 0.4 um and 0.3 um, respectively. These domains exhibit a shape factor of 1.7 and 1.9, respectively. Whereas SEBS forms larger domains with a semi-major axis of 1.3 um and shape factor of 2.1. SEBS with its inherent molecular architecture obtains the most non-spherical domains. SEBS when blended with POE, even at small fractions, achieves more non-spherical domains than with only POE. By blending two block copolymers, domains with size and shape different than the individual block copolymer can be obtained. Incorporating talc significantly reduces the particle size and obtains an average semi-major axis of approximately 0.2 um. Adding talc decreases particle size as well as shape factor for the SEBS domains. Shape factor and particle size analysis provide opportunities to understand the correlation between the morphology and impact properties of these polypropylene formulations.

3.3.3   Mechanical properties of polypropylene formulations

Impact properties of polypropylene formulations were investigated using fracture toughness test and instrumented impact test. Polypropylene is an inherently ductile material at room temperature.[110, 111] Consequently, the room temperature fracture toughness test shows non-linear load versus extension response for engineered polypropylene

formulations (Appendix Figure A3.1). It also forms a stress-whitened process zone in front of the crack tip. This zone results from the plastic deformation processes that occur during the failure. In these formulations, energy absorption occurs *via* the creation of a new surface area and plastic deformation. Therefore, energy dissipation evaluation must consider elastic as well as plastic contributions. Figure 3.6 shows the non-linear fracture energy release rate (J_q). Polypropylene modified with SEBS demonstrates the highest J_q. Interestingly, a blend of POE and SEBS results in lower J_q than only POE and only SEBS.
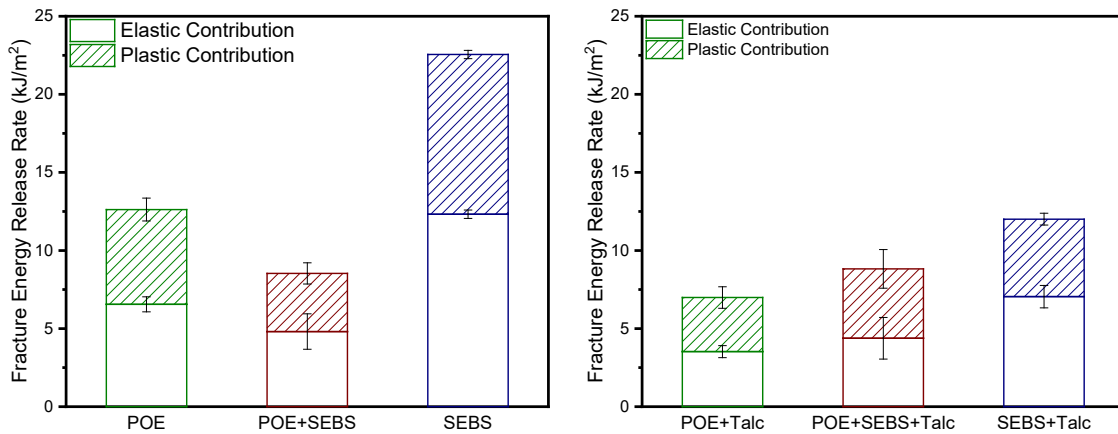
Figure 3.6 Fracture energy release rate for polypropylene formulations determined from quasi-static SENB testing at room temperature.

Notably, J_q scales with the average particle size (semi-major axis "a" of ellipsoidal domains) for impact modified polypropylene. Fracture toughness properties for polymers often scale with particle size. Larger domains cavitate at lower stresses, as discussed in section 3.1. It allows larger domains to effectively cavitate and activate energy absorption processes, such as yielding, crazing, or shear band formation. SEBS generates larger, higher aspect ratio domains than other formulations. These domains achieve higher stress concentration and cavitate at lower stresses. Higher stress concentration improves particle-particle interactions. This results in significantly higher plastic deformation and thereby, improved impact properties for polypropylene modified with SEBS.

74

Incorporating talc reduces the fracture toughness for only SEBS- and only POE-containing formulations. On the other hand, when a blend of POE and SEBS is present, the addition of talc achieves comparable fracture toughness. There are three main reasons that result in the reduction of fracture toughness upon incorporating talc. First, the addition of talc significantly reduces the size of domains for impact modified polypropylene. These smaller domains are difficult to cavitate and thereby, less effective in toughening. Second, the incorporation of fillers creates a weak interfacial region with the matrix. These fillers also resist against plastic deformation. Third, talc produces a large number of nucleation sites and smaller spherulites. This large inter-spherulitic boundary further weakens the material.[130-132] Weak interface leads to poor impact properties. As a result, the incorporation of talc results in a reduction in J_q. Fracture toughness tests show that SEBS is a better toughening agent for polypropylene compared with POE when tested at room temperature. These room-temperature impact properties show a strong dependence on particle size.

Impact properties of engineered polypropylene formulations under extreme loading conditions were evaluated using the instrumented impact testing. Testing was conducted at -15 °C and -30 °C and at a high strain rate when a material is under a biaxial state of stress. Polypropylene is in a glassy regime at test temperatures. Further, the yield stress of polymeric materials increases with the strain rate and decreases with the temperature.[96, 133] This contributes to a brittle failure for polypropylene. As a result, improving the low-temperature impact properties of polypropylene is challenging.

Figure 3.7 shows the total absorbed energy normalized with the sample thickness. Impact modifier SEBS achieves the highest energy absorption even under extreme loading

conditions. This formulation exhibits a ductile failure. Polypropylene modified with POE and with a blend of POE and SEBS shows comparable energy absorption and brittle failure. Impact properties at subzero temperature also scale with the particle size. SEBS exhibits larger domain sizes than POE. In addition, SEBS has a much lower modulus than POE at test temperatures (Appendix Figure A3.2). For effective soft particle toughening, the impact modifier (rubber) should have an order of magnitude lower modulus than the matrix. This is a necessary and often a sufficient requirement. Interestingly, the impact properties of nylon gradually increase with decreasing modulus of the impact modifier.[134] This shows that impact properties depend on the modulus of the rubbery phase. As a result, SEBS leads to superior energy absorption for polypropylene in comparison with POE.
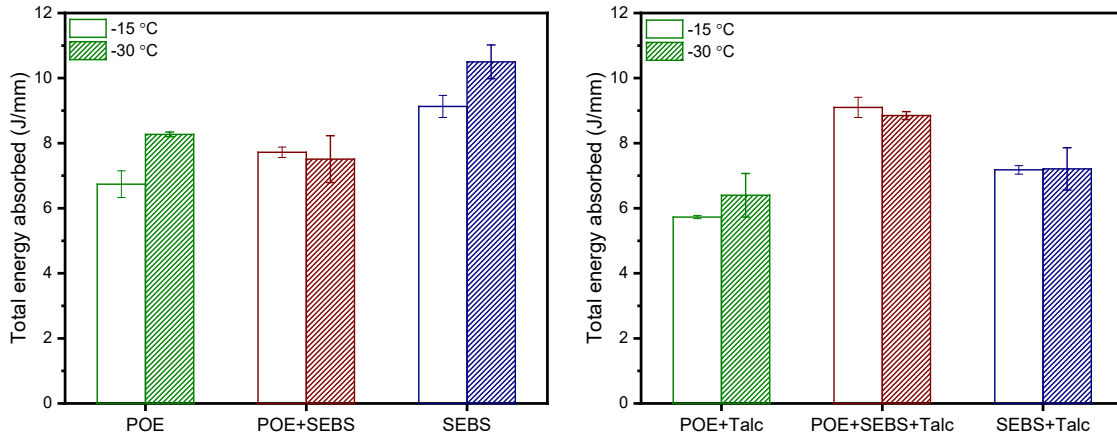
Figure 3.7 Total energy absorbed during instrumented impact testing under extreme loading conditions for polypropylene formulations.

Incorporating talc decreases the energy absorption under extreme loading conditions when polypropylene is modified with only SEBS or only POE. These formulations exhibit a brittle failure. Talc acts as a stress concentrator and contributes to the formation large weak interface. Interestingly, talc-containing polypropylene formulation modified with a blend of POE and SEBS demonstrates higher energy absorption compared with only SEBS and only POE.

Talc-containing formulations have similar domain sizes and shapes. SEBS with large domain sizes and lower modulus shows higher energy absorption than POE even when talc is present. Polypropylene modified with SEBS, POE, and talc is a complex multicomponent system. Morphology of domains, stiffness of each phase, failure mechanisms that occur dictates the energy absorption. Nonetheless, it appears that talc-containing polypropylene when modified with a blend of POE and SEBS shows synergistically higher energy absorption than when modified with only POE or only SEBS.

3.3.4 Fractographic analysis for polypropylene formulations

The fractographic analysis was performed to understand the failure mechanisms that occur under extreme loading conditions. Instrumented impact testing creates a stress whitened process zone that surrounds the puncture location. This is a result of plastic deformation that occurs during the material failure. Isolated and etched process zone were imaged using SEM, as shown in Figure 3.8. Etching conditions are optimized to selectively degrades the rubbery, amorphous regions. These micrographs show polypropylene spherulitic crystal structure, resulting from the etching of inter-spherulitic amorphous regions. Process zone for polypropylene modified with POE shows agglomerated white color crystalline POE domains. Any indications of craze nucleation or particle cavitation are absent. This suggests plastic energy absorption primarily occurs *via* matrix yielding and shear deformation. Process zone for polypropylene modified with a blend of POE and SEBS demonstrates fibrillated crazes. These crazes are concentrated in the regions where agglomerated POE domains exist. In this case, nucleation and growth of crazes are also a mode of failure.
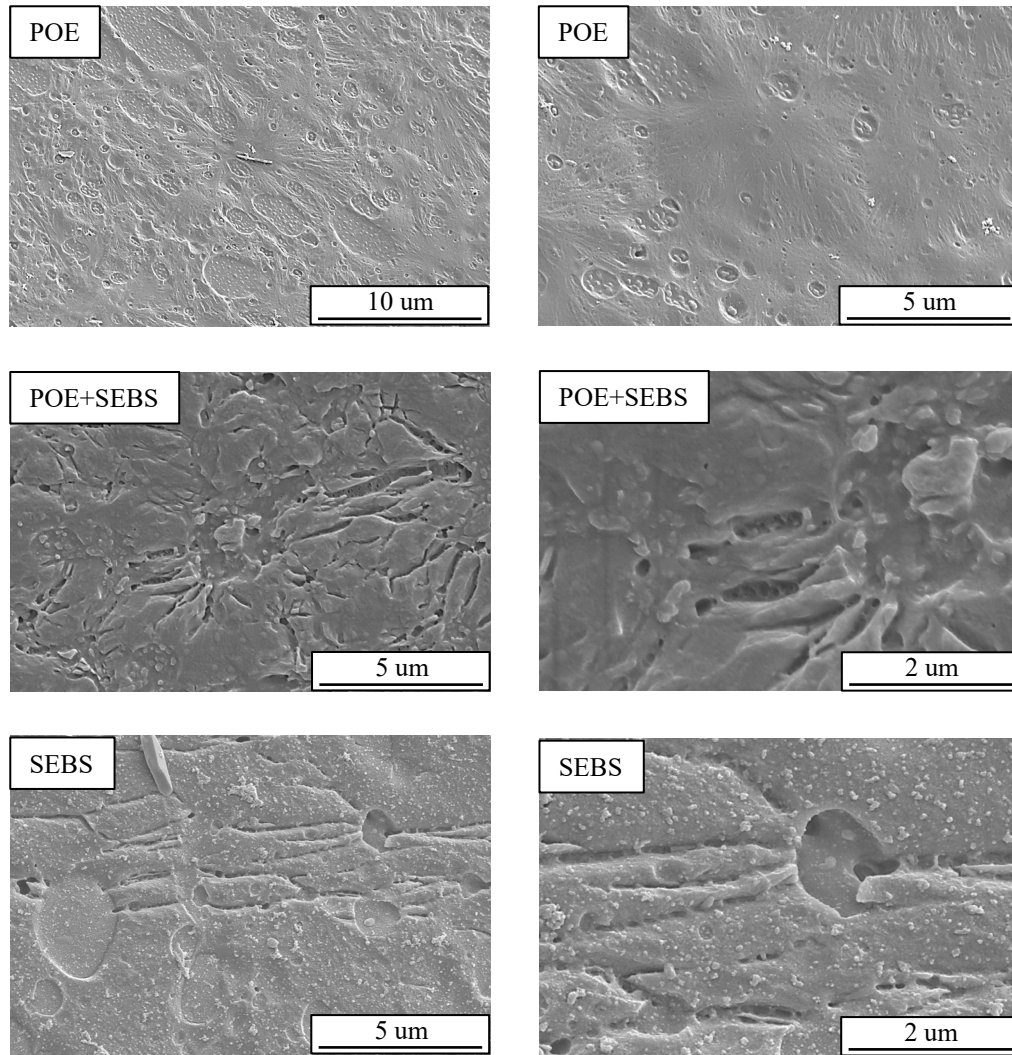
Figure 3.8 Etched process zone for impact tested polypropylene formulations comprising of POE, a combination of POE and SEBS, and SEBS, respectively.

Process zone for polypropylene modified with SEBS shows ellipsoidal domains. SEBS is an amorphous block copolymer and gets completely etched. Process zone exhibits similar, broad size distribution that was observed on the cryofractured surface. This process zone also shows the formation of fibrillated crazes. These crazes appear to nucleate at the surface of SEBS domains. Notably, these crazes are much larger than crazes that occur for a blend of POE and SEBS. The region around the domains where stresses are higher scales with the domain size.[32] Larger domains have a more pronounced region around them where stresses are high and it allows the material to be drawn in the growing craze. These load-

bearing crazes are stabilized by the larger SEBS domains that allow additional matrix material to be drawn in the crazes.[32, 33] In some cases, crazes are bridging or connecting two neighboring domains. Higher stress concentration leads to strong particle-particle interactions and results in inter-connected craze formation. Inter-connected craze formation results in superior energy absorption for polypropylene modified with SEBS.

Figure 3.9 shows the etched process zone for talc-containing impact modified polypropylene formulations. These micrographs show micron size, dispersed talc particles. POE domains exhibit better dispersion when talc is present. Talc increases the melt viscosity and thereby, results in a reduction in the rate of diffusion. This minimizes the agglomeration of POE domains. These formulations show the formation of isolated, smaller crazes. Talc and phase-separated domains provide sites with higher stress concentration where craze nucleation occurs. This leads to the formation of multiple smaller crazes. However, larger domains (1 to 2 um) for craze stabilization are absent. As a result, the material fails before these crazes can grow and draw additional matrix material. These results suggest that, for engineered polypropylene formulations, cavitation of the rubbery domains is not the mechanism that activates the energy absorption, but craze nucleation and formation of stabilized crazes leads to superior energy absorption.

The effect of particle size and shape on the impact properties for polypropylene formulations is evaluated. Figure 3.10 shows room temperature fracture energy release rate (J_q) and subzero temperature energy absorption as a function of semi-major axis (a) and cavitation stress. Particle size and shape affects the cavitation stress (σ_m) and thereby, the efficiency of domains to cavitate and initiate the plastic deformation. σ_m is evaluated using Equation 3.1 with the measured values for semi-major axis (a), semi-minor axis (b), and

shape factor (a/b). Further, values for K_m, K_R, and γ is assumed as 1 to *only* consider the contributions of particle size and shape towards cavitation stress. Cavitation stress decreases with an increase in particle size or shape factor.
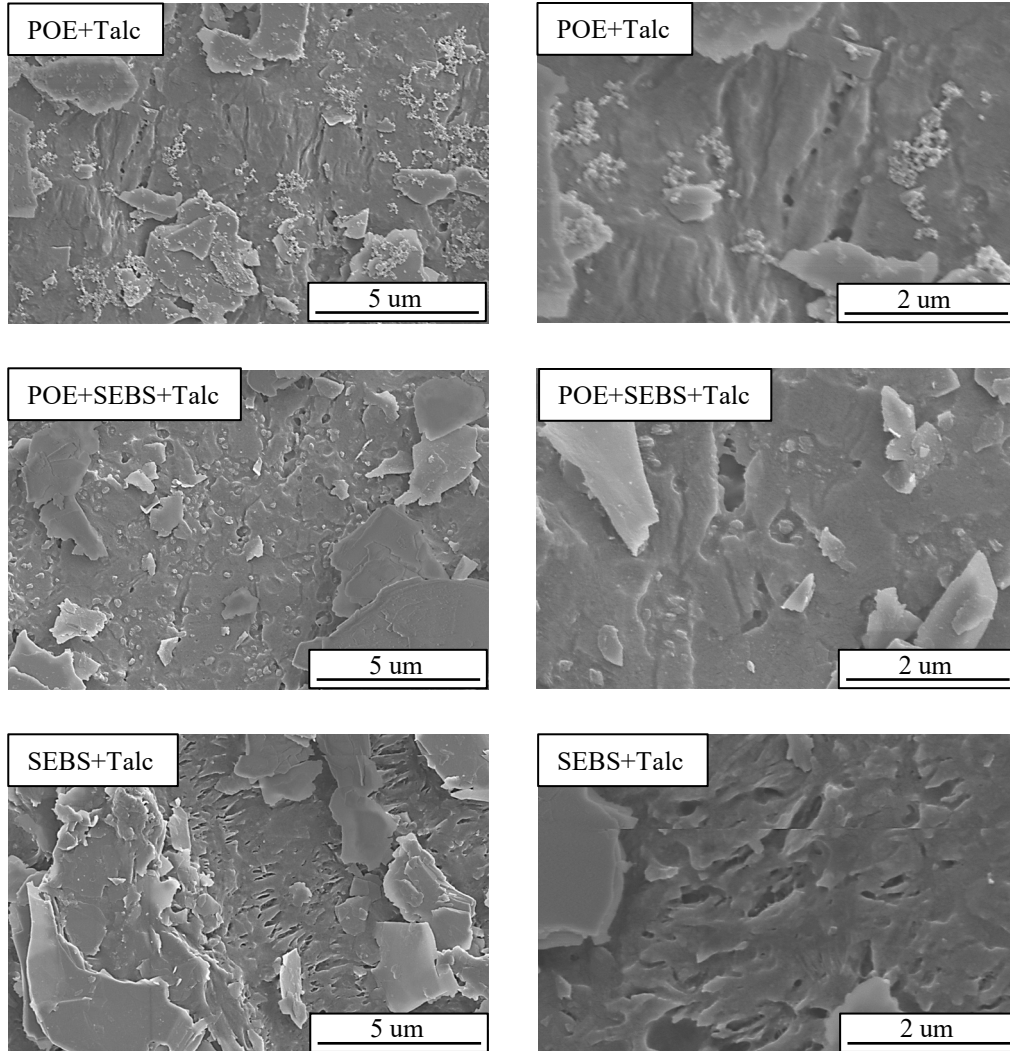
Figure 3.9 Etched process zone for impact tested, talc-containing polypropylene formulations comprising of POE, a combination of POE and SEBS, and SEBS, respectively.

Room temperature fracture energy release rate (J_q) for polypropylene formulations show a strong dependence on particle size. Although room temperature failure processes are not investigated here, cavitation of domains and consequent matrix yielding are likely failure mechanisms. σ_m inversely scales with the particle size and also, depends on the

80

aspect ratio of ellipsoidal domains. As a result, SEBS with the largest particle size and the lowest cavitation stress exhibit superior impact properties. Other formulations demonstrate compare particle size and shape factor, and thereby, achieve similar cavitation stress. Consequently, room temperature impact performance shows no clear dependence on particle shape. Even the impact performance under extreme loading conditions depends on the particle size with larger SEBS domains achieving the most significant energy absorption. Polypropylene formulations at subzero temperatures absorb energy *via* craze nucleation and growth. This craze formation strongly depends on the particle size. Engineered polypropylene formulations exhibit a narrow range of shape factors from 1.7 to 2.2. It is necessary to achieve particles with a similar size and a broad range of shape factors to assess the effect of particle shape on impact properties. Further, this analysis assumes similar mechanical properties (K_R and γ) for POE and SEBS rubbery phase which is not the case. As a result, the effect of cavitation stress and, in turn, particle shape remains unclear.

The blending of block copolymer results in non-spherical, ellipsoidal domains. However, the shape of these domains is comparable with domains obtained using each of the block copolymers individually. Additionally, the effect of particle shape on impact properties of polypropylene, studied here, is difficult to decipher. Future work will focus on a systematic investigation to understand the effect of the architecture of block copolymers being blended on the shape of phase-separated domains. This will provide opportunities to develop an understanding of the non-spherical impact modification of polypropylene, discussed in detail in section 3.5.
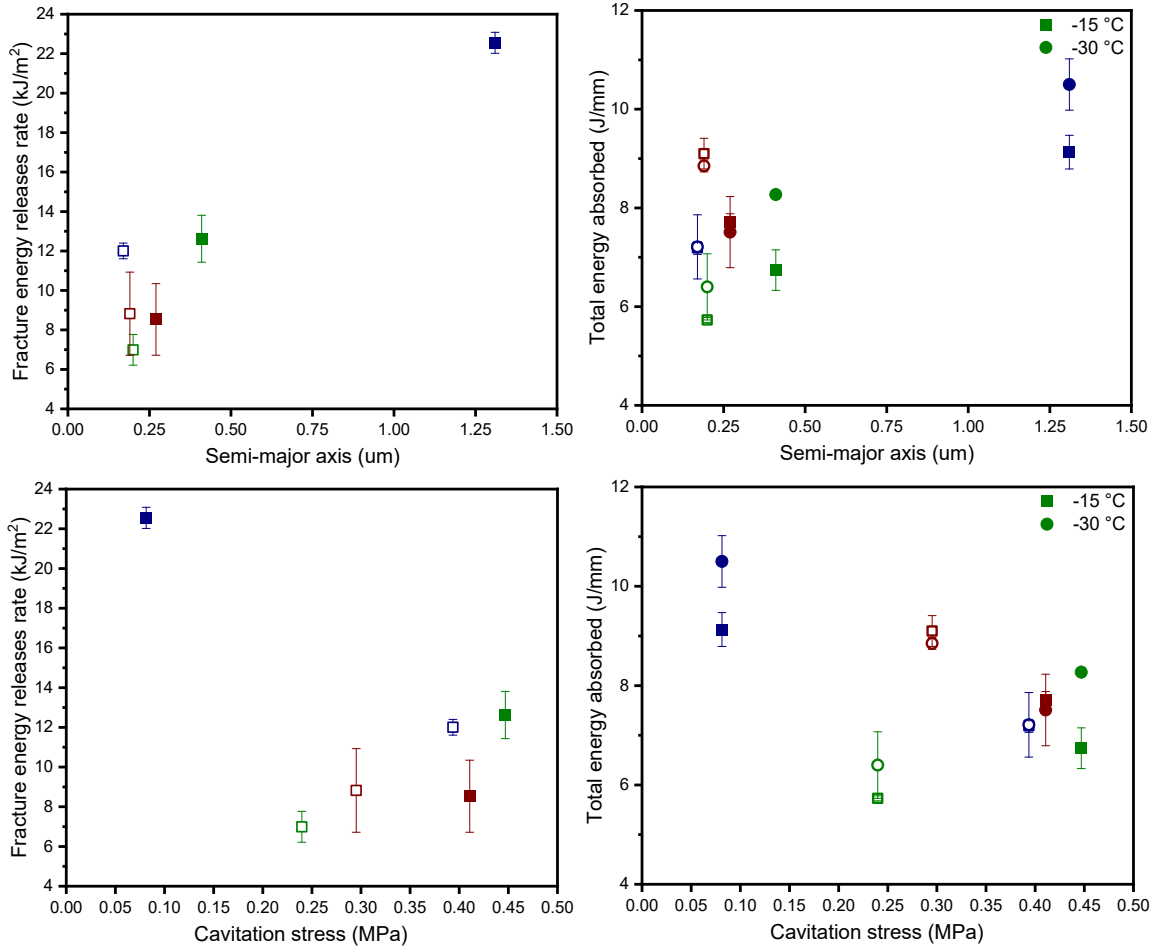
Figure 3.10 Room temperature fracture energy release rate (J_q) and Energy absorption under extreme conditions as a function of measured semi-major axis (a_c) and cavitation stress (σ_m), respectively (Closed symbols: without talc formulations; Open symbols: with talc formulations; green: POE; maroon: POE+SEBS; blue: SEBS).

3.3.5   Mechanical properties and morphology for polyoxymethylene formulations

Polyoxymethylene is an engineering thermoplastic. It combines high strength, excellent chemical resistance, and low coefficient of friction with properties typically associated with polymeric materials, such as processibility, corrosion resistance, and low cost. Additionally, it has a wide operating temperature range (-40 °C to 120 °C) and low moisture absorption. This makes it a suitable candidate to replace metals in demanding applications.[107, 135, 136] It is used in industrial, automotive, medical, and mechanical applications, such as gears, bearings, fittings, and electrical insulator parts.[137]

However, polyoxymethylene exhibits poor impact properties at room temperature. This limits the implementation of polyoxymethylene and makes it challenging. Polyoxymethylene is synthesized by polymerization of formaldehyde or formaldehyde trimer (trioxane). It has a linear backbone, and these highly structured molecular chains can pack better. This results in a high degree of crystallinity (up to ~70 %) and high density.[135, 138, 139] Yield stress typically scales with the percent crystallinity, and materials with high yield stresses tend to fail in a brittle manner.

Studies show that soft particle toughening improves the failure properties of polyoxymethylene. This is typically achieved using elastomers and block copolymers, such as thermoplastic polyether- and polyester-based polyurethanes, acrylate elastomers, EPDM rubber, EVA, and PETG.[140-143] However, improving the impact properties of polyoxymethylene is difficult for a variety of reasons. A high concentration of additives is required to achieve the desired impact properties. It reduces the stiffness and strength of the material. Further, in some cases, co-continuous morphology is necessary to improve the fracture toughness.[128, 135] Polyoxymethylene chains are also susceptible to degradation

and chain scission.[135] As a result, there are limited reports on soft particle toughening of polyoxymethylene in comparison with other semi-crystalline polymers. In this chapter, we focus on the soft particle toughening of polyoxymethylene.

Immiscible polymer blends often exhibit spherical morphology for the dispersed phase. This morphology minimizes the interface area where interfacial energies are high. Compatibilization of a polymer blend reduces the interfacial tension and provides control over the morphology.[117] There are two common approaches for compatibilization. First, incorporation of a graft or block copolymer called a compatibilizer. In some cases, compatibilizers are synthesized using reactive mixing.[144, 145] Second, the in-situ formation of a block copolymer at the interface.[146] Compatibilizer obtains different morphologies, such as core-shell or encapsulated domains and often, reduces the domain sizes.[145, 147] Herein, we investigate the approach of using compatibilizers to obtain non-spherical domains.

In this chapter, homopolymer and block copolymer additives were studied to achieve improved fracture toughness for polyoxymethylene. A detailed investigation was performed to determine the appropriate particle size and concentration for effective impact modification. Additionally, we prepared a compatibilizer/adduct using reactive mixing and illustrate its effect on the morphology, thermal and mechanical properties. These properties are evaluated using scanning electron microscopy (SEM), differential scanning calorimetry (DSC), and tensile testing, respectively.

Polyoxymethylene formulations modified with block copolymeric additives were investigated for effective soft particle toughening. These block copolymers are selected such that they are miscible with polyoxymethylene in the melt but generate phase-separated

domains upon cooling. Herein, we investigated three block copolymers which are SEBS, SEBS-*g*-MA, and SIS. SEBS is a proven impact modifier for thermoplastic polyolefins.[13] It is made up of styrene and ethylenic blocks. SIS contains unsaturated isoprene block. This unsaturation provides opportunities for further functionalization or reactive mixing. Polyoxymethylene is a weakly polar homopolymer. SEBS-*g*-MA contains polar carbonyl moieties associated with maleic anhydride functional groups. Such favorable interactions can improve the compatibility between the additive and the matrix. This facilitates stronger interphase, narrow particle size distribution, and smaller particle size.[140, 148]

Soft particle toughening for polyoxymethylene was investigated using a uniaxial tensile test instead of fracture toughness tests. Calorimetric studies show that polyoxymethylene used in this work exhibits 65% crystallinity. Yield stress for semi-crystalline polymers scales with percent crystallinity. Materials with high yield stresses show poor impact properties. Such high yield stresses lead to a brittle failure for polyoxymethylene at room temperature. As a result, the tensile test can provide a reasonable understanding of rubber toughening.

Polyoxymethylene formulations containing SEBS-*g*-MA at concentrations ranging from 2.5 wt.% to 30 wt.% were prepared. These formulations were characterized to determine the optimum concentration that achieves the most effective toughening. Figure 3.11 shows the stress versus strain curves for these formulations. Elastic modulus, yield stress, and rupture energy density are evaluated from these curves.
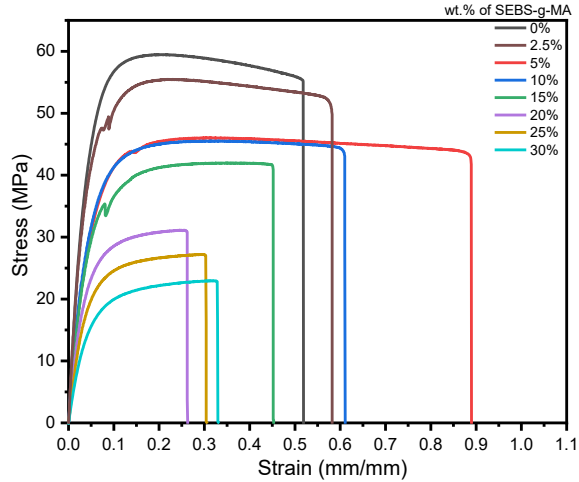
Figure 3.11 Representative stress versus strain curves for polyoxymethylene formulations containing SEBS-*g*-MA at varying concentrations.

Incorporating SEBS-*g*-MA decreases the elastic modulus as well as yield stress. Reduction in modulus and yield stress is proportional to the concentration SEBS-*g*-MA. SEBS-*g*-MA is a soft elastomer with extremely low modulus and does not contribute to matrix materials strength and stiffness. Reuss model and Voigt model predict the lower bound and upper bound of composite material properties, respectively.[149] Modulus values for SEBS-*g*-MA modified polyoxymethylene formulations lie within the predicted lower bound and upper bound, as shown in Figure 3.12-(a). Such intermediate modulus values indicate the absence of any favorable interactions between the dispersed phase (SEBS-*g*-MA) and the continuous phase (POM).[150] SEBS-*g*-MA contains a low concentration of maleic anhydride groups (~2 wt.%) and it is insufficient to strengthen the interface with the POM.

Figure 3.12-(b) shows yield stress for these formulations and theoretical yield stress. This theoretical model assumes SEBS-*g*-MA acts as a void and does not contribute to the yield stress. As a result, the theoretical yield stress is estimated using a rule of mixtures ($\sigma_y = \sigma_{y0}(1 - c)$). Yield stress values lower than the rule of mixture predictions

suggests a weak interface. These values are much lower than predicted. It indicates a complex underlying mechanism.
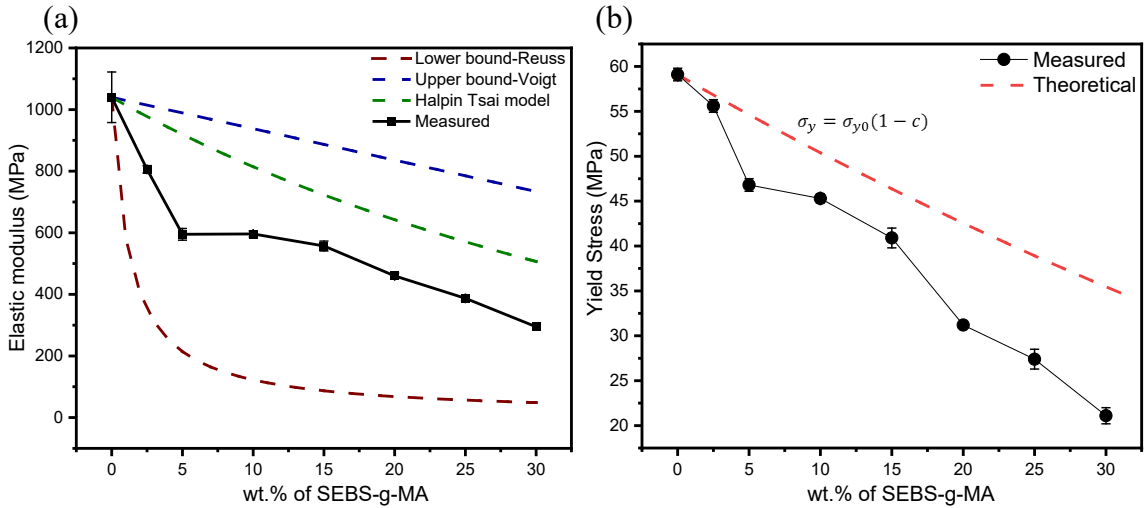
Figure 3.12 (a) Elastic modulus and (b) yield stress for polyoxymethylene formulations containing SEBS-*g*-MA compared with the theoretical models.
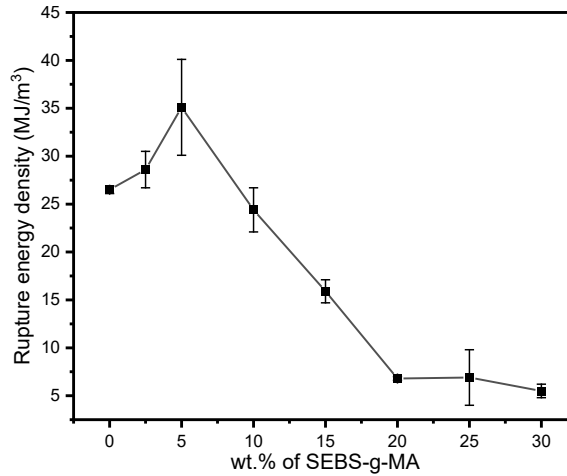
Figure 3.13 Rupture energy density for polyoxymethylene formulations containing SEBS-*g*-MA as a function of concentration.

On the other hand, rupture energy density and strain-at-failure increase with the concentration up to 10 wt.%. With further increase in the concentration, these formulations demonstrate poor properties than polyoxymethylene control, as shown in Figure 3.13. Polyoxymethylene modified with optimum concentration (5 wt.%) of SEBS-*g*-MA results in the most significant improvement (32%) in rupture energy density. Particle size, inter-

particle spacing, and concentration are interrelated.[77] Optimum concentration results in the appropriate size and inter-particle spacing for phase-separated domains. Such optimized morphology is necessary for superior energy absorption to occur. The optimum concentration also depends on the identity of the additive. For polyoxymethylene modified with SEBS-*g*-MA, the most effective toughening is realized at 5 wt.% concentration.

Morphology of polyoxymethylene formulations modified with SEBS-*g*-MA was investigated to illustrate the effects of concentration on particle size. Herein, we consider two extreme formulations containing 5 wt.% and 30 wt.% of SEBS-*g*-MA, as shown in Figure 3.14.
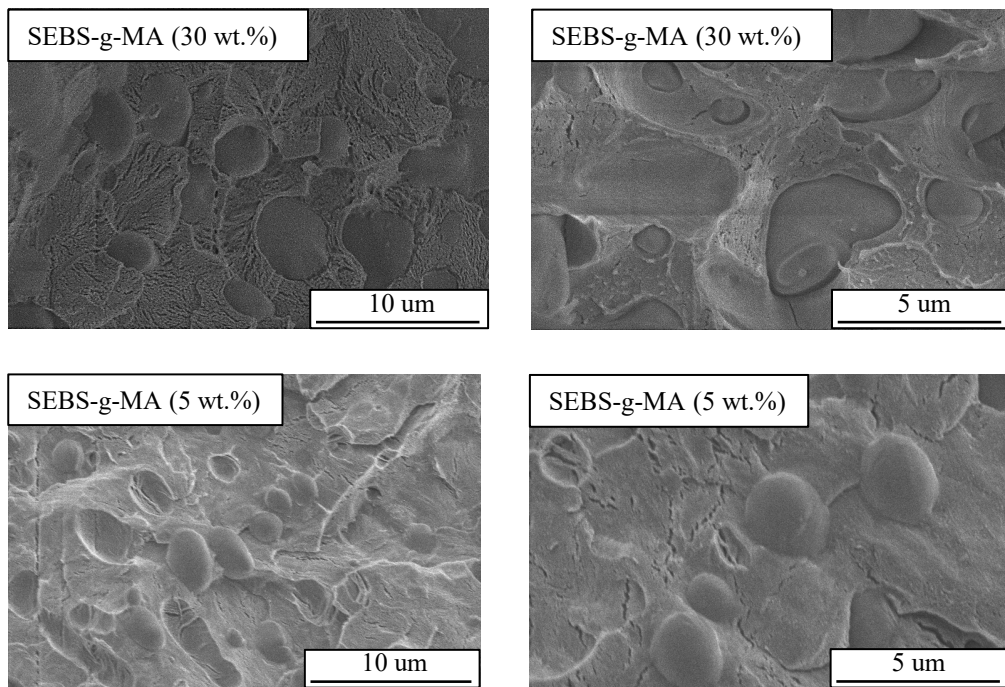
Figure 3.14 Morphology for polyoxymethylene formulations containing SEBS-*g*-MA at 30 wt.% and 5 wt.%, respectively.

At 30 wt.%, SEBS-*g*-MA generates a broad size distribution of phase-separated domains with particle sizes ranging from 1 to 7 um. However, at 5 wt.%, it phase-separates to achieve a narrow size distribution of domains with sizes ranging from 1 to 4 um. These domains exhibit an average particle size (semi-major axis a) of 1.3 um at 5 wt.%

concentration. At both concentrations, the SEBS-*g*-MA phase-separates to form spherical or ellipsoidal domains. Particle size scales with the concentration.[77] Optimum particle size results in the most effective impact modification. Particles larger than optimum can act as defects. Particles smaller than the optimum are difficult to cavitate which is necessary for plastic deformation to occur. Polyoxymethylene exhibits superior energy density when rubbery domains with 1.3 um size are present.

Polyoxymethylene modified with SEBS and SIS were also investigated for soft particle toughening. These formulations were modified with an optimum 5 wt.% of the block copolymer. Figure 3.15 shows stress versus strain plots for impact modified formulations. Measured yield stress, elastic modulus, and rupture energy density are tabulated in Table 3.4. Incorporating SEBS and SIS reduces the yield stress and the elastic modulus. SEBS and SIS are elastomeric block copolymers with low stiffness. Their addition results in the reduction of materials stiffness and strength.

Polyoxymethylene (POM) formulations	Modulus (GPa)	Yield Stress (MPa)	Rupture energy density (MJ/m³)
POM Control	1 ± 0.08	59.1 ± 0.7	26.5 ± 0.4
POM + 5 wt.% SEBS-g-MA	0.6 ± 0.02	46.8 ± 0.7	35.1 ± 5
POM + 5 wt.% SEBS	0.8 ± 0.02	50.1 ± 0.6	35.4 ± 5
POM + 5 wt.% SIS	0.6 ± 0.05	54 ± 0.1	39.8 ± 4

Table 3.4 Mechanical properties for polyoxymethylene formulations containing SEBS-*g*-MA, SEBS, and SIS.
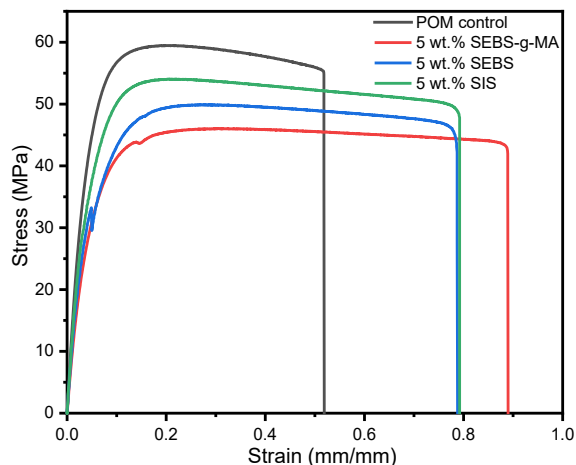
Figure 3.15 Representative stress versus strain curves for polyoxymethylene formulations containing SEBS-*g*-MA, SEBS, and SIS.

These formulations demonstrate higher strain-at-failure and rupture energy density than the control polyoxymethylene. SIS results in the most significant improvement of 55% in the rupture energy density. SEBS-*g*-MA exhibits the highest strain-at-break. Notably, these formulations exhibit a neck formation during the tensile testing. Necking is a typical post-yield response for ductile polymers, such as polycarbonate. Neck formation results from a strain localization in the gauge area. It allows polymer chains to be drawn in the loading direction. This contributes to energy absorption *via* plastic deformation.

Figure 3.16 shows the morphology for the impact modified polyoxymethylene formulation. These formulations contain 5 wt.% of SEBS and SIS, respectively. SEBS phase-separates into 2 um to 10 um large domains. These domains are mostly spherical, while some domains exhibit elongated and ellipsoidal shapes. SEBS-*g*-MA exhibit similar domain shapes. However, it shows a narrow size distribution and smaller domain sizes (1 to 4 um). Interestingly, SIS affords submicron size domains. These domains are spherical.
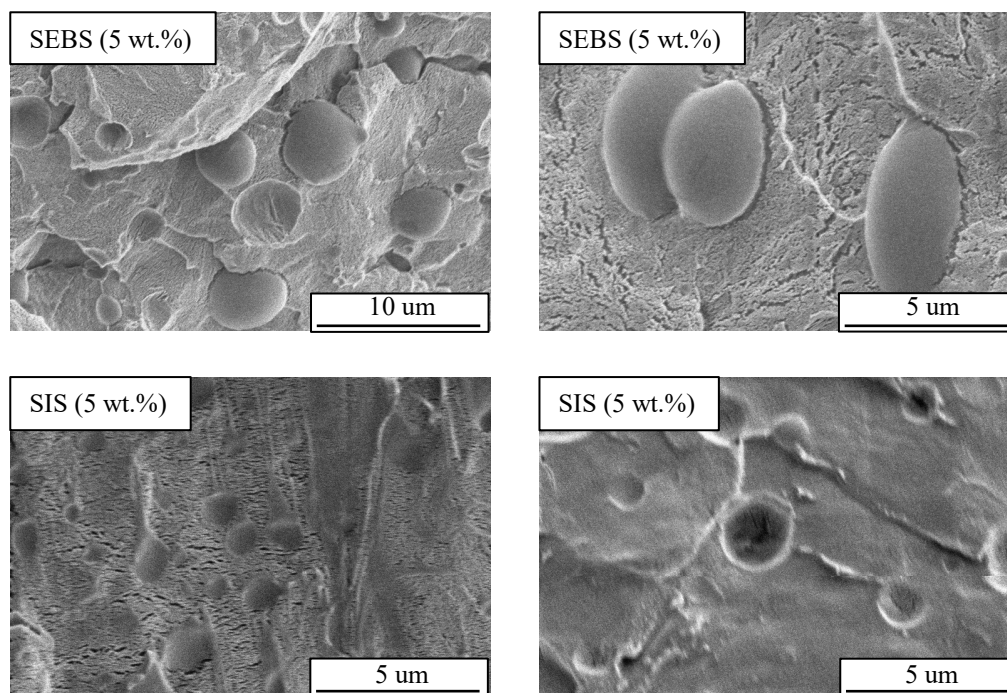
Figure 3.16 Morphology for polyoxymethylene formulations containing SEBS and SIS at 5 wt.%, respectively.

The morphology of the impact modified polyoxymethylene formulations was further analyzed using image analysis. Particle perimeter and area for approximately 150 domains were measured. These domains were analyzed as a 2-dimensional ellipse, following the procedure described in section 3.3.2. Semi-major axis "a", semi-minor axis "b", and the aspect ratio "a/b" (shape factor) are tabulated in Table 3.5

Polyoxymethylene (POM) formulations	"a" (um)	"b" (um)	"a/b"
POM + 5 wt.% SEBS-g-MA	1.3 ± 0.5	0.7 ± 0.1	1.9
POM + 5 wt.% SEBS	1.6 ± 0.9	0.7 ± 0.1	2.3
POM + 5 wt.% SIS	1.1 ± 0.4	0.7 ± 0.1	1.6

Table 3.5 Average semi-major axis (a), semi-minor axis (b), and aspect ratio (a/b) for phase-separated domains of polyoxymethylene formulations containing SEBS-g-MA, SEBS, and SIS analyzed as ellipses.

SEBS exhibits a larger average semi-major axis (1.6 um) than SEBS-*g*-MA (1.3 um). On the other hand, SIS results in an average semi-major axis of 1.1 um. Particle size

depends on molecular weight, solubility parameter, architecture, and interactions with the matrix.[127-129] Further, SEBS-*g*-MA and SEBS have different molecular weights and polystyrene contents. Besides, maleic anhydride functional groups of SEBS-*g*-MA provide favorable interactions with the matrix, unlike SEBS. This results in a much finer particle size distribution for SEBS-*g*-MA.

SEBS, SEBS-*g*-MA, and SIS improve the impact properties of polyoxymethylene. These improvements result from the formation of rubbery domains of appropriate size and inter-particle spacing. SEBS-*g*-MA leads to the most significant improvement when blended at 5 wt.% concentration and generates 1.3 um large domains. However, further investigation will be needed to estimate the optimum concentration and corresponding optimum particle size for SIS and SEBS.

3.3.6   Polyoxymethylene formulations modified with prepared elastomeric adducts

Soft particle toughening for polyoxymethylene, as discussed in the previous section, depends on the size, the concentration, and the inter-particle spacing of rubbery domains. These block copolymers generate spherical, ellipsoidal, or elongated domains upon TIPS in polyoxymethylene matrix. Next-generation impact modification, studied in this chapter, indicates that impact properties also depend on particle shape. Non-spherical domains can provide more effective toughening than conventional spherical soft particle toughening.

Herein, we investigate the strategy of using compatibilizers or adducts to obtain non-spherical rubbery domains. Recently, Chang-Sik and coworkers prepared a compatibilizer for PBT/EVA blend *via* reactive mixing using peroxides.[144, 145] In this work,

adducts are prepared using reactive mixing. Block copolymers SEBS, SEBS-*g*-MA, and SIS were melt-mixed with dicumyl peroxide (DCP) to obtain elastomer-polyoxymethylene adducts. These adducts were prepared with 20, 50, and 80 wt.% of block copolymer concentration. Polyoxymethylene formulations containing 5 wt.% of these adducts were characterized for their morphology, thermal, and mechanical properties.

SEBS, SIS, and SEBS-*g*-MA are ideal candidates for making elastomeric adducts. These block copolymers have similar backbone architecture with styrene and ethylene or isobutylene blocks. However, they offer different chemical functionalities. SEBS-*g*-MA is functionalized with maleic anhydride groups and SIS is an unsaturated block copolymer. These functionalities provide opportunities for grafting or crosslinking.

Elastomeric adducts show melting temperature and percent crystallinity similar to polyoxymethylene homopolymer (Appendix Figure A3.3). However, crystallization temperature decreases with an increase in the concentration of elastomer present in the adduct. Elastomeric adducts when prepared using 80 wt.% of elastomer results in multiple, lower temperature crystallization exotherms. Polyoxymethylene is prone to thermal degradation. Melt mixing polyoxymethylene with radical initiator DCP can lead to polyoxymethylene chain scission. Further, inhomogeneous elastomeric adducts can result in multiple crystallization peaks. In addition, the chemical modification that occurred during the reactive mixing might alter the crystallization characteristics as well.

Figure 3.17 shows the morphology for polyoxymethylene formulations containing 5 wt.% of elastomeric adducts. SEBS and SIS adducts phase separate into spherical or ellipsoidal domains. SEBS adduct domains are 3 to 10 um in size and SIS adducts are 0.2 to 2 um in size. Reactive mixing does not result in any change in the morphology for SEBS

93

and SIS. These adducts show similar domain sizes and shape to that of unreacted SEBS and SIS, respectively.
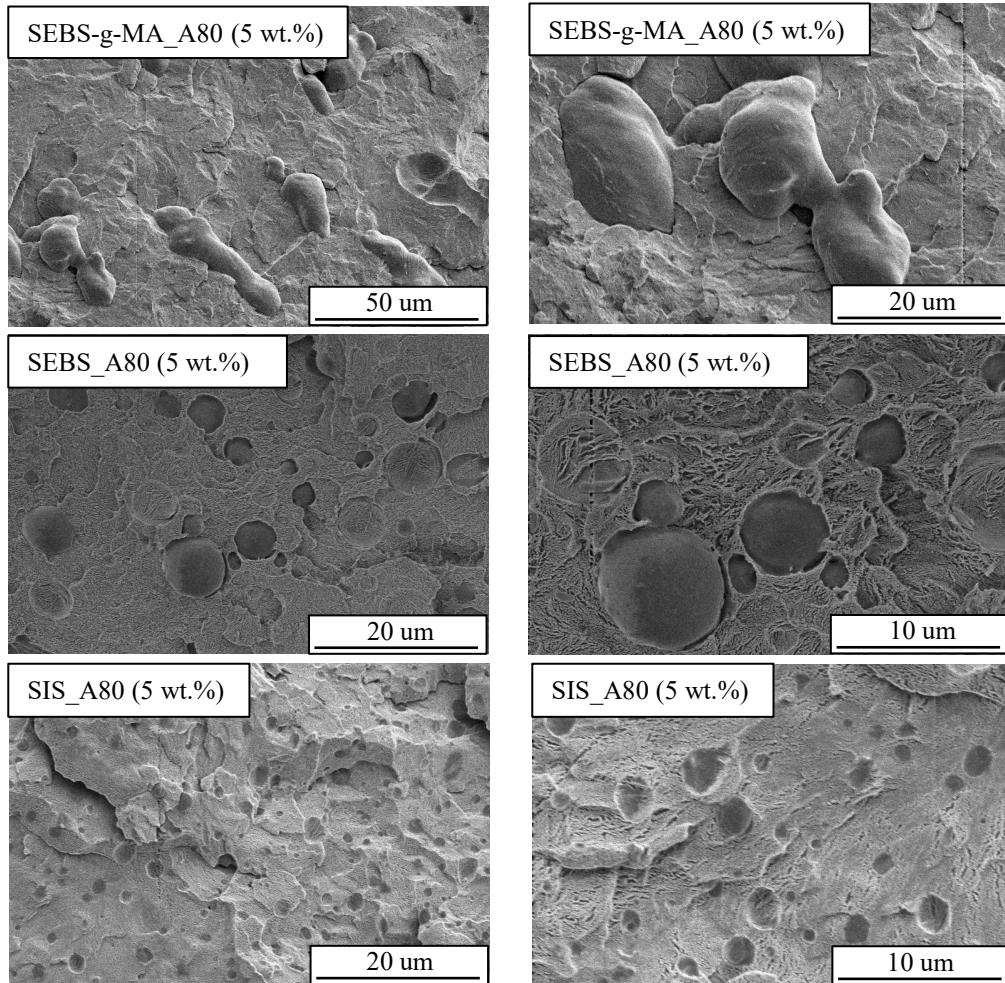
Figure 3.17 Morphology for polyoxymethylene formulations containing SEBS-*g*-MA, SEBS, and SIS adducts at 5 wt.%, respectively.

Notably, SEBS-*g*-MA adduct generates highly irregular and unusual domains. These domains are highly elongated and, in some cases, appear to have fused together. Their morphology suggests that these domains are trapped in their shape. However, these domains are relatively large with sizes in the range of 10 to 50 um. Such large domains act as defects. It leads to premature material failure before plastic deformation can occur. It is necessary to realize these non-spherical domains in sizes suitable for toughening. Altering

94

the processing parameters (for example, screw speed, processing temperature, and viscosity) results in domains on the same length scale. Even after altering the processing conditions, these domains still achieve irregular and non-spherical shapes. Processing conditions do not affect the size and shape of these domains. Although precise reactions that occur during the reactive mixing are unknown, chemical crosslinking between SEBS-g-MA and polyoxymethylene is likely.

The quantitative analysis for elastomeric adduct domains is tabulated in Table 3.6. SEBS and SIS adducts exhibit average semi-major axis (a) of 2.1 um and 1 um, respectively. These domains achieve a shape factor of 3 and 1.3, respectively. Most importantly, SEBS-g-MA adducts show a shape factor of 25 and an average semi-major axis (a) of 13.5 um. Such a high value of shape factor demonstrates highly non-spherical and unusual domain shapes.

Polyoxymethylene (POM) formulations	"a" (um)	"b" (um)	"a/b"
POM + 5 wt.% SEBS-g-MA_A80	13.5 ± 6.5	0.6 ± 0.1	25
POM + 5 wt.% SEBS_A80	2.2 ± 0.9	0.7 ± 0.1	3
POM + 5 wt.% SIS_A80	1 ± 0.3	0.7 ± 0.1	1.4

Table 3.6 Average semi-major axis (a), semi-minor axis (b), and aspect ratio (a/b) for phase-separated domains of polyoxymethylene formulations containing SEBS-g-MA, SEBS, and SIS adducts analyzed as ellipses.

Figure 3.18 shows stress versus strain plots for polyoxymethylene modified with elastomeric adducts. These formulations exhibit reduction in the elastic modulus and yield stress. Nonetheless, elastomeric adduct achieves higher modulus than just elastomeric block copolymer itself when incorporated at the same concentration. Elastomeric adducts also contain polyoxymethylene chains. Polyoxymethylene is either blended or reacted with the elastomer. This leads to a marginally higher stiffness. SEBS and SIS adducts show

failure properties similar to polyoxymethylene control. Reactive mixing can result in the degradation of polyoxymethylene. This results in the lack of improvements in the mechanical properties. SEBS-*g*-MA adducts result in brittle failure. These formulations exhibit a lower strain-at-break in comparison with polyoxymethylene control. These poor mechanical properties result from the presence of larger domains/defects.
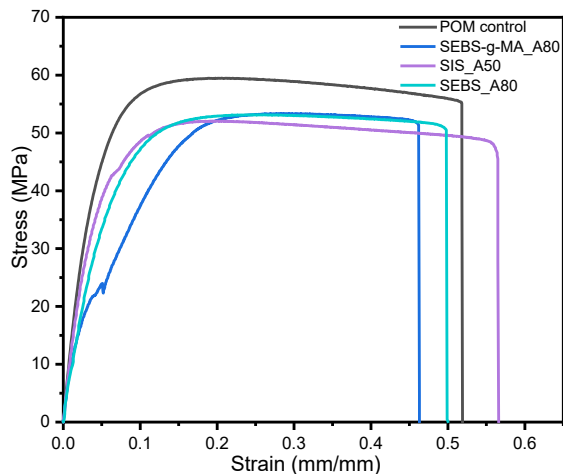
Figure 3.18 Representative stress versus strain plots for polyoxymethylene formulations containing SEBS-*g*-MA, SEBS, and SIS adducts at 5 wt.%, respectively.

A comparison of morphologies achieved for SEBS, SEBS-*g*-MA, and SIS adducts suggests that maleic anhydride functionality is a must to achieve high aspect ratio non-spherical domains. Reactive mixing enables developing unique adducts with unusual morphologies. For effective impact modification, it is necessary to engineer their particle size and further work is needed to achieve the desired particle size and shape.

3.4 Conclusions

We investigated next-generation, non-spherical impact modification for crystalline thermoplastics polypropylene and polyoxymethylene. We studied two different strategies to obtain non-spherical phase-separated domains. First, blending two block copolymers in

polypropylene melt generates elongated and ellipsoidal domains upon TIPS. Second, preparing elastomeric adducts *via* reactive mixing results in unusual, higher curvature domains when melt mixed with polyoxymethylene.

Polypropylene modified with POE or SEBS or a blend of POE and SEBS exhibits spherical and non-spherical ellipsoidal domains. Incorporating talc reduces the domain sizes while maintaining the particle shape. Impact properties of engineered polypropylene formulations show a strong dependence on particle size at quasi-static room temperature testing as well as extreme condition (subzero temperatures, high-strain rate) testing. Polypropylene containing SEBS shows larger domains (average a = 1.3 um) and demonstrates the most significant toughness improvement. Notably, under extreme loading conditions, particle cavitation is not the failure mechanism, instead, energy absorption occurs *via* craze nucleation and craze stabilization. Larger (1 to 2 um) domains result in enhanced particle-particle interactions and interconnected craze formation, thereby achieving superior energy absorption.

Block copolymers SEBS, SEBS-*g*-MA, and SIS improves the toughness of polyoxymethylene without compromising its high crystallinity. Impact modified polyoxymethylene achieves up to 50% enhancement in the rupture energy density when engineered with optimum concentration (5 wt.%) of the impact modifiers that generates the optimum particle size (1 to 2 um). Polyoxymethylene containing SEBS-*g*-MA based elastomeric adducts exhibit irregular and non-spherical domains. This morphology likely results from the chemical modification that occurs during the reactive mixing. These domains possess high curvature and a very high shape factor of 25. However, larger domain

sizes of these domains are detrimental to impact properties and future studies are necessary to obtain non-spherical domains with the desired size.

3.5   Future work

This chapter demonstrates different strategies to realize non-spherical impact modification for semi-crystalline thermoplastics. However, future studies are required to develop an understanding of the next-generation impact modification.

Impact properties for polypropylene show a strong dependence on particle size. However, the precise morphology is much more complicated. Domains have a broad size distribution and variation in shapes, such as spherical, ellipsoidal, and irregular domains. Therefore, there is a need for quantitative stereology. Quantitative stereology using Saltikov's analysis for spherical domains and Dehoff's analysis for ellipsoidal domains can provide a better illustration of size distribution. Further, a better descriptor for domain shapes is needed. Elongated and ellipsoidal domains can be treated as ellipses to provides qualitative information for comparing different morphologies. However, modeling highly unusual morphologies, for example, the morphology of SEBS-*g*-MA-based elastomeric adducts in polyoxymethylene, as an ellipse is an unjustified simplification. Therefore, a shape factor that provides a holistic perspective for domain morphology and takes into account the highest local stress concentration, surface area to volume ratio, opportunities for particle-particle interactions, and interparticle spacing needs to be identified.

Further, the concept of non-spherical impact modification should be expanded for different polymeric systems. In addition to the next-generation impact modification discussed in this chapter, previous work in the Lesser group has shown non-spherical

impact modification for glassy epoxy composites. Nonetheless, this technology can be studied for different thermoset or thermoplastic materials and different processing techniques, such as injection molding, 3D printing, and electrospinning. In addition, different strategies should be investigated to realize non-spherical domains by taking advantage of hyperbranched or dendritic polymers, brush block copolymers, and selectively etched or selectively grafted copolymers to access different unusual and interesting morphologies. Understanding the morphology evolution will allow us to gain insights into the kinetics of phase-separation and enable designing process or molecular parameters to achieve desired morphology. Future studies should focus on developing a technique or utilizing the existing technique, such as SEM, AFM, or optical microscopy, for in-situ imaging of TIPS or RIPS.

Next-generation impact modification and associated micromechanics can be further understood with the help of modeling and simulation studies. Conventional, spherical impact modification is well studied for a variety of polymeric systems and especially, in terms of understanding the underlying fracture mechanics. However, a thorough finite element modeling is needed to qualitatively as well as quantitatively describes the effect of particle shape on stress or strain fields around the crack tip or cavitated domains, factors affecting cavitation, local stress concentrations, the effect of anisotropy associated with non-spherical domains, and modes of failure. During the collaborative project on impact modification of polyoxymethylene, preliminary finite element modeling work for ellipsoidal domains was conducted by BASF, however, there remains a lot of future opportunities in the field of next-generation, non-spherical impact modification.

CHAPTER 4

MULTIFUNCTIONAL MISCIBLE ORGANOPHOSPHORUS ADDITIVES FOR FLAME RETARDANCE AND FORTIFICATION OF HIGH T$_g$ EPOXY RESINS

4.1   Introduction

Epoxide networks are ubiquitous in polymer materials chemistry and engineering since they offer exceptionally useful thermal and mechanical properties, as well as superior chemical and corrosion resistance, dimensional stability, and adhesion. Therefore, cured epoxy thermosets are used in numerous automotive, aerospace, and electronics applications.[151-153] However, certain traits of epoxy thermosets, including their inherent flammability, create problems in several materials settings.[154, 155] Conventionally, the fire risk of epoxy networks is mitigated by incorporating halogenated organic flame retardants into the matrix. While halogens, especially aromatic bromides, effectively reduce the heat release of epoxies by acting as gas phase flame retardants,[156] the resultant release of corrosive and toxic gas introduces health and safety concerns.[157] In addition, environmental legislation concerning the manufacture of halogenated molecules complicates their continued use, such that the discovery of halogen free flame-retardant polymers and additives takes on increasing importance.[158, 159] Flame retardant strategies involving inorganic additives provide a condensed phase mechanism for dissipating heat and forming a protective barrier to slow combustion.[157] While these inorganic compounds are generally environmentally benign, the high concentrations required to impart low heat release properties perturb the desired physical/mechanical properties of the polymer matrix.[160] Thus, there remains a pressing need to combine inherently flame retardant polymer materials with additives that offer mechanisms to improve materials properties.

100

Organophosphorus compounds are promising alternatives to halogenated flame retardants, as seen in epoxy networks in which phosphorus groups are used either as additives or as part of the covalently cross-linked network.[161, 162] Experimental evidence suggests that phosphorus acts both in the gas phase to inhibit flame propagation (by quenching free radicals) and in the condensed phase to form an inorganic "glass" barrier.[163] Recent studies have shown synergistic improvements in char formation and superior flame-retardant performance when phosphorus-containing additives are combined with condensed phase flame retardants.[153, 155, 164, 165] Among phosphorus-containing flame-retardant additives, dimethyl methylphosphonate (DMMP) has produced favorable results in polyurethane foams as well as battery housing.[166-171] Moreover, prior studies in our laboratories showed that even low concentrations (≤ 10 parts per hundred (phr)) of DMMP efficiently reduce flammability in aliphatic epoxy networks.[172]

In combination with polymers, organophosphorus additives may decrease process viscosity and, in some cases, reduce matrix stiffness due to plasticization.[173] In contrast, some reports have identified phosphorus-based small molecule additives as "fortifiers" for aliphatic epoxy networks, in which the fortifiers function as processing aids while simultaneously increasing yield stress and stiffness by network densification (*i.e.* filling free volume).[172, 174, 175] Specifically, previous studies on organophosphorus additives showed that lower molecular weight compounds, such as trimethyl phosphate and DMMP, to be more efficient fortifiers than bulkier examples *(e.g.*, triphenyl phosphate) affording cured epoxy networks with minimal reduction of glass transition temperature (T_g).[176] Notably, prior work by Spiess described organophosphorus additives as participating in

ion pair formation and electrostatic interactions that determined the extent of fortification and mechanical enhancement.[177]

We systematically investigated the thermal and mechanical properties of high T_g epoxy networks in the presence of an organophosphorus additive, building on recent studies that showed deoxybenzoin-based epoxies to have significantly lower heat release and comparable physical and mechanical properties relative to conventional bisphenol A-based epoxies.[178, 179] Interesting recent reports by others described deoxybenzoin-based polyarylate additives to increase the thermal stability of polyether ester elastomers, with a synergistic flame-retardant behavior in the presence of a phosphorus-containing flame retardant.[180] Moreover, Hu described blending deoxybenzoin and phosphorus-based additives with poly(trimethylene terephthalate) to give a synergistic response in char formation (condensed phase) and flame-inhibition (vapor phase).[181] Thus, deoxybenzoin-based groups are excellent flame retardants in their own right and in some cases appear to exhibit synergistic interactions with phosphorus-containing additives.[182]

In this chapter, organophosphorus additives are investigated for simultaneous mechanical fortification and reduced flammability in aromatic and aliphatic epoxy thermosets. Specifically, we investigated epoxy networks produced by curing the diglycidyl ether of bisphenol A (DGEBA) and the diepoxide of bis-hydroxydeoxybenzoin (BEDB) with aromatic and aliphatic amines in the presence of DMMP. The thermal and mechanical properties of these cured epoxies were characterized by differential scanning calorimetry (DSC) and compression testing, and the heat release properties and flammability were characterized by microscale combustion calorimetry (MCC) and

vertical burn testing. The role of DMMP as both fortifier and flame-retardant was investigated further by NMR spectroscopy performed before and after burning.

4.2 Experimental

4.2.1 Materials

DOW DER 332, a commercial grade diglycidyl ether of bisphenol A (DGEBA), was supplied by Olin epoxy. BEDB, diglycidyl ether of 4,4'-bishydroxydeoxybenzoin (BEDB), was synthesized following a published procedure.[178] 4,4'-Diphenyldiamino sulfone (DDS) (97%), dimethyl methylphosphonate (DMMP) (97%), triethyl phosphate (TEP) (99%), trimethyl phosphate (TMP) (99%), triphenylphosphine oxide (TPPO) (98%), desoxyanisoin (98%), and pyridine hydrochloride (98%) were procured from Sigma-Aldrich. Epichlorohydrin (>99%) and 9,10-dihydro-9-oxa-10-phosphaphenanthrene-10-oxide (DOPO) were purchased from TCI. Jeffamine D-230 polyetheramine (D230) was purchased from huntsman chemicals. All other chemicals were purchased from Sigma-Aldrich and used without further purification.

4.2.2 Sample preparation

The general procedure for making epoxy thermosets involved mixing the epoxy resin (DGEBA or BEDB) with an organophosphorus additive (DMMP or TEP or TMP or TPPO), followed by the addition of a curing agent (DDS or D230). The resulting formulation was degassed (by vacuum) and poured into either cylindrical test tubes (internal diameter = 10 mm) or into a rectangular glass mold (thickness = 3.2 mm). Samples were cured in a nitrogen atmosphere. Aliphatic epoxy formulations were cured using

Jeffamine D-230 polyetheramine (D230) at 100 °C for 6 hours, whereas aromatic epoxy resins were cured using diphenyl diamino sulfone (DDS) at 200 °C for 6 hours, followed by a post-cure at 220 °C for 2 hours.

Specifically, high T_g epoxy formulations were prepared by mixing the epoxy resin (DGEBA or BEDB) with organophosphorus additive (DMMP) at 135 °C for 30 minutes. The concentrations of DMMP in the epoxy resin were blended to afford overall phosphorus content (wt.%) in the cured epoxy formulation of up to 2 wt.%. The curing agent, diphenyldiamino sulfone (DDS), was added to the resin and was stirred for 30 minutes to ensure complete dissolution of DDS. The resulting formulation was degassed (by vacuum) and poured into either cylindrical test tubes (internal diameter = 10 mm) or into a rectangular glass mold (thickness = 3.2 mm). The samples were cured in a nitrogen atmosphere at 160 °C for 6 hours, followed by a post-cure at 220 °C for 2 hours.

4.2.3   Thermal analysis

Differential scanning calorimetry (DSC) was performed on a TA Instruments Q200 to measure the glass transition temperature (T_g) of the cured epoxy resins. Samples were investigated over a temperature range from 0 to 220 °C at a heating/cooling rate of 10 K min^{-1} during a consecutive heat-cool-heat cycle. T_g was recorded as the inflection point of the transition observed during the second heating cycle.

Thermogravimetric analysis (TGA) was performed using TA Instruments Q50 in a $N_{2(g)}$ atmosphere using a platinum pan in the temperature range from 25 to 700 °C at 10 °C min^{-1} heating rate. Char residue was taken as the weight percent residue at 700 °C.

Dynamic mechanical analysis (DMA) was performed using TA instruments Q800 at a heating rate of 3 K min^{-1} in the temperature range of -120 to 275 °C to determine the storage modulus and tan delta as a function of temperature. The storage modulus at T_g+40 °C was ascribed as a rubbery plateau modulus.

4.2.4   Compression testing

Compression testing was performed on cylindrical specimens using an Instron 5800 at a constant crosshead rate of 2 mm min^{-1}. Non-standard cylindrical specimens with a diameter-to-height ratio of 1:1 and a diameter of 10 mm were used to prevent buckling of the samples. The top and bottom surfaces of the specimens were lubricated with silicone oil and Teflon tape. The recorded data was corrected for the compliance of the system and used to determine the elastic modulus, yield stress, and strain hardening modulus values of the cured epoxy resins (reported values are the average of at least three identically evaluated specimens).

4.2.5   Microscale combustion calorimetry

Microscale combustion calorimetry (MCC) was performed on samples weighing 2-4 mg following ASTM D7309-13.[183] Samples were heated from 75 to 750 °C at 1 K s^{-1} in an inert $N_{2(g)}$ atmosphere. The degradation products were then combined with 20 cc min^{-1} oxygen flow (80 cc min^{-1} nitrogen flow) in a combustion furnace at 900 °C to allow for complete combustion. The reported values from MCC are the average of at least three samples.

4.2.6   Vertical burn testing

Comparative burning characteristics of the cured epoxy formulations were determined using conditions similar to those of the ASTM D3801 vertical burn test.[184] Specimens with dimensions of 130 x 13 x 3.2 mm were cut from the cured epoxy plaque. Samples were positioned such that the longitudinal length of the sample was vertical and 10 mm of the lower end of the specimen was in contact with a propane flame (height = 40 mm) produced by a Bunsen burner while in atmospheric conditions. Samples were kept in contact with the flame for 10 seconds and t_1 (defined as the time required for the flame to self-extinguish after removal of the Bunsen burner flame) was recorded. The flame exposure was repeated for a second time and the corresponding extinguishing time was recorded as t_2.[184] Values for t_1 and t_2 were averaged for two or more specimens.

4.2.7   Scanning electron microscopy

The morphology of the charred surface was examined by a scanning electron microscope on a Magellan 400 equipped with a field emission gun. SEM imaging was performed on specimens tested on vertical burn test and samples were collected from the specimen end that had been in direct contact with the flame. These samples were sputter-coated with a thin layer of gold before SEM imaging.

4.2.8   Solid state NMR

Solution and solid-state ^1H, ^{13}C, and ^{31}P NMR experiments were performed on Brüker Avance III HD 500 MHz and 600 MHz spectrometers, respectively. Solid-state experiments were performed using high-power ^1H decoupling and direct polarization (DP)

with magic-angle spinning (MAS) at a speed of 8.6 kHz. Spinning side bands were separated by 8600 Hz, the spinning frequency used for the measurement. All NMR experiments were conducted at room temperature. ^{1}H T_1 and ^{31}P T_1 of the cured resins were estimated to be ~1.5 seconds and ~10 seconds, respectively. A recycle delay of 40 seconds was used for ^{31}P DP experiments, while a short recycle delay of 1 second was used for ^{13}C DP experiments to probe nuclei with short T_1 (such as the signal corresponding to the methyl group on DMMP). Chemical shift simulation was performed with ACDLabs 2018 NMR Predictor® software.

4.3 Results and Discussion

4.3.1 Thermal properties of aromatic epoxy networks containing organophosphorus additives

Epoxy resins were prepared using DGEBA, a stoichiometric amount of aromatic crosslinking agent diamino diphenyl sulfone (DDS), and 15 phr (parts per hundred resin) of organophosphorus additives DMMP, TMP, TEP, or TPPO (Figure 4.1). Herein, we investigate TMP and TEP (3 P-O bonds), DMMP (2 P-O bonds), and TPPO (0 P-O bonds) additives to evaluate the effect of a number of P-O bonds on condensed phase char formation and gas-phase flame inhibition for epoxy networks. Additionally, these additives also act as fortifiers for aliphatic epoxy networks and provide opportunities to obtain flame retardant fortified epoxy composites.[176]
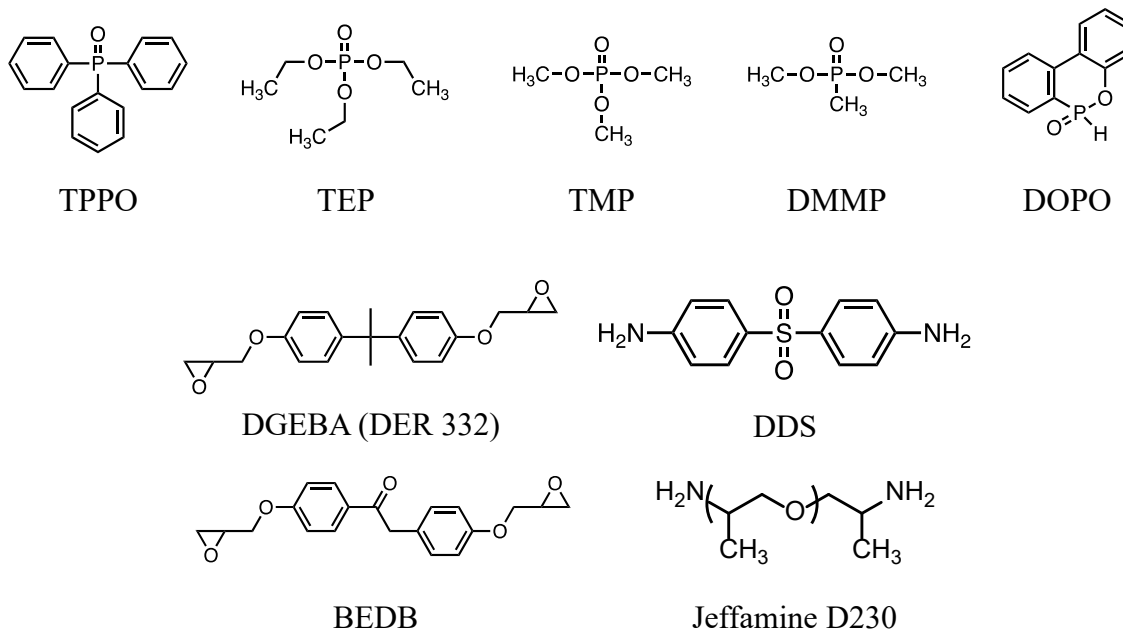
Figure 4.1 Chemical structures of epoxy resins, aliphatic and aromatic amines, and organophosphorus additives.

The Thermal and heat release properties of these epoxy networks were studied using the thermogravimetric analysis (TGA). Epoxy networks are degraded under an inert nitrogen atmosphere in a TGA that mimics their burning behavior in the pyrolysis zone of a flame. Further, the rate of degradation indicates the rate of fuel generation during the burning process, and as a result, the flammability of material scales with the rate of degradation. Figure 4.2 shows the weight loss and rate of degradation as a function of temperature for these epoxy networks. The control DGEBA epoxy networks are thermally stable up to ~350 °C and exhibit a single step degradation process at 410 °C, followed by steady degradation to achieve 12 wt.% of char at 700 °C. Incorporating organophosphorus additives lowers the onset of degradation temperature and reduces the maximum rate of degradation. Epoxy network containing TPPO (no P-O single bonds) shows an earlier onset of degradation at 275 °C, however, exhibits a comparable maximum rate of degradation and char content with that of control epoxy networks. Epoxy networks containing TMP

and TEP (3 P-O bonds) achieve high char content of ~30 wt.% and show the most significant decrease in the degradation onset temperature and the maximum rate of degradation. DMMP (2 P-O bonds) also reduces the maximum rate of degradation and results in the formation of 25 wt.% of char at 700 °C. Interestingly, epoxy networks comprising of DMMP show intermediate values for char content and degradation onset temperature.
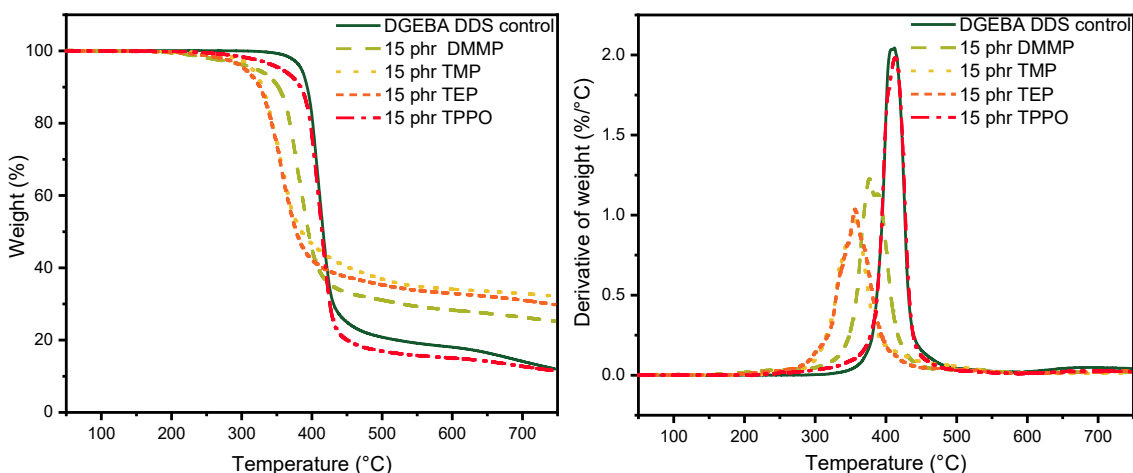
Figure 4.2 TGA thermograms for DGEBA epoxy networks containing 15 phr of DMMP, TMP, TEP, and TPPO.

TMP, TEP, and DMMP are low molecular weight additives that boil during the degradation and thereby, demonstrate an earlier onset of degradation. These additives produce condensed phase char that prevents the burning of the underlying material. Additionally, phosphorus-based moieties quench the high-energy free radicals produced during the burning process and minimize the rate of combustion. This reduces the rate of degradation for these epoxy networks. The char content for investigated epoxy networks increases with the number of P-O bonds, whereas the onset of degradation temperature and maximum rate of degradation decreases. On contrary, recent studies have shown that the propensity for char formation increases with the degree of oxygenation (number of P-O bonds) of phosphorus-containing crosslinkers.[163] The degradation characteristics depend

on whether phosphorus moieties are covalently bound with the network or are unbound additives. Amongst the additives that were investigated, DMMP affords the optimum balance between the lower rate of degradation, higher char content, and undesirable earlier onset of degradation temperature. As a result, consequent studies focus on the effect of the concentration of DMMP on the thermal, mechanical, and heat release properties of epoxy networks.

4.3.2   Thermal and mechanical properties of DMMP-containing epoxy networks

Epoxy resins were prepared from diepoxide monomers, either DGEBA or BEDB, with a stoichiometric equivalent of crosslinking agent, diamino diphenyl sulfone (DDS), in the presence of DMMP (Figure 4.1). DMMP concentrations of 2-8 weight percent were employed, corresponding to 0.5-2.0 elemental weight percent phosphorus.

The physical and mechanical properties of the phosphorus-containing networks were characterized by several methods, including DSC to evaluate their fundamental thermal properties. DGEBA- and BEDB-based formulations, without DMMP, showed nearly identical T_g values of 205 °C and 201 °C, respectively (Figure 4.3). Adding DMMP to the DGEBA-based networks results in a small initial increase in T_g at low phosphorus weight percent (0.5 wt.%), followed by a substantial decline at higher phosphorus content. BEDB-containing epoxy networks demonstrate a steady decline in T_g with increasing phosphorus concentration. The most significant influence of DMMP, resulting in 40 °C reduction in T_g, is observed for formulations containing two weight percent phosphorus. Based on the thermal properties of DMMP-containing epoxy networks, we hypothesize that increasing phosphorus concentration beyond two weight percent will further reduce T_g

to a level that is deleterious to the overall desired thermal and mechanical properties of the material.
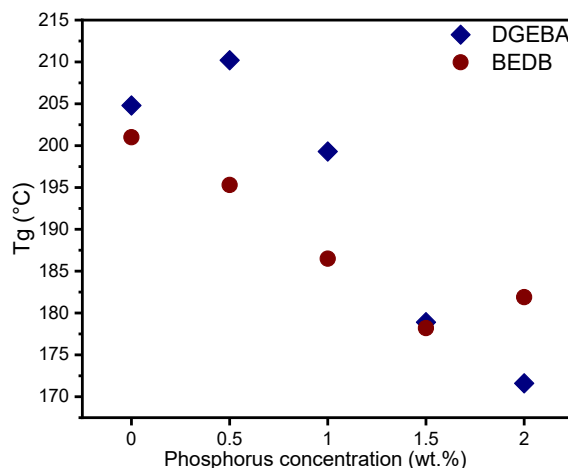
Figure 4.3 Glass transition temperature values measured for DGEBA- and BEDB-based epoxy networks as a function of phosphorus concentration.

Dynamic mechanical analysis (DMA) was also used to measure the thermal properties of DGEBA-based formulations. DMA measures macroscopic mechanical properties at a slow heating rate (3 K min^{-1}), whereas DSC measures the specific heat capacity of a few milligrams of material at a fast-heating rate (10 K min^{-1}). As a result, DMA, a more sensitive tool, was used to validate the glass transition temperatures determined using DSC. Figure 4.4 shows tan delta as a function of temperature for DGEBA-based epoxy formulations and T_g is estimated as the temperature corresponding to the maximum of the tan delta.

The glass transition temperature for DGEBA-based epoxy networks without phosphorus is 212 °C, a slightly higher temperature compared to 205 °C observed using DSC. The inherent differences between DSC and DMA result in a slight variation in T_g. However, a similar trend for glass transition temperatures is observed for DGEBA-based networks containing DMMP where T_g initially increases at 0.5 wt.% of P and decreases at

higher weight percentages of phosphorus, as shown in Table 4.1. These results further confirm the effect of DMMP on the thermal transitions for DGEBA-based epoxy networks.
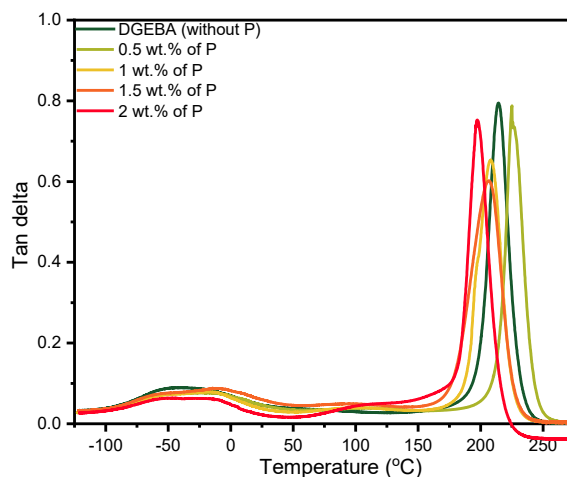
Figure 4.4 Tan delta as a function of temperature measured for DGEBA-based epoxy networks containing DMMP.

	wt.% of P	Glass transition temperature (°C)
	Control	212
	0.5	224
DGEBA	1	208
	1.5	207
	2	197

Table 4.1 Glass transition temperature values measured using DMA for DGEBA-based epoxy networks as a function of phosphorus concentration.

Mechanical fortification of the cured epoxy formulations was investigated using uniaxial compression testing, an advantageous method for high T_g, glassy epoxy networks since it allows evaluation in the high strain regime of the sample, which is inaccessible by tensile testing due to brittle failure resulting from defects in the low strain regime.[185] The elastic modulus values for DGEBA- and BEDB-based formulations without DMMP (in the absence of phosphorus), as shown in Figure 4.5, ranges from 1.6-1.8 GPa. This narrow range indicates that the keto-methylene group of the deoxybenzoin moiety causes no

substantial variations in the stiffness of the cured material relative to the DGEBA-based networks.
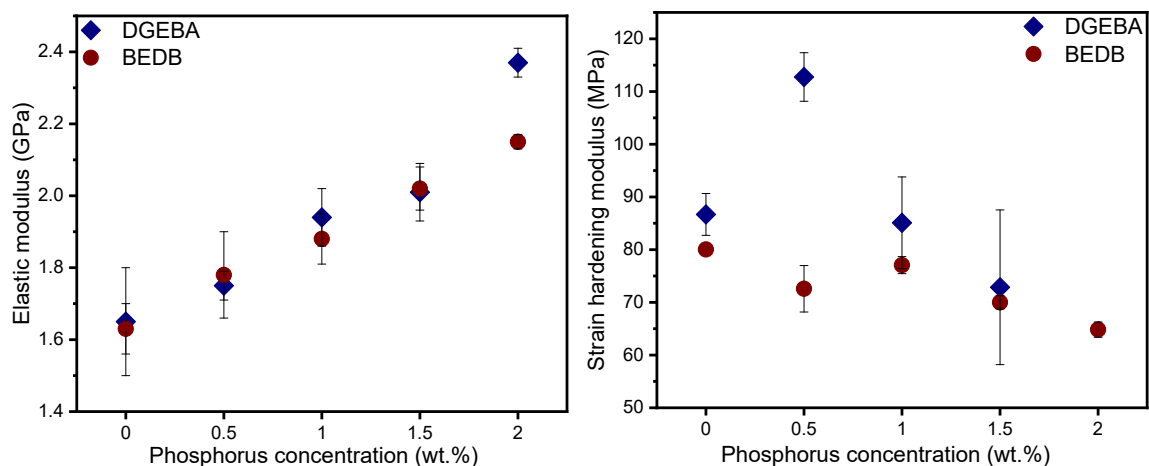
Figure 4.5 The elastic modulus and strain hardening modulus values of DGEBA- and BEDB-containing formulations as a function of phosphorus concentration.

In addition, incorporating DMMP into the network increases the elastic modulus of the cured resins in proportion to the phosphorus concentration. Notably, DGEBA- and BEDB-based formulations at 2 wt.% phosphorus (the maximum concentration investigated) achieve substantially higher elastic modulus values (2.1-2.3 GPa) relative to the networks without DMMP. Typically, this degree of elastic modulus enhancement relies on rigid inorganic fillers or fiber reinforcement;[186, 187] however, improvements in these networks result from added DMMP, which is liquid at room temperature. These results suggest that DMMP facilitates intermolecular interactions within the polymer network which, in turn, provides resistance to deformation.

The T_g of a glassy amorphous material typically scales with yield stress.[185] Interestingly, while thermal analysis shows that DMMP reduces T_g of the cured network, yield stress does not follow similarly, but instead, it is comparable and in some cases higher than the formulations without DMMP (Table 4.2). As yield stress is associated with

113

network stiffness and strength,[188] these results show that DMMP improves the strength of epoxy networks, essentially functioning as a molecular fortifier.

Epoxy networks	wt.% of P	Compression modulus (GPa)	Yield Stress (MPa)	Strain hardening modulus (MPa)
DGEBA	Control	1.65 ± 0.15	130.2 ± 2.6	86.7 ± 4
	0.5	1.75 ± 0.04	133 ± 1.7	113 ± 5
	1	1.94 ± 0.08	133.9 ± 3.3	85 ± 9
	1.5	2.01 ± 0.08	130.8 ± 3.1	73 ± 15
	2	2.37 ± 0.04	130.5 ± 2.4	
BEDB	Control	1.63 ± 0.07	126.3 ± 2.8	80 ± 0
	0.5	1.78 ± 0.12	129.2 ± 5.3	73 ± 4
	1	1.88 ± 0.07	125 ± 4.1	77 ± 2
	1.5	2.02 ± 0.06	133 ± 1.9	70 ± 1
	2	2.15 ± 0.02	134.4 ± 2.8	65 ± 1

Table 4.2 Mechanical properties evaluated using compression testing for DGEBA- and BEDB-containing formulations as a function of phosphorus concentration.

One advantage of compression testing is its ability to probe the high strain regime (post-yield response) of glassy epoxies and thereby evaluate the strain hardening modulus. Figure 4.5 shows that the strain hardening modulus decreases with increasing phosphorus concentration for both DGEBA and BEDB formulations. Notably, the DGEBA formulation containing 0.5 weight percent phosphorus shows greater strain hardening modulus as well as higher T_g, possibly a result of efficient epoxy curing facilitated *via* a lower process viscosity. On the contrary, at higher phosphorus concentrations, both the strain hardening modulus and T_g decreases for the DGEBA-based formulations. While lower T_g values are typically attributed to plasticization, prior studies showed that strain hardening modulus depends on network connectivity and scales with crosslinking density, independent of backbone architecture.[185, 189] Thus, lower crosslinking densities may arise from covalent integration of DMMP into the network, which is plausible under the curing conditions and supported by NMR spectroscopy (vide infra), resulting in networks with unreacted epoxide or amine. Such a disentangled network with free chain-ends or chain

extended network would lead to increased free volume in the network and disrupt network connectivity, resulting in lower T_g and strain hardening modulus values compared to networks without DMMP.

Building on recent advances in the spectroscopic characterization of polymer-additive interactions (*e.g.,* hydrogen bonding and ion pair formation),[177, 190] we employed solid state nuclear magnetic resonance (ssNMR) spectroscopy to characterize the networks. In the ^{31}P ssNMR spectrum of a DGEBA-network, shown in Figure 4.6-(a), two resonances are noted: a strong, broad signal at 34.4 ppm and a weak signal at 51.0 ppm (the remaining signals are attributed to spinning side bands). The ^{31}P ssNMR spectrum of the cured BEDB network appeared similarly (Figure 4.6-(b)).
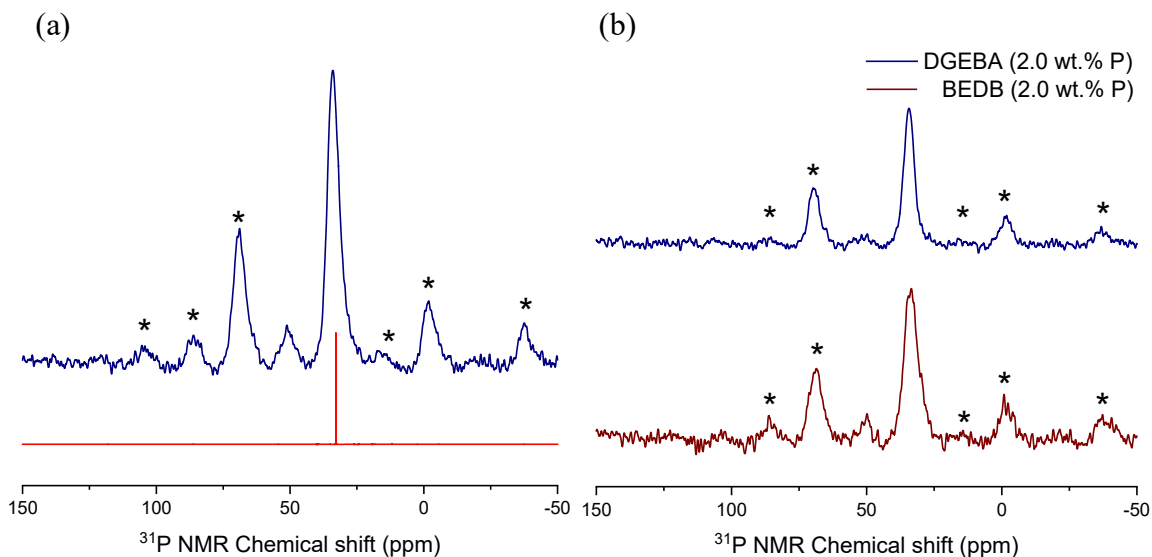
Figure 4.6 a) Solid-state ^{31}P NMR spectrum of a DGEBA-cured resin containing phosphorus with peaks at 34.4 and 51.0 ppm (all other peaks are spinning sidebands, denoted by asterisks) (blue, broad signal). Solution-state ^{31}P NMR spectrum of DMMP in DMSO-d_6 (red, sharp signal). b) Solid-state ^{31}P NMR spectrum of a DGEBA-cured and BEDB-cured resin containing phosphorus.

These spectra confirm the integration of phosphorus-containing compounds into the epoxy networks, despite employing a post-curing heating step that is 40 °C above the

boiling point of DMMP. The exact chemical structures responsible for these phosphorus resonances are unknown. It is tempting to assign the signal at 34.4 ppm to unreacted DMMP that is physically entrapped in the epoxy matrix, since its ppm value is close to that of DMMP in solution (32.9 ppm), and Brunklaus and coworkers attributed a ^{31}P ssNMR resonance at 33.1 ppm to residual DMMP in an aliphatic epoxy network. However, in our spectra, the signal breadth and shape of the spinning sidebands, typical of ssNMR and the chemical shift anisotropy that arises from orientation-dependent nuclear magnetic interactions of rigid segments, suggests covalent integration of phosphorus into the cured networks.
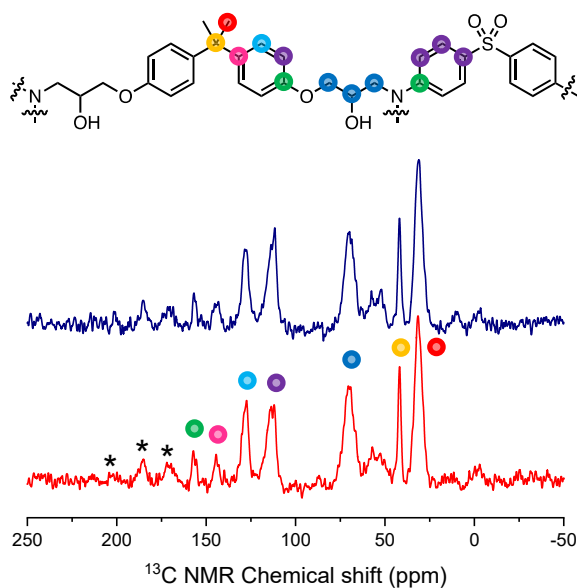
Figure 4.7 Solid-state ^{13}C NMR spectrum of the DGEBA-based network with 2 wt.% phosphorus (blue) and without organophosphorus additive (red) (asterisks denote spinning sidebands).

Fixing phosphorus into the network covalently may occur by several mechanisms, including a nucleophilic attack of amines and alkoxides at the phosphorus of DMMP; a peak position of ~34 ppm suggests the product of alkoxide based substitution on known small molecules with the corresponding P-O and P-N bonds.[191-193] The ^{31}P signal at 51.0

ppm generally corresponds to a structure in which an R-group (alkyl or aromatic) replaced one OCH$_3$ group of DMMP;[194] while conventional mechanisms to account for such a product are non-obvious, long heating times in the solid state may produce minor products of this type. In the ^{13}C NMR spectra (Figure 4.7), the lack of sharp signals for the methyl (8-10 ppm) and methoxy (52 ppm) groups further suggests an absence of physically entrapped DMMP, while the broad signals in similar peak positions indicate the presence of P(O)-OCH$_3$ and P(O)-CH$_3$ species (*i.e.,* rather than DMMP itself).

4.3.3   Heat release and flammability properties of DMMP-containing epoxy networks

The cured DGEBA and BEDB epoxy resins were characterized for their thermal and heat release properties by several methods, starting with thermogravimetric analysis (TGA) to evaluate thermal degradation properties, with a clear influence of DMMP apparent from the data in Figure 4.8.
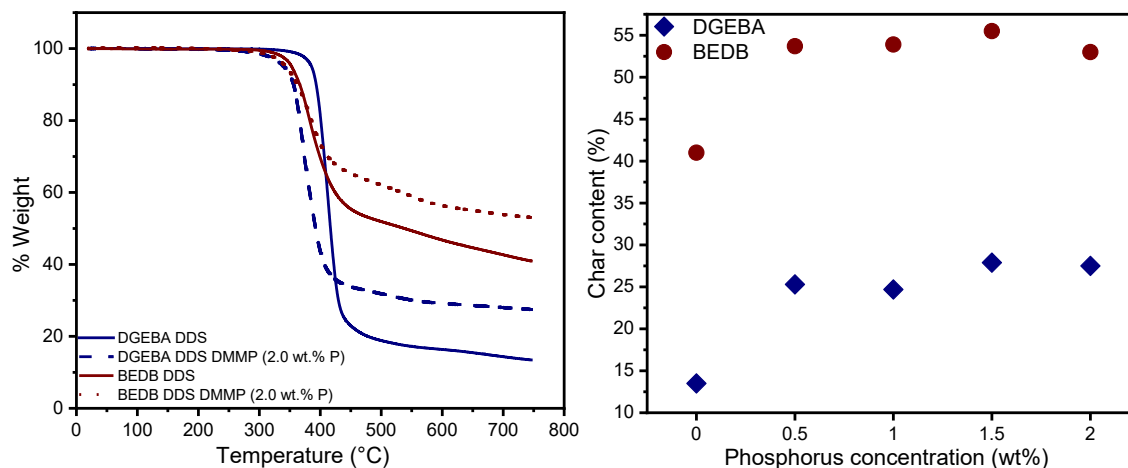
Figure 4.8 a) TGA thermograms of DGEBA and BEDB cured epoxies and networks containing 2 weight percent phosphorus; b) char residue, determined by TGA at 700 °C, for phosphorus containing DGEBA and BEDB formulations.

The DGEBA-based network prepared with 2 weight percent phosphorus produces a char residue of 27%, an impressive two-fold increase over the network prepared without

DMMP (12%). Remarkably, replacing DGEBA with BEDB, also with 2 weight percent phosphorus, produces a network with a char residue of 55%, an exceptionally high value for organic polymers and markedly higher than BEDB networks without phosphorus (42%). Such high char residues correlate with low heat release properties, due to a reduced propensity of volatiles to escape the charring network during decomposition. The inclusion of DMMP appears to aid in char formation, even at only 0.5 weight percent phosphorus; with greater phosphorus concentration, the char residue plateaus.

DMMP also influences the kinetics of network degradation, as observed by the slower degradation rate of DMMP-containing networks relative to formulations without DMMP (Figure 4.9). The DGEBA- and BEDB-based networks exhibit a single-step degradation process with the onset of degradation at ~350 °C in the absence of phosphorus. The degradation temperature of these epoxy networks decreases with the increasing concentration of phosphorus (Appendix Figure A4.1), resulting in up to 50 °C decrease in the onset of degradation for DGEBA- and BEDB-based networks containing 2 weight percent phosphorus. Notably, the 300 °C degradation temperature of these formulations, well above the boiling point of DMMP (180 °C), suggests that strong DMMP-matrix interactions prevent volatilization of the additive.
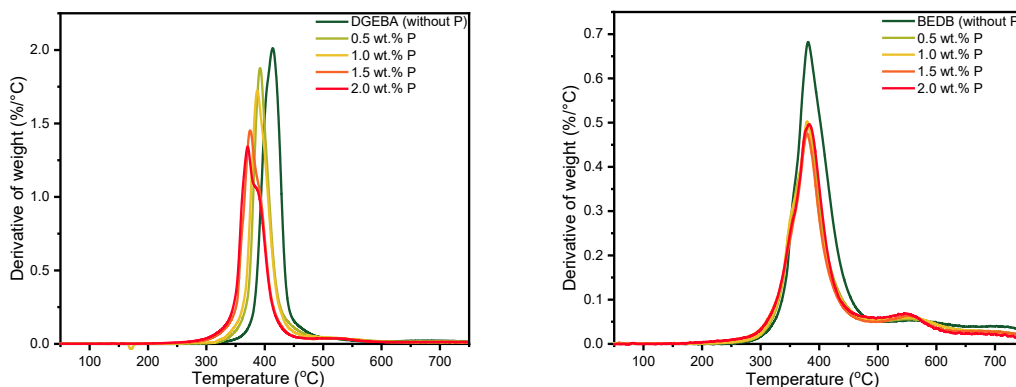
Figure 4.9 Derivative weight percent of DMMP-containing epoxy formulations obtained by thermogravimetric analysis (TGA).

Additionally, the incorporation of DMMP in these epoxy networks reduces the degradation rate while simultaneously achieving higher char content. For example, the maximum rate of degradation for DGEBA-based networks decreases from 2 %/°C in the absence of phosphorus to 1.3 %/°C in the presence of 2 weight percent phosphorus, whereas for BEBD-based network degradation rate reduces from 0.7 %/°C to 0.45 %/°C with the incorporation of 2 weight percent phosphorus. Further, BEDB-based networks also demonstrate lower rates of degradation compared with DGEBA-based networks. The maximum rate of degradation denotes the maximum possible material degraded at peak degradation temperature and acts as an indicator of heat released during the process. Therefore, a significant reduction in the rate of degradation for DGEBA- and BEDB-based networks in the presence of phosphorus suggests improved heat release properties.

Further, a kinetic study was performed following the ASTM standard E1641 to determine the thermal degradation activation energy of these epoxy networks.[195] Decomposition curves for epoxy networks were evaluated using TGA at different heating rates including 1 K min^{-1}, 2.5 K min^{-1}, 5 K min^{-1}, and 10 K min^{-1}, as shown in Figure 4.10. This test method assumes a general form of degradation equation (Equation 4.1) which is solved using the method of Ozawa, Flynn, and Wall to obtain Equation 4.2. Solving this equation using an iterative method provides activation energy of degradation. Figure 4.11 shows the thermal degradation activation energy barrier for increasing conversion rates.

Equation 4.1: $\dfrac{da}{dT} = \dfrac{A(1-\alpha)}{\beta} e^{\left[-\frac{E}{RT}\right]}$

Equation 4.2: $E = -\left(\dfrac{R}{b}\right)\dfrac{\Delta log\beta}{\Delta\left(^1/_T\right)}$
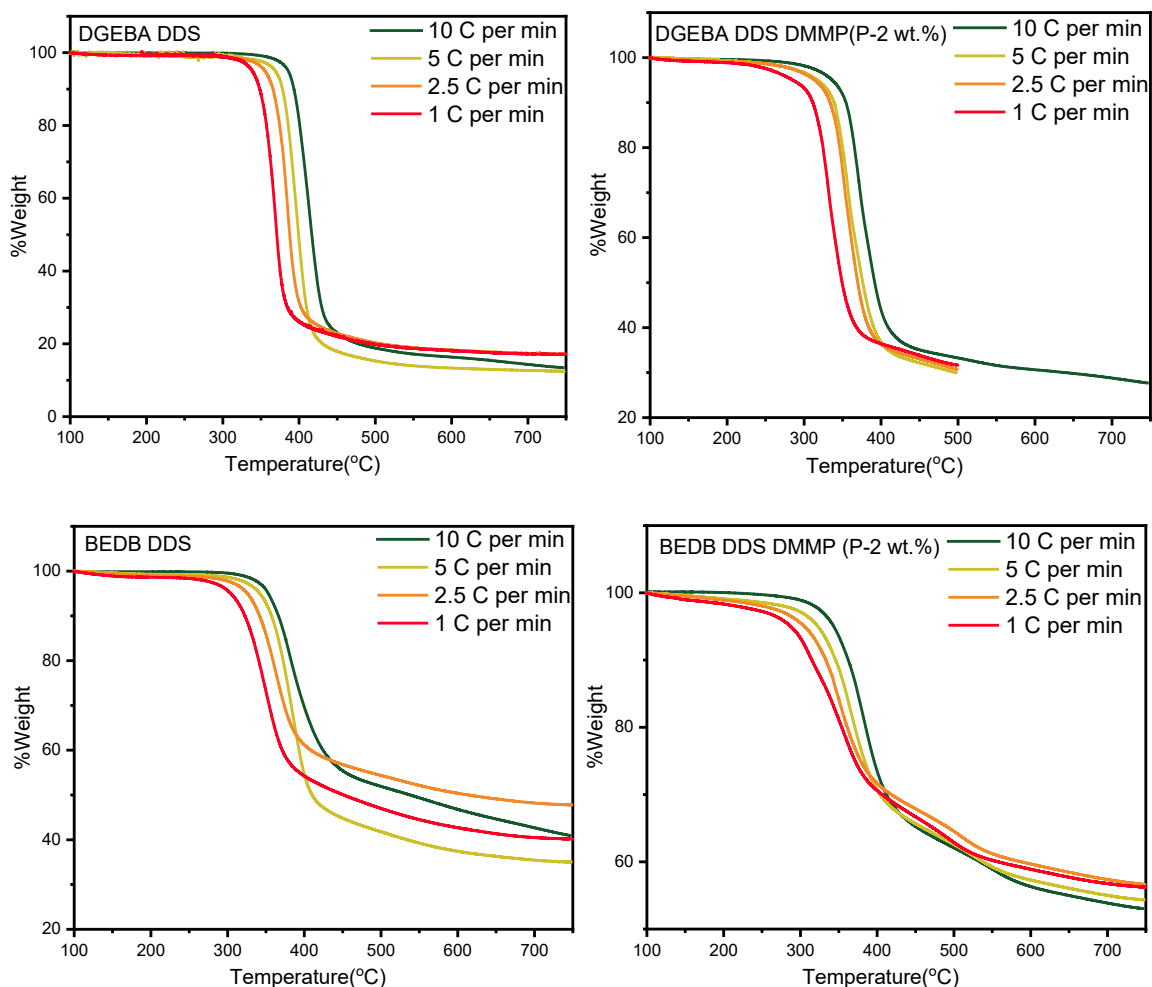
Figure 4.10 Decomposition curves at different heating rate for DGEBA- and BEDB-based epoxy networks obtained by thermogravimetric analysis (TGA).

The degradation activation energy for DGEBA and BEDB networks without DMMP is higher in comparison with DGEBA and BEDB networks containing 2 weight percent phosphorus during the initial conversion. However, at higher degrees of conversion, the energy barrier for degradation for DMMP-containing networks is higher in comparison with networks without DMMP. Volatilization of unbound DMMP and lower bond energy for P-C bond results in an earlier onset of degradation for networks containing DMMP.[196] However, a char layer formed on the surface of the material during the degradation increases the barrier for thermal degradation and provides resistance against

further degradation of the underlying material. As a result, when a sufficient char layer is formed, the activation energy for networks containing DMMP becomes higher than for networks without DMMP. Such transition occurs for deoxybenzoin-based networks at 15 % conversion, whereas for bisphenol A-based networks at 50 % conversion. These results suggest that the efficient char formation of BEDB networks coupled with the flame retardance mechanisms of DMMP offers pronounced resistance for thermal degradation, even at the initial stages of degradation.
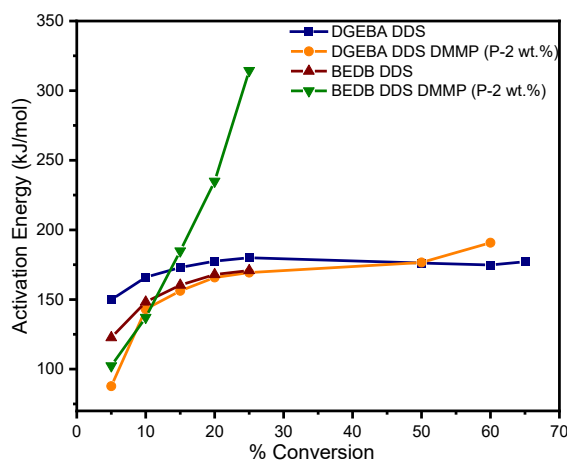
Figure 4.11 Degradation activation energy for DGEBA- and BEDB-based epoxy networks determined using Ozawa, Flynn, and Wall method.

MCC evaluations were performed on the epoxy formulations to obtain heat release profiles, with representative heat release rate (HRR) curves shown in Figure 4.12. MCC is an oxygen consumption calorimetry technique performed on milligram scale samples that provides heat release data used to calculate valuable flammability parameters, such as heat release capacity (HRC) and fire growth capacity (FGC).[197, 198] The peak heat release rate (pHRR), an indicator of the maximum possible heat release during combustion, for the DGEBA epoxy formulation was 445 W g^{-1} without phosphorus and 300 W g^{-1} with 2 weight percent phosphorus additive. Impressively, the BEDB networks have pHRR values

of 225 W g^{-1} and with the introduction of 2 weight percent phosphorus reduces pHRR to only 116 W g^{-1}.
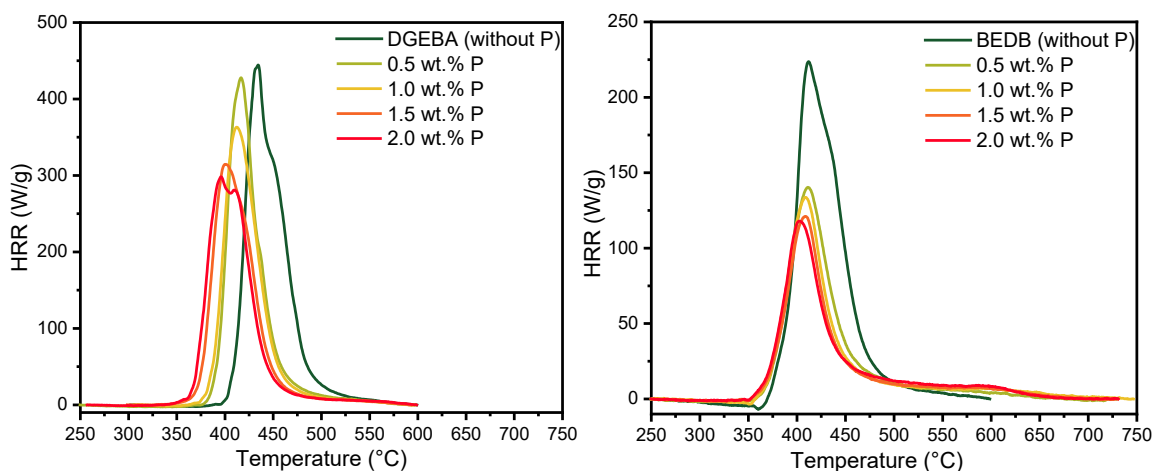
Figure 4.12 Heat release rate profiles of a) DGEBA and b) BEDB epoxy networks with and without the organophosphorus additive DMMP.

MCC measurements revealed that both the HRC (calculated by dividing the peak heat release by the heating rate) and the total heat release (THR as defined as the area under the heat release profile) decreases significantly in the presence of DMMP. In general, these small-scale MCC measurements correlate well with parameters obtained from large-scale (> 100 gram) fire tests, such as cone calorimetry and the limiting oxygen index test.[197] These significantly lower HRC and THR values suggest a potential reduction in the flammability of materials prepared from these epoxy polymers. Figure 4.13 illustrates that by replacing DGEBA with BEDB, the HRC of the resultant networks decreases by 60%, from 600 J g^{-1} K^{-1} to 220 J g^{-1} K^{-1}. The HRC and THR are reduced even further (an additional 40-50%) by incorporating 2 weight percent phosphorus into the epoxy formulations. Interestingly, the HRC of conventional DGEBA networks decreases to 300 J g^{-1} K^{-1} with 2 weight percent phosphorus, 50% lower than the phosphorus-free networks. Notably, the BEDB-based formulation containing 2 weight percent phosphorus reveals an impressively low HRC of 119 J g^{-1} K^{-1} and a THR of 7.2 kJ g^{-1}. Such exceptionally low

heat release values place these epoxy networks into an exclusive category of inherently flame retardant polymers, such as poly(phenyleneethersulfone) (PESU) (115 J g^{-1} K^{-1}) and polyetherketoneketone (PEKK) (96 J g^{-1} K^{-1}).[199]
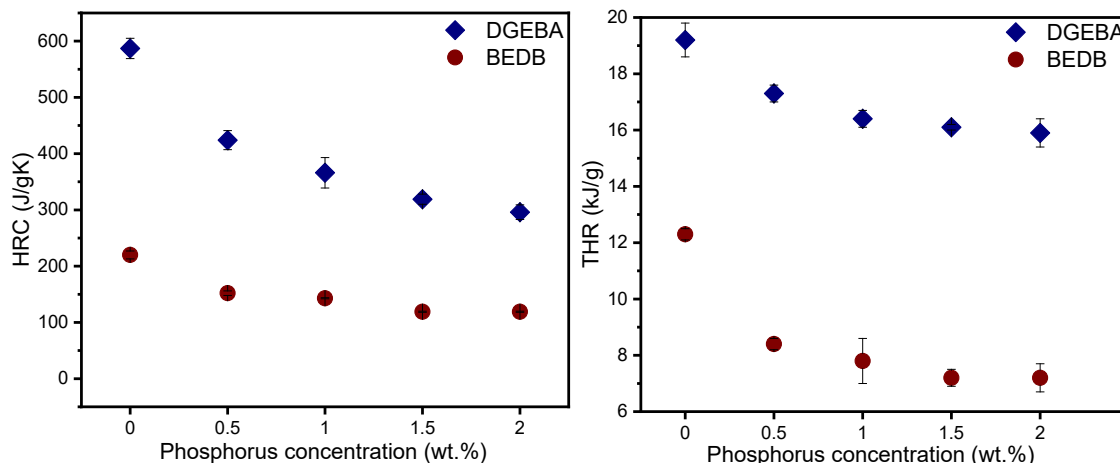
Figure 4.13 a) Heat release capacity and b) total heat release, determined by MCC, for all epoxy networks as a function of increasing phosphorus concentration.

Interestingly, the reduction in heat release properties of the DMMP-containing epoxy formulations coincided with lower ignition temperatures, which are more significant for the DGEBA-based networks (~50 °C reduction) than for BEDB-based networks (~20 °C reduction). Recently, Lyon and coworkers developed a new flammability parameter, termed fire growth capacity (FGC), which takes into account variations in ignition temperature as well as the temperature range over which heat is released during combustion, culminating in a better assessment of the potential for a material to contribute to fire growth.[200, 201] The FGC, calculated as per Equation 4.3, utilizes values obtained from MCC and takes into account the ignition capacity based on T_1 (the temperature when 5% of the combustion heat is released), T_2 (the temperature when 95% of the combustion heat is released), and Q_∞, the heat release capacity when T_0 is the testing temperature.

Equation 4.3: $FGC = \left(\frac{Q_\infty}{T_2 - T_1}\right)\left(\frac{T_2 - T_0}{T_1 - T_0}\right)$

The calculated FGC (Table 4.3) of 384 J g^{-1} K^{-1} for the DGEBA-based epoxy formulation drops to 273 J g^{-1} K^{-1} for the formulation containing 2 weight percent phosphorus. Notably, replacing DGEBA with BEDB lowers the FGC to 194 J g^{-1} K^{-1}, which decreases even further, to only 56 J g^{-1} K^{-1}, in the BEDB formulation containing 2 weight percent phosphorus. Interestingly, the FGC gradually decreases with increasing phosphorus concentration for DGEBA-based networks; however, the FGC of deoxybenzoin-based networks decreases very significantly with only 0.5 wt.% phosphorus concentration. Thus, owing to the benefit of this phosphorus additive, epoxy networks with impressively low FGC values can now be classified among inherently flame-retardant polymers, such as polyamideimide (25 J g^{-1} K^{-1}) and polyetherimide (110 J g^{-1} K^{-1}).[202]

	wt.% of P	HRC (J/g-K)	THR (kJ/g)	FGC (J/g-K)
DGEBA	Control	587 ± 18	19.2 ± 0.6	384 ± 11
	0.5	424 ± 17	17.3 ± 0.3	351 ± 05
	1	366 ± 27	16.4 ± 0.3	311 ± 11
	1.5	319 ± 9	16.1 ± 0.1	286 ± 06
	2	296 ± 13	15.9 ± 0.5	273 ± 09
BEDB	Control	220 ± 7	12.3 ± 0.2	194 ± 1
	0.5	152 ± 4	8.4 ± 0.2	76 ± 1
	1	143 ± 1	7.8 ± 0.8	65 ± 4
	1.5	119 ± 1	7.2 ± 0.3	56 ± 0
	2	119 ± 1	7.2 ± 0.5	56 ± 2

Table 4.3 Heat release capacity (HRC), Total heat release (THR), and Fire growth capacity (FGC) for DMMP-containing DGEBA and BEDB formulations

In accord with TGA and MCC results, vertical burn tests performed (conducted similarly to a conventional UL-94 vertical burn test but in the ambient atmosphere and with propane as the fuel) on the DMMP-containing BEDB networks exhibits self-extinguishing properties (Table 4.4).

	After flame 1(s)	After flame 2 (s)	Dripping	UL-94 Rating
DGEBA Control	-	-	Yes	NR
DGEBA + DMMP (P-2 wt.%)	23	20	No	V-1
BEDB Control	14	14	No	V-1
BEDB + DMMP (P-2 wt.%)	3	10	No	V-0

Table 4.4 Vertical burn results for DMMP-containing DGEBA and BEDB networks

Vertical burn tests allow for observation of flame propagation and melt dripping, which is inaccessible by TGA and MCC, as well as for evaluating polymers based on the time required for the flame to self-extinguish in categories ranging from effective flame retardant, to moderately flame retardant, to highly flammable.[203] For example, DGEBA-cured resins containing 2 wt.% phosphorus self-extinguishes in 20 seconds, whereas DGEBA specimens without DMMP burn entirely to the clamp and drip excessively (Figure 4.14). Replacing DGEBA with BEDB, without phosphorus, produced cured resins that self-extinguishes in 14 seconds. Even more impressively, BEDB resins containing 2 weight percent phosphorus self-extinguishes in ~7 seconds, on average, demonstrating excellent flame retardant properties that we anticipate to be attractive for many applications requiring epoxy adhesives.

(a) DGEBA +DDS

(b) DGEBA +DDS+ DMMP (P-2%)

(c) BEDB +DDS

(d) BEDB +DDS+ DMMP (P-2%)

(e)
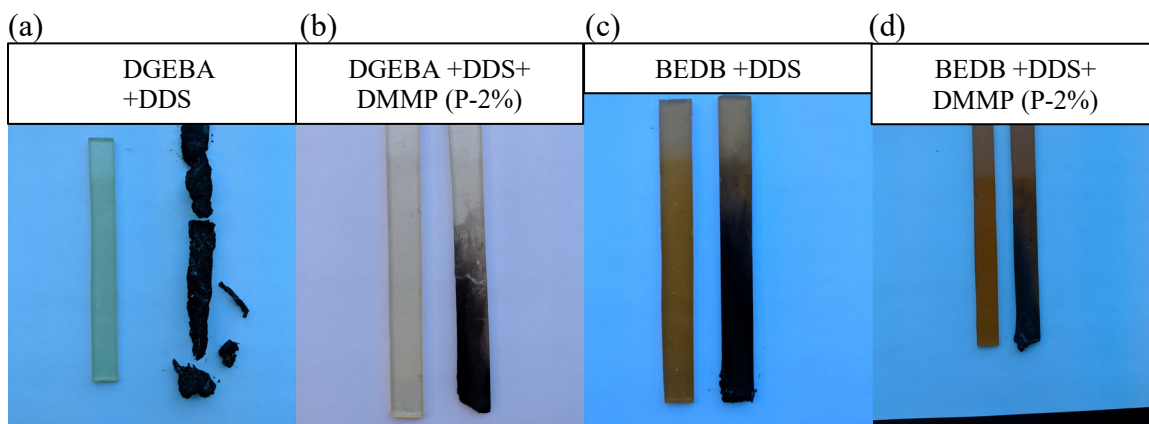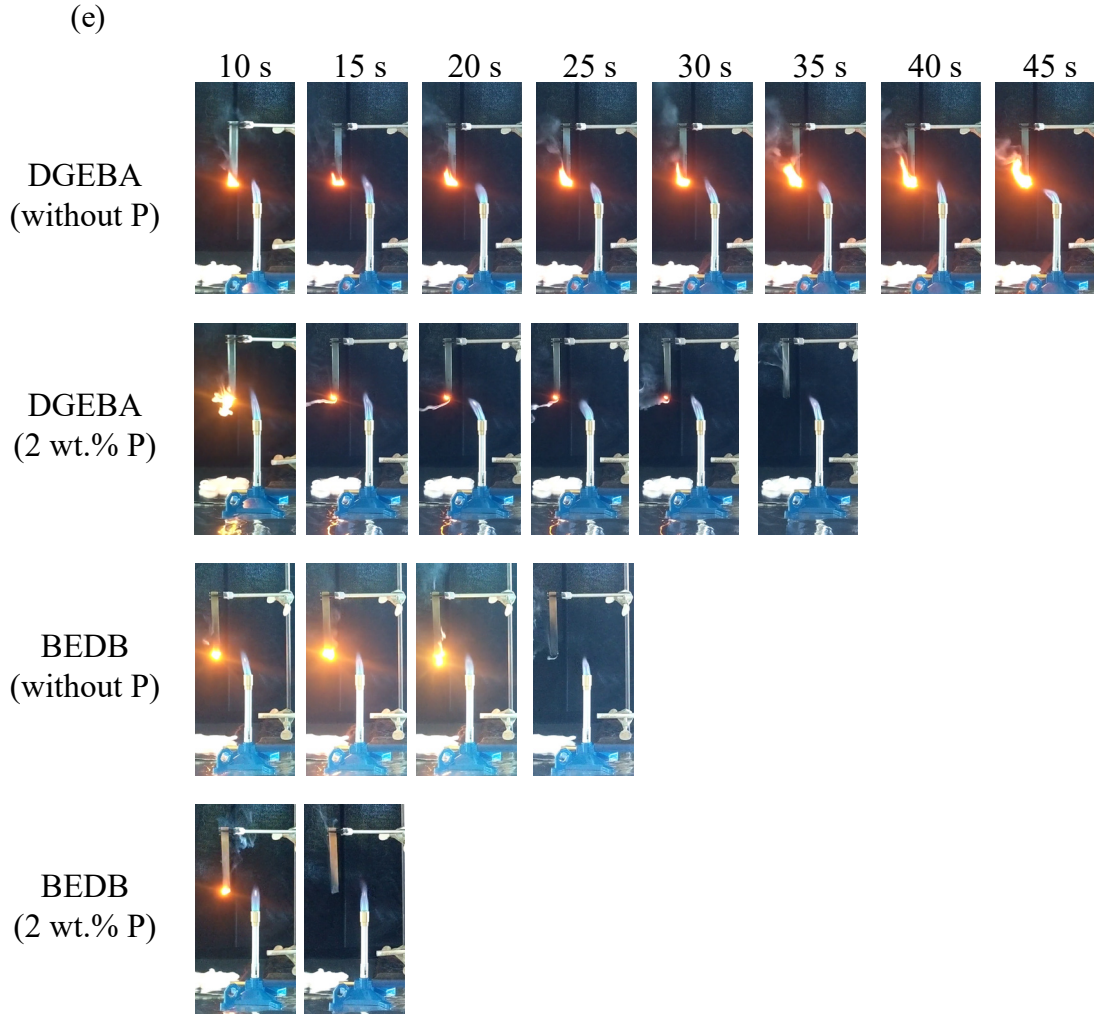
Figure 4.14 Photos of epoxy specimens before vertical burn testing (left) and after (right) of a) DGEBA without phosphorus, b) DGEBA containing 2 wt.% phosphorus, c) BEDB without phosphorus, and d) BEDB with 2 wt.% phosphorus e) Evolution of burning for the epoxy formulations with and without phosphorus.

After the vertical burn tests were completed, the morphology of the charred samples was analyzed by scanning electron microscopy (SEM) (Figure 4.15). Char residue from samples without DMMP appears smooth and homogeneous, while char from the DMMP-containing formulations displays porous, foam-like surface structures. The pore diameters for DGEBA resins containing 2 weight percent phosphorus ranges from 50 to 100 μm, while the deoxybenzoin resins exhibit a broader pore size distribution, from 5 to 300 μm.
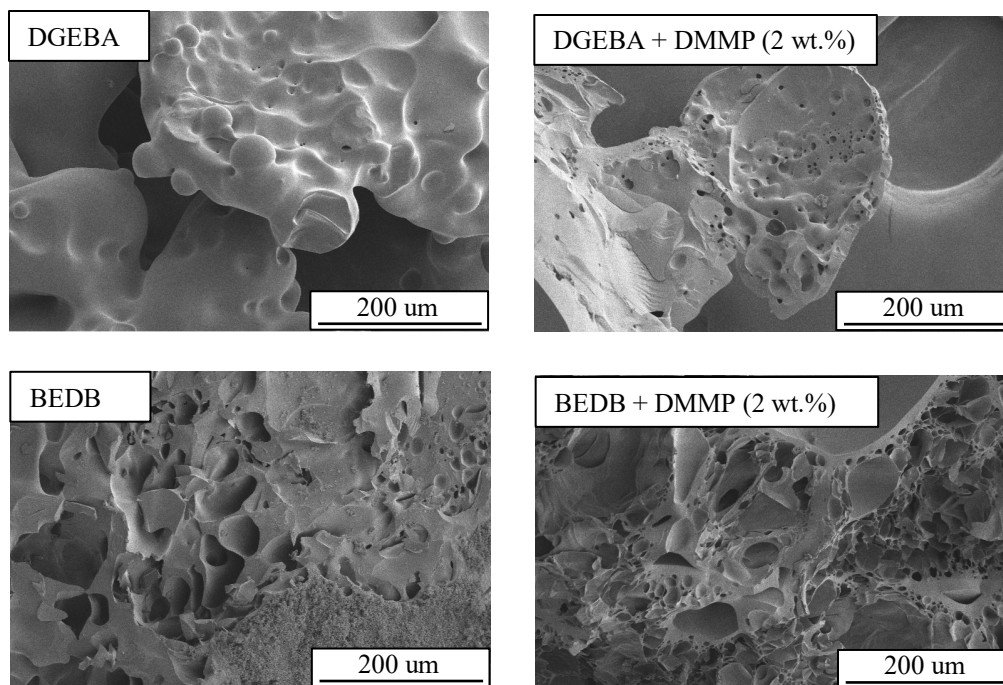
Figure 4.15 SEM images of the char formed after the vertical burn testing of (a) DGEBA-based epoxy, (b) BEDB-based epoxy, (c) DGEBA with DMMP (2 wt.% phosphorus), and (d) BEDB with DMMP (2 wt.% phosphorus) formulations.

The porous surface observed may result from gas evolution during combustion, which allows polymer at the combustion surface to flow and gaseous products to release.[204-206] Organophosphorus flame retardants are known to act in the gas phase by forming phosphorus oxide radicals (P-O•) during decomposition that quench reactive hydroxyl and hydrogen radicals to form inert gases.[206] To further elucidate the role of DMMP during thermal degradation, the DGEBA network containing 2 weight percent phosphorus was degraded completely by heating to 700 °C in a nitrogen atmosphere and the char residue was collected. Solid-state ^{31}P NMR spectroscopy performed on the collected residue revealed the absence of phosphorus in the char (Figure 4.16), suggesting the release of P-containing compounds into the vapor phase during thermal degradation.
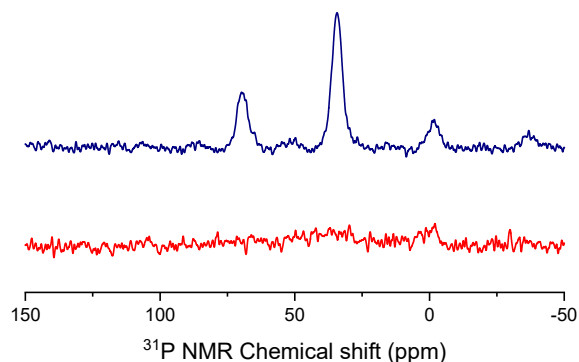
Figure 4.16 Solid-state ^{31}P NMR spectra of DGEBA-based formulation containing 2 wt% phosphorus (blue) and char residue after complete degradation by TGA (red).

Thus, the combined effect of gas-phase flame inhibition and improved char formation results in the superior flame-retardant performance of DMMP-containing thermosets, significantly minimizing the flammability of these epoxy resins.

4.3.4 Thermal and mechanical properties of organophosphorus additive-containing aliphatic epoxy networks

Bisphenol A-based aliphatic epoxy networks containing DMMP, even at a modest 10 phr concentration, demonstrate improved mechanical and heat release properties.[172] However, there remain opportunities to investigate flame retardant properties of deoxybenzoin-based aliphatic epoxy networks containing DMMP for a possible synergism. Additionally, non-toxic and eco-friendly 9,10-dihydro-9-oxa-10-phosphaphenanthrene-10-oxide (DOPO) has received a lot of attention from the scientific community for its effectiveness as a flame retardant additive, but its ability to act as a fortifier remains untested.[207, 208] Therefore, mechanical and heat release properties of aliphatic epoxy networks containing DMMP or DOPO or a combination of DMMP and DOPO are studied. Epoxy resins were prepared from bisphenol A- and deoxybenzoin-based epoxy monomers with a stoichiometric equivalent amount of aliphatic polyetheramine Jeffamine D-230 (D230). Epoxy formulations were prepared using 10 phr of DMMP or DOPO, and also,

128

using 17.5 phr DOPO that results in wt.% of P as that of 10 phr DMMP. These epoxy networks were characterized using non-standard compression testing, microscale combustion calorimetry (MCC), and thermogravimetric analysis (TGA).

Thermal properties of these formulated epoxy resins were determined using a differential scanning calorimetry (DSC). Glass transition temperatures evaluated using DSC have been tabulated in Table 4.5. The aliphatic DGEBA-based networks possess a higher T_g of 89 °C compared to the T_g of 78 °C for BEDB-based resins. BEDB is a solid at room temperature with a melting point of 130 °C and therefore, requires a higher mixing temperature of 130 °C. Under these processing conditions, aliphatic D230 rapidly reacts with the epoxide functionalities and forms a crosslinked network with unreacted epoxide chain ends, resulting in lower glass transition temperatures. In the case of DGEBA-based networks, DMMP and DOPO acts as a plasticizer and reduces the glass transition temperatures to 72 °C and 86 °C, respectively. Interestingly, for BEDB-based epoxy networks, DMMP lowers the T_g, however, incorporation of DOPO increases the T_g. DOPO is a semi-crystalline solid at room temperature with a melting point of 120 °C, and it reacts with the epoxide functionality at high processing temperatures.[155] Mixing BEDB-based epoxy resins with DOPO and D230 at 130 °C results in several side reactions and leads to a higher T_g.

Epoxy networks	Additive	Glass transition temperature (°C)
DGEBA	Control	89
	10 phr DMMP	72
	10 phr DOPO	86
BEDB	Control	78
	10 phr DMMP	72
	10 phr DOPO	89

Table 4.5 Glass transition temperature values measured using DSC for aliphatic DGEBA- and BEDB-based epoxy networks containing DMMP and DOPO.

Mechanical fortification of these epoxy formulations was investigated using non-standard compression testing. Figure 4.17 shows representative stress-strain curves recorded during the compression testing and utilized to determine yield stress, elastic modulus, and strain hardening modulus of these networks.
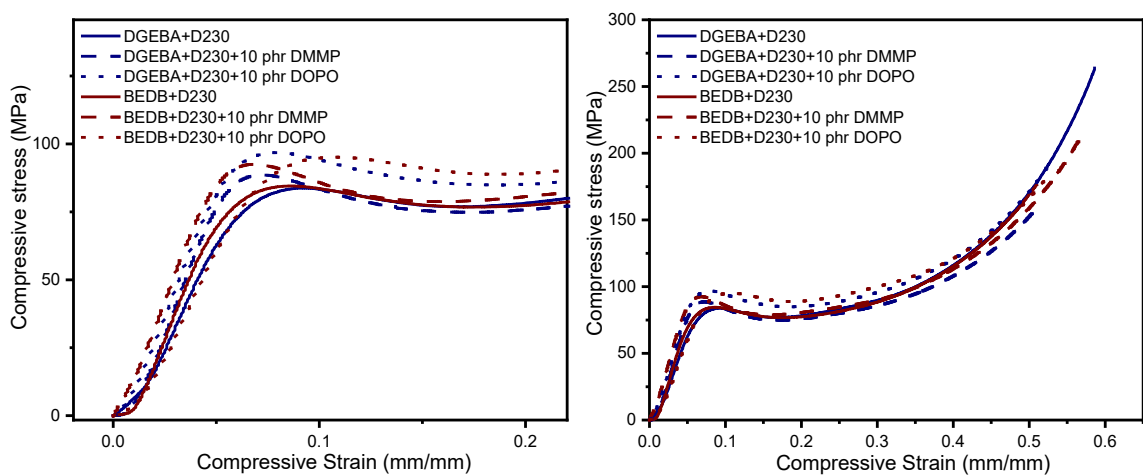
Figure 4.17 Stress-strain plots for DGEBA- and BEDB-based aliphatic epoxy networks containing DMMP and DOPO.

The control aliphatic DGEBA- and BEDB-based epoxy networks exhibit elastic modulus in the range of 1.5-1.8 GPa and yield stress of ~84 MPa. Similar strength and stiffness of both networks further emphasize that the keto-methylene linkage in the deoxybenzoin moiety does not contribute towards mechanical properties. Notably, incorporating DMMP substantially improves the stiffness as well as yield stress for these epoxy networks, as tabulated in Table 4.5. DMMP facilitates enhanced intermolecular interactions and thereby, achieves superior linear elastic properties. Additionally, DOPO shows characteristics of a fortifier for DGEBA-based networks and improves the elastic modulus and yield stress. Interestingly, adding DOPO reduces the modulus for BEDB-based networks. There is a possible side reaction between DOPO and BEDB epoxy monomer that can occur at a higher mixing temperature and result in the formation of a fragmented epoxy network.[155] Such fragmented networks exhibit lower stiffness. DMMP

130

and DOPO also increase the density of epoxy networks. These results suggest that DMMP and DOPO fortify the DGEBA- and BEDB-based epoxy networks.

Epoxy networks	Additive	Compression modulus (GPa)	Yield Stress (MPa)	Strain hardening modulus (MPa)	Density (g/cc)
DGEBA	Control	1.5	83.6	538	1.15
	10 phr DMMP	1.9	88.3	421	1.18
	10 phr DOPO	1.9	86.1	494	1.24
BEDB	Control	1.8	84.8	500	1.23
	10 phr DMMP	2.1	92	451	1.23
	10 phr DOPO	1.6	94.9	472	1.3

Table 4.6 Mechanical properties measured using non-standard compression testing for aliphatic DGEBA and BEDB formulations containing DMMP and DOPO.

In addition to linear elastic properties, non-standard compression testing allows probing high strain non-linear mechanical response. Incorporating DMMP and DOPO reduces the strain hardening modulus for both the DGEBA- and BEDB-based epoxy networks, as indicated in Table 4.6. Strain hardening modulus depends on the network connectivity and crosslink density. DMMP and DOPO influence the curing kinetics and, in the case of BEDB, can even get covalently integrated into the network *via* grafting. This results in lower crosslink densities for fortified epoxy networks.

4.3.5 Heat release and flammability properties of organophosphorus additive-containing aliphatic epoxy networks

Figure 4.18 shows the derivative of weight loss as a function of temperature for bisphenol A- and deoxybenzoin-based epoxy resins containing organophosphorus additives. Bisphenol A-based epoxy networks have a higher rate of degradation in comparison with the deoxybenzoin-based epoxy networks, a similar trend as that of aromatic epoxy networks. Further, deoxybenzoin-based epoxy monomers lead to a superior

char formation. For example, deoxybenzoin-based aliphatic epoxy networks demonstrate higher char content (27 wt.%) than DGEBA-based aliphatic (8 wt.%) and aromatic (12.5 wt.%) networks. DMMP and DOPO decrease the rate of degradation and lower the onset of degradation temperature for both networks.
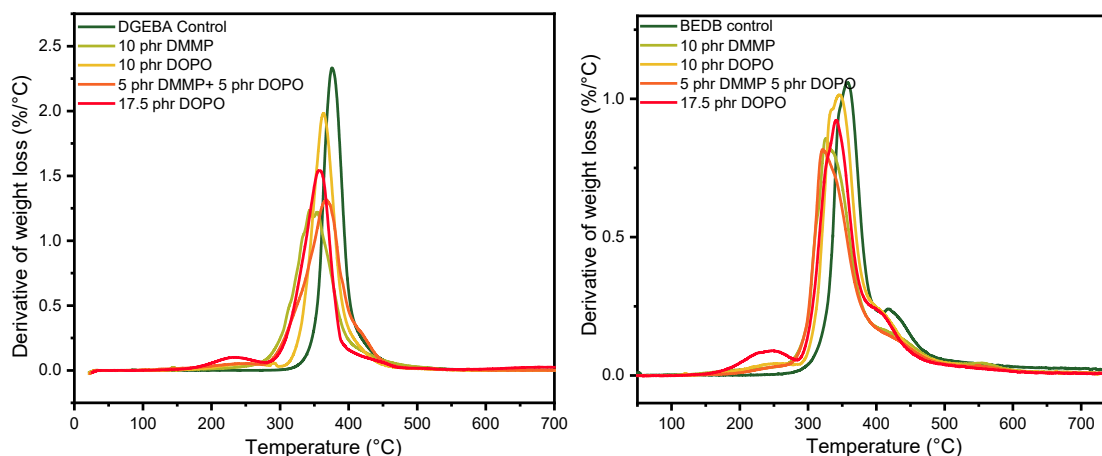
Figure 4.18 Derivative weight percent of DMMP and DOPO-containing aliphatic epoxy formulations obtained by thermogravimetric analysis (TGA).

For DGEBA networks, the rate of degradation reduces from 2.3 %/°C to 1.2 %/°C and 2 %/°C with the incorporation of 10 phr DMMP and 10 phr DOPO, respectively. Even in the case of deoxybenzoin-based epoxy networks, DMMP results in a more significant decrease in the rate of degradation in comparison with DOPO. Epoxy networks containing 10 phr DMMP achieve a lower maximum rate of degradation when compared with networks containing 17.5 phr DOPO where phosphorus concentration is similar. DMMP, when present, minimizes fuel generation and reduces the rate of degradation. As a result, networks containing only DMMP or a combination of DMMP and DOPO exhibit a similar rate of degradation. Interestingly, the char content of epoxy networks remains similar even after the incorporation of DMMP or DOPO, in contrast with aromatic epoxy networks. These results suggest that the linear backbone of aliphatic networks is more susceptible to

degradation, especially in the absence of aromatic sulfone-containing amines which contributes to the polyaromatic char formation.[162]

Microscale combustion calorimetry (MCC) was another technique implemented to evaluate the flammability characteristics of aliphatic epoxy networks. Figure 4.19 shows the heat release rate profiles for DGEBA- and BEDB-based epoxy networks which were fitted with asymmetric Gaussian distribution to determine the heat release capacity (HRC) and total heat release (THR).
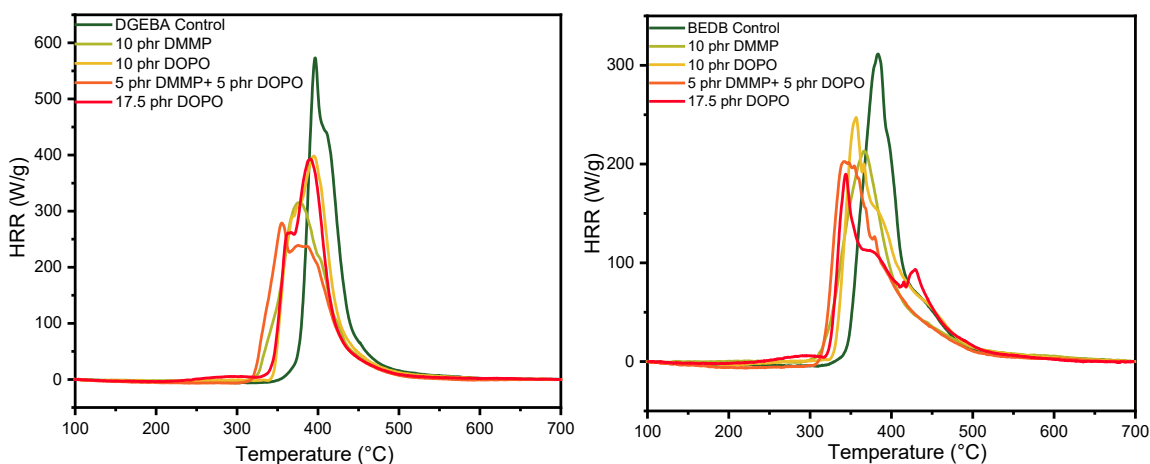
Figure 4.19 Heat release rate profiles of a) DGEBA and b) BEDB aliphatic epoxy networks containing DMMP and DOPO.

The peak heat release rate (pHRR) indicates the maximum heat released during the combustion. The control DGEBA networks exhibit the pHRR of 565 W g^{-1}, whereas control BEDB networks achieve a significantly lower pHRR of 385 W g^{-1}. The pHRR for both these networks reduces upon introduction of the organophosphorus additives where 10 phr DMMP is more effective in reducing the pHRR than 10 phr DOPO or 17.5 phr DOPO. The reduction in the rate of degradation and pHRR reflects in heat release capacity and total heat release of these networks, as shown in Figure 4.20.

(a)

(b)
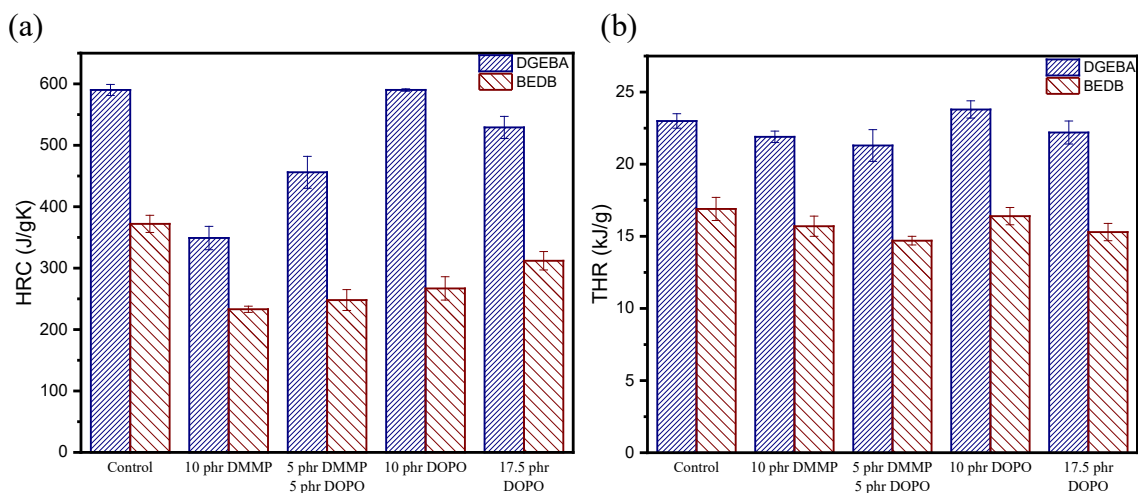
Figure 4.20 a) Heat release capacity and b) total heat release, determined by MCC, for aliphatic epoxy networks containing DMMP and DOPO

Impressively, the HRC of BEDB epoxy networks is ~35% lower than the DGEBA based epoxy networks. The HRC and THR of both networks decrease with the incorporation of DMMP or DOPO. Most significant improvements in the heat release properties are achieved at 10 phr DMMP where HRC decreases from 590 J g^{-1} K^{-1} to 350 J g^{-1} K^{-1} for DGEBA networks and from 372 J g^{-1} K^{-1} to 233 J g^{-1} K^{-1} for BEDB networks. These results, as tabulated in Table 4.7, suggest that DMMP is a more effective flame retardant when compared with DOPO at similar concentrations or even at similar wt.% of phosphorus. DMMP likely acts as a gas phase flame inhibitor for aromatic epoxy networks, as discussed earlier, whereas DOPO contributes towards char formation.[162] However, aliphatic epoxy networks with highly flammable linear hydrocarbon backbone may hinder enhanced char formation.

	Additive	HRC (J/g-K)	THR (kJ/g)	Char (%)
DGEBA	Control	590	23	7.8
	10 phr DMMP	349	21.9	8
	5 phr DMMP 5 phr DOPO	456	21.3	6.5
	10 phr DOPO	590	23.8	5.3
	17.5 phr DOPO	529	22.2	4.5
BEDB	Control	372	16.9	26.6
	10 phr DMMP	233	15.7	25.8
	5 phr DMMP 5 phr DOPO	248	14.7	33
	10 phr DOPO	267	16.4	22.7
	17.5 phr DOPO	312	15.3	24.7

Table 4.7 Heat release capacity (HRC), Total heat release (THR), and Char content values measured for aliphatic DGEBA and BEDB formulations containing DMMP and DOPO.

In order to delineate the flame inhibition mechanism of DMMP in aliphatic epoxy networks, BEDB-based epoxy networks with and without DMMP were characterized using SEM. SEM imaging was performed on the epoxy samples tested using vertical burn test, as shown in Figure 4.21. The Control BEBD network shows a smooth surface, whereas the BEDB network containing DMMP exhibits a porous, cellular morphology with large (~200 um), open-walled cells. This suggests that gases volatilized during the burning process and DMMP is primarily acting as a gas phase flame retardant, even for aliphatic epoxy networks.
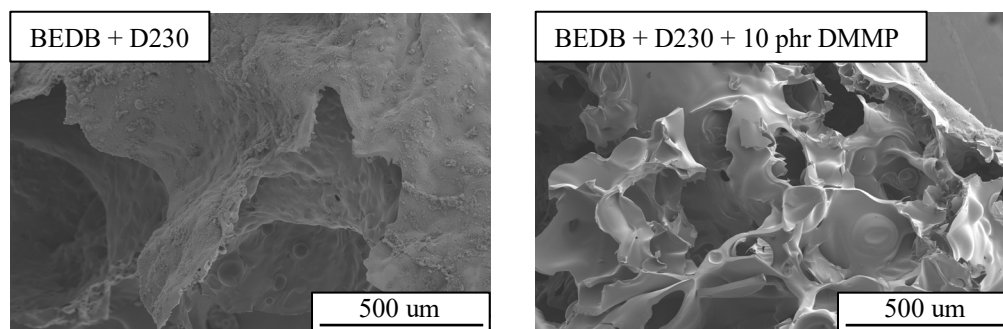
Figure 4.21 SEM images of the char formed after the vertical burn testing of (a) BEDB-based epoxy and (d) BEDB with 10 phr DMMP aliphatic networks.

Thus, unlike aromatic networks, DMMP does not enhance the char formation in aliphatic epoxy networks. Nonetheless, DMMP facilitates the gas-phase flame inhibition

mechanism to improves the heat release properties, while simultaneously enhancing the mechanical properties.

4.4   Conclusions

The investigation of different organophosphorus additives showed that dimethyl methyl phosphonate (DMMP), an organophosphorus additive, provides opportunities to afford improved mechanical and heat release properties for aromatic and aliphatic epoxy networks. The effects of the organophosphorus additive DMMP on the mechanical and heat release properties of both conventional (DGEBA) and inherently low flammability (BEDB) epoxy resins were investigated. Mechanical characterization of the DMMP-containing epoxy networks reveals characteristics of molecular fortification, showing comparable yield stress and higher elastic modulus values relative to resins lacking DMMP.   TGA measurements performed on DMMP-containing networks show char residues as high as 55% and MCC of all the DMMP-containing networks exhibit 50% lower HRC, THR, and FGC values relative to formulations without DMMP. Moreover, vertical burn tests demonstrated that DMMP-containing formulations self-extinguish quickly, without dripping. Morphological and spectroscopic analysis of the charred specimens suggests flame-retardancy via a gas-phase mechanism. Further, the incorporation of organophosphorus additive, DMMP, in aliphatic epoxy networks achieves similar enhancements in elastic modulus, yield stress, and heat release properties. Thermogravimetric and morphological analysis indicate gas-phase flame inhibition mechanisms. Overall, this organophosphorus additive represents an opportunity to combine materials chemistry with mechanical enhancement to achieve low heat release properties without the need for conventional halogenated or inorganic additives.

4.5   Future work

This chapter investigated multi-functional organophosphorus additives for fortification and flame retardance of aliphatic and aromatic epoxy networks. However, further studies are necessary to advance the understanding of these organophosphorus additives and their mechanisms of flame-retardance.

Investigation of char morphology and solid-state NMR suggests that DMMP primarily acts as a gas-phase flame retardant. Nevertheless, additional investigation using TGA-FTIR and pyrolysis GC MS can be performed. This characterization will be advantageous to understand the degradation products and pathways and will further delineate the flame-retardance mechanisms of DMMP, whether it only gas-phase or DMMP also facilitates condensed phase-char formation.

This work demonstrated that DMMP is covalently integrated with high T_g epoxy networks. Future studies are necessary to understand the precise reactions that occur during the fabrication of DMMP containing epoxy networks. This can be achieved *via* solid-state NMR investigation of epoxy networks at different curing stages. Additionally, possible reactions in the binary mixtures of epoxy and amine or epoxy and DMMP or amine and DMMP should be studied to further understand the reaction between DMMP and the matrix in a ternary composite. Solid state NMR suggests that, under the given conditions, DMMP is present in two different chemical environments. If either covalently bound phosphorus or physically trapped unbound phosphorus is more advantageous for the flame inhibition, understanding the reactions can provide opportunities to tailor epoxy networks with the

desired chemical environment for the organophosphorus additive and thereby, achieve enhanced flame retardant properties.

In addition, this chapter deals with the incorporation of phosphorus based DMMP as an additive and shows that heat release properties and mechanical properties scale with the phosphorus concentration. Future studies can focus on comparing the mechanical and flame retardant properties for epoxy composite when phosphorus is present as an additive and when phosphorus is present as a part of the epoxy network. This can be realized by synthesizing phosphorus-containing epoxy monomers or amine crosslinkers.

APPENDIX

ANALYTICAL SOLUTION FOR YIELD INITIATION AND PERCOLATION IN A POROUS MEDIA SUBJECTED TO A HYDROSTATIC STATE OF STRESS

Herein, an analytical solution is presented to describe when matrix yielding initiates, radially propagates, and eventually percolates as a function of cavity concentration. This solution assumes that the matrix yields according to a von Mises criterion and post-yield flow is fully plastic (no strain hardening). Additionally, the cavities (after rubber cavitation) are assumed to be of uniform size a and equally spaced with an interparticle spacing of $2\,b$. Finally, the loading configuration considered in this solution is pure hydrostatic tension of magnitude σ_∞ (Figure 1).
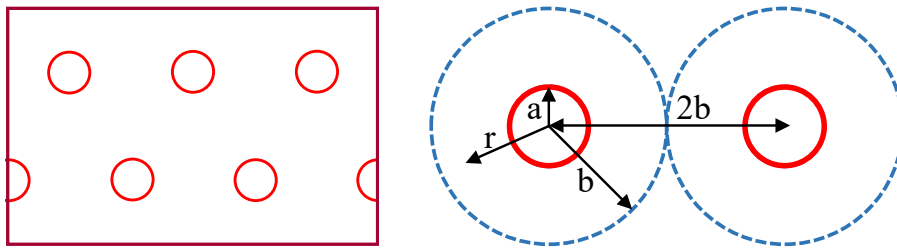
Figure A1.1 Schematic for idealized porous media with pores of uniform size a and equally spaced with an interparticle spacing of $2\,b$.

We focus on an isolated pore of size a and evaluate the condition for yield initiation to occur at the surface of the pore. In addition, when the yield fronts advance to $r = b$, a complete percolation of the yield fronts will be achieved, owing to the uniform interparticle spacing between the domains. The analytical solution is solved considering a spherical coordinate system where $r, \theta,$ and $\emptyset$ are three directions and $\sigma_r, \sigma_\theta,$ and $\sigma_\emptyset$ are corresponding stresses in the principal directions, as shown in Figure 2.

139
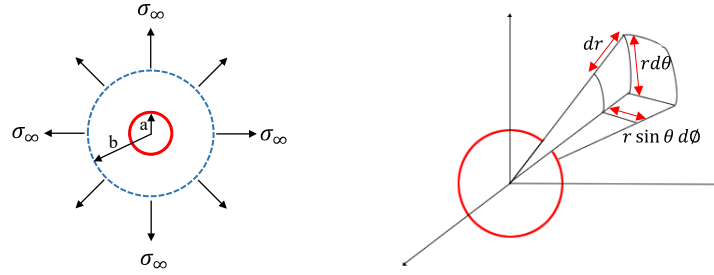
Figure A1.2 Representative volume for an isolated pore in the matrix with far-field applied stress of magnitude σ_∞ and spherical co-ordinate system with principal stresses.

A general elastic solution is considered and solved by applying the boundary conditions to determine the criterion to achieve yielding at $r = a$ and $r = b$. Equation 1 and Equation 2 represent a general elastic solution for a thick hollow sphere subjected to internal and/or external pressure in a spherical coordinate system,[210] considering the symmetry of spherical coordinates with $\sigma_\theta = \sigma_\emptyset$.

Equation 1: $\sigma_r = \frac{2}{3}\left[1 - \frac{a^3}{r^3}\right]C_1 + \frac{C_2}{r^3}$

Equation 2: $\sigma_\theta = \sigma_\emptyset = -\frac{\sigma_r}{2} + C_1$

The particular solution for given idealized porous media was determined by applying the following boundary conditions: 1) pore has a free surface at $r = a$ and consequently, radial stress (σ_r) equals to 0 and 2) at $r = b$ from the center of the pore, radial stress (σ_r) equals far-field applied stress (σ_∞).

$when\ r = a\ ;\ \sigma_r = 0 \Rightarrow C_2 = 0$ and

$when\ r = b\ ;\ \sigma_r = \sigma_\infty \Rightarrow C_1 = \left(\dfrac{\frac{3}{2}\sigma_\infty}{1 - \dfrac{a^3}{b^3}}\right)$

Substituting the determined constants C_1 and C_2, the generalized solution reduces to a particular solution, as per Equation 3 and Equation 4.

140

Equation 3: $\sigma_r = \sigma_\infty \dfrac{\left(1-\frac{a^3}{r^3}\right)}{\left(1-\frac{a^3}{b^3}\right)}$

Equation 4: $\sigma_\theta = \dfrac{\sigma_\infty}{2}\dfrac{\left(2+\frac{a^3}{r^3}\right)}{\left(1-\frac{a^3}{b^3}\right)}$

von Mises criterion predicts that material yields when the distortion energy reaches a critical value. Although it is widely used in the prediction of both metals and many polymer applications, it is known that a modified von Mises criterion is more appropriate for polymers. That said, since the hydrostatic stress is relieved by cavitation, a simple von Mises criterion should provide a reasonable estimate of yielding in the case of porous polymeric materials. The matrix yield criterion was determined by applying a von Mises yield criterion, as shown in Equation 5 for principle stresses in a spherical coordinate system. Equations 6 and 7 indicate results for the case of pure hydrostatic tension.

Equation 5: $\sigma_y^2 = \dfrac{1}{2}[(\sigma_r - \sigma_\theta)^2 + (\sigma_\theta - \sigma_\emptyset)^2 + (\sigma_\emptyset - \sigma_r)^2]$

Equation 6: $\sigma_y^2 = (\sigma_r - \sigma_\theta)^2$

Equation 7: $\sigma_y = |\sigma_r - \sigma_\theta|$

To further simplify these equations, dimensionless quantities p, ρ, β, S_r, and S_θ are introduced. p is defined as the ratio of far-field applied stress σ_∞ with the yield stress σ_y, β is defined as the ratio of half of the interparticle spacing (b) with the radius of each pore (a), and ρ is a dimensionless variable described as the ratio of r (radial distance from the center of a pore) to a (radius of the pore) and ranges from 1 to $\dfrac{b}{a}$ (β). S_r and S_θ are dimensionless variables defined as the ratio of σ_r and σ_θ (principle stresses) with the yield stress σ_y, respectively. Substitution of these defined dimensionless quantities reduces Equation 3 and 4 to Equation 8 and 9, respectively.

$$p = \frac{\sigma_\infty}{\sigma_y}; \ \rho = \frac{r}{a}; \ \beta = \frac{b}{a}; \ S_r = \frac{\sigma_r}{\sigma_y}; \ S_\theta = \frac{\sigma_\theta}{\sigma_y}$$

Equation 8: $S_r = p \frac{\left(1-\frac{1}{\rho^3}\right)}{\left(1-\frac{1}{\beta^3}\right)} = p \frac{\beta^3}{\rho^3} \frac{(\rho^3-1)}{(\beta^3-1)}$

Equation 9: $S_\theta = \frac{p}{2} \frac{\left(2+\frac{1}{\rho^3}\right)}{\left(1-\frac{1}{\beta^3}\right)} = \frac{p}{2} \frac{\beta^3}{\rho^3} \frac{(2\rho^3+1)}{(\beta^3-1)}$

The concentration of pores is defined as the relative ratio of pore volume with the total volume of the matrix and pores, as shown in Equation 10.

Equation 10: $c = \left(\frac{\frac{4}{3}\pi a^3}{\frac{4}{3}\pi b^3}\right) = \frac{1}{\beta^3}$

Substituting the dimensional quantities, Equation 7 simplifies to Equation 11.

Equation 11: $|S_r - S_\theta| = 1$

- Yield initiation at $r = a$

Yield initiation criterion is evaluated by substituting $r = a$ in Equation 11 and solving the resulting equation (steps as shown in Equation 12 and Equation 13) gives Equation 14 which shows that the far-field stress (applied stress) required for the yield initiation decreases linearly with the concentration of cavities.

Equation 12: $|S_\theta| = 1$

Equation 13: $p = \frac{2}{3}\left(\frac{\beta^3-1}{\beta^3}\right)$

Equation 14: $\sigma_\infty = \frac{2}{3}\sigma_y[1-c]$

Further, for the case of an isolated pore in an infinite media ($c \rightarrow 0$), Equation 14 reduces to $\sigma_\infty = \frac{2}{3}\sigma_y$ and Equation 9 reduces to $\sigma_\theta = \frac{3}{2}\sigma_\infty$. These results suggest that even

142

a single isolated pore or cavitated rubber particle in the matrix results in the stress concentration at the surface of the pore and significantly decreases the far-field stress required for the yield initiation.

- Yield percolation at $r = b$

Equation 15 shows the equilibrium equation for a spherical coordinate system, arrived at by solving the field equations of elasticity including kinematic, compatibility, and constitutive equations.

Equation 15: $\frac{d\sigma_r}{dr} + \frac{2(\sigma_r - \sigma_\theta)}{r} = 0$

The equilibrium equation simplifies to Equation 18 by using the dimensionless quantities (Equation 17 and Equation 18) and by recalling the von Mises yield criterion (Equation 11).

Equation 16: $\frac{dS_r}{d\rho} + \frac{2(S_r - S_\theta)}{\rho} = 0$

Equation 17: $\frac{dS_r}{d\rho} = \frac{2(S_\theta - S_r)}{\rho}$

Equation 18: $\frac{dS_r}{d\rho} = \frac{2}{\rho}$

This differential equation is integrated to arrive at Equation 19, followed by applying the boundary conditions (Equation 20), the criterion for yield percolation is determined, as shown in Equation 21.

Equation 19: $S_r = 2\ln\rho + C_3$

$when\ r = a\ ;\ S_r = 0 \Rightarrow C_3 = 0$

Equation 20: $S_r = 2\ln\rho$

Equation 21: $\sigma_\infty = 2\sigma_y \ln c^{\frac{-1}{3}}$

143
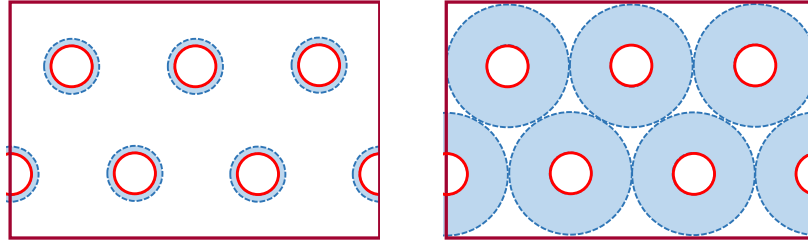
Figure A1.3 Schematic for yield initiation and yield percolation in porous media, respectively.

The analytical solution for the idealized system shows that the far-field stress (applied stress) required for yield initiation decreases linearly with the concentration, whereas stress required for yield percolation decreases logarithmically with the concentration of pores, as shown in Figure 4. At high concentrations, it is possible to achieve complete yield percolation at stresses lower than the yield stress of polymer matrix, indicating the advantages of introducing cavities or pores for energy absorption. Therefore, optimizing the pore concentration provide opportunities to maximize the matrix yielding and improve the impact properties.

Figure A1.4 Applied stress as a function of rubber concentration required for yield initiation and yield percolation, estimated using Equation 14 and Equation 21.

144

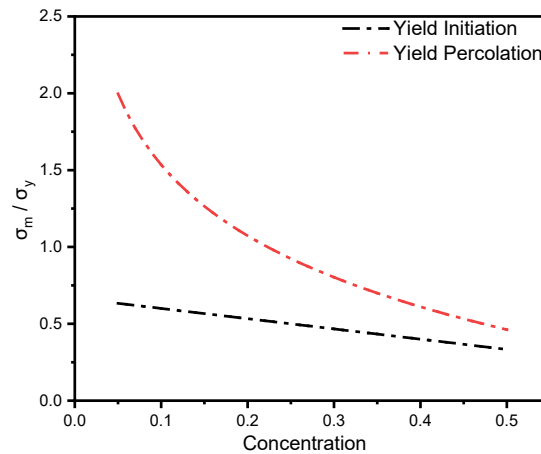| Block copolymer	Commercial Name	Composition
PE-PEO	PE-PEO	M_n~575, PEO 20%
	Brij 93	M_n~357, PEO 29%
	Brij L4	M_n~362, PEO 49%
	Brij S10	M_n~711, PEO 62%
	Brij S20	M_n~1152, PEO 76%
	PE-PEO	M_n~2250, PEO 80%
PEO-hexadecyl ether	Brij C10	M_n~683, PEO 64%
PEO-nonylphenyl ether	IGEPAL CO-720	M_n~749, PEO 70%
PEO-oleyl ether	Brij O20	M_n~1150, PEO 77%
PDMS-[65-70%(60%PPO-40%PEO)]	DBP 732	$M_w = 20,000$
PDMS-PEO	DBE-814	M_w~1,000, PEO 80%
	DBE-712	M_w~600, PEO 60-70%
	DBE-411	M_w~400-500, PEO 45-50%
	DBE-921	M_w~5,000, PEO 85-90%
	DBE-621	M_w~2,500, PEO 50-55%
	DBE-311	M_w~800-1,200, PEO 30-35%
	DBE-224	M_w~10,000, PEO 25-30%
PS-PB-PMMA	SBM	
PEO-PPO-PEO	PEO-PPO-PEO	M_n~5,800, PEO 30%
	PEO-PPO-PEO	M_n~14,600, PEO 82.5%
	PEO-PPO-PEO	M_n~2,800, PEO 10%
	PEO-PPO-PEO	M_n~1,900, PEO 50%
PCL-PTHF-PCL	PCL-PTHF-PCL	M_n~2,000
Polylauryllactam-PTHF	Polylauryllactam-PTHF	
PMMA-PBuA-PMMA	M51	
	M52	
	M53	
PEO-PPO-PDMS-PVMS	DBP-V102	M_w 9,000~12,000
Carbinol(-OH) terminated PDMS	DBE-C25	M_w 3,500~4,500
Acryloxyl terminated PDMS	DBE-U12	M_w 1,500~1,600

Table A2.1 Commercial grades and compositions corresponding to homopolymers and block-copolymers used as additives in stereolithographic resin formulations.
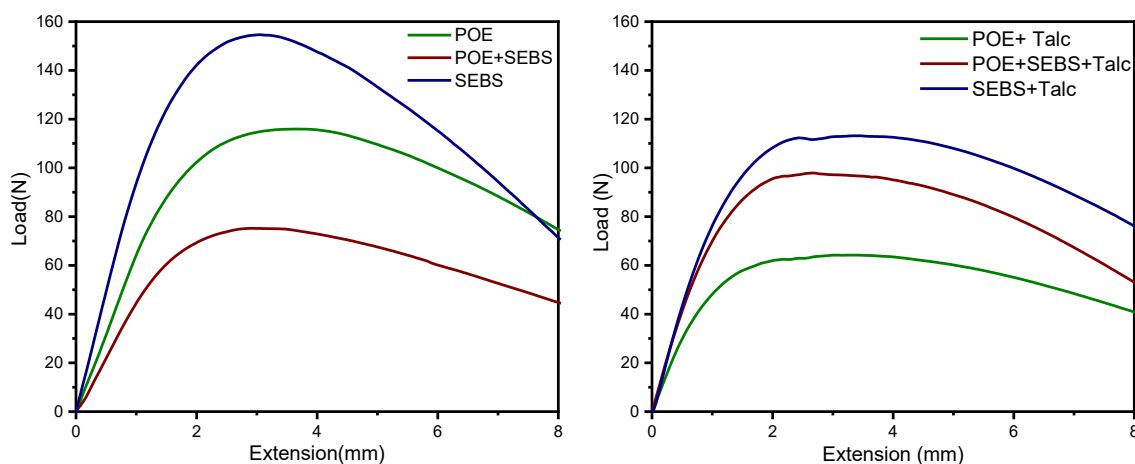
Figure A3.1 Representative load versus extension curves for polypropylene formulations generated during quasi-static SENB testing at room temperature.
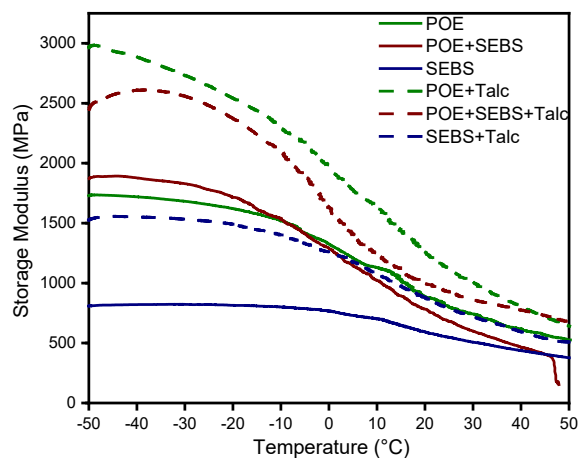
Figure A3.2 Representative storage modulus versus temperature curves for polypropylene formulations generated using DMA.
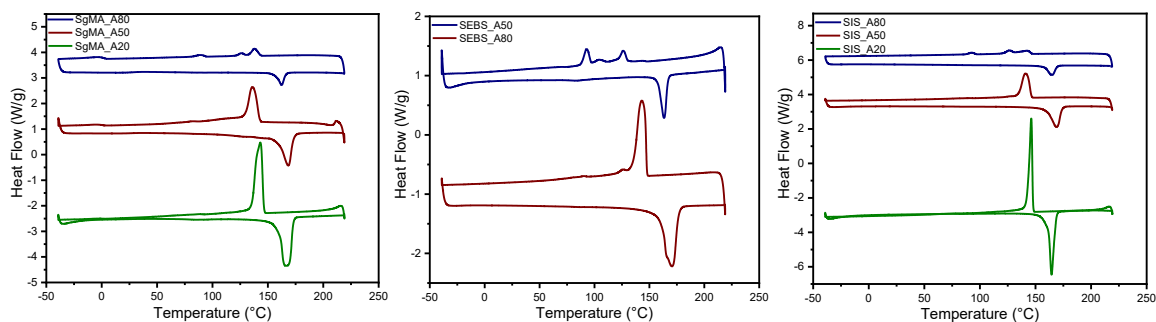

Figure A3.3 DSC thermographs for elastomeric adducts of SEBS-*g*-MA, SEBS, and SIS, respectively.
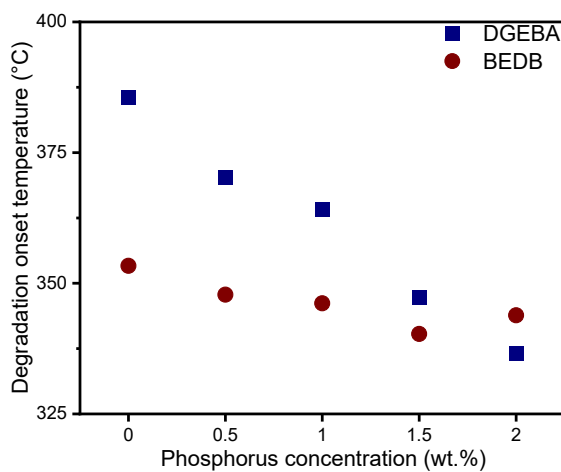

Figure A4.1 Degradation onset temperature (corresponding to 5 wt.% weight loss) for DGEBA- and BEDB-based networks.

BIBLIOGRAPHY

1. S. Al-Malaika, A. Golovoy, and C.A. Wilkie, *Chemistry and technology of polymer additives*, Oxford1999.
2. J.E. Kresta, *Polymer Additives*, New York :Plenum Press1984.
3. S. Clark, in *Allied Market Research*2014.
4. V. Ambrogi, et al., in *Modification of Polymer Properties*, Elsevier2017, pp 87-108.
5. A.J. Kinloch and R.J. Young, *Fracture Behaviour of Polymers*1995.
6. G.R. Irwin, *Trans. ASME, Ser. E, J. Appl. Mech.*, **24**, 361 (1957).
7. H.M. WESTERGAARD, *Journal of Applied Mechanics*, **6**, 49 (1939).
8. D.S. Dugdale, *Journal of the Mechanics and Physics of Solids*, **8**, 100 (1960).
9. G. Barenblatt, *Advances in Applied Mechanics*, **7**, 56 (1962).
10. S. Humbert, O. Lame, and G. Vigier, *Polymer*, **50**, 3755 (2009).
11. A.T. Detwiler and A.J. Lesser, *Journal of Materials Science*, **47**, 3493 (2012).
12. E.D. Crawford and A.J. Lesser, *Polymer Engineering & Science*, **39**, 385 (1999).
13. F.O.M.S. Abreu, M.M.C. Forte, and S.A. Liberman, *Journal of Applied Polymer Science*, **95**, 254 (2005).
14. A.K. Bandaru, et al., *International Journal of Impact Engineering*, **93**, 136 (2016).
15. A. Elloumi, S. Pimbert, and C. Bradai, *Journal of Composite Materials*, **50**, 985 (2016).
16. C. Fang, et al., *Materials Research Express*, **5**, 055307 (2018).
17. S.C. Tjong, et al., *Composites Science and Technology*, **62**, 831 (2002).
18. D. Dompas and G. Groeninckx, *Polymer*, **35**, 4743 (1994).
19. A. Lazzeri and C.B. Bucknall, *Journal of Materials Science*, **28**, 6799 (1993).
20. A.J. Kinloch and Y. Huang, *Journal of Materials Science*, **27**, 2753.
21. C. Bucknall, *Toughened Plastics*1977.
22. B.P. Panda, S. Mohanty, and S.K. Nayak, *Polymer-Plastics Technology and Engineering*, **54**, 462 (2015).
23. A. van der Wal and R.J. Gaymans, *Polymer*, **40**, 6067 (1999).
24. W. Tang, et al., *Journal of Applied Polymer Science*, **122**, 461 (2011).
25. J. Liu, et al., *Macromolecules*, **43**, 7238 (2010).
26. R. He, et al., *Journal of Applied Polymer Science*, **134**, 44849 (2017).
27. S. Wu, *Polymer*, **26**, 1855 (1985).
28. R.J.M. Borggreve, et al., *Polymer*, **28**, 1489 (1987).
29. C.B. Bucknall, *Journal of Polymer Science Part B: Polymer Physics*, **45**, 1399 (2007).
30. M. Helbig, et al., *European Journal of Mechanics - A/Solids*, **57**, 108 (2016).
31. H.-J. Sue, *Journal of Materials Science*, **27**, 3098 (1992).
32. B.Z. Jang, D.R. Uhlmann, and s. Vander, *Polymer Engineering and Science*, **25** (1985).
33. A.M. Donald and E.J. Kramer, *Journal of Applied Polymer Science*, **27**, 3729 (1982).
34. C.J. McCutcheon, et al., *Macromolecules*, **53**, 10163 (2020).
35. D.A. Norman and R.E. Robertson, *Polymer*, **44**, 2351 (2003).

36. A.G. Evans, *The Philosophical Magazine: A Journal of Theoretical Experimental and Applied Physics*, **26**, 1327 (1972).
37. J. Lee and A.F. Yee, *Polymer*, **42**, 589 (2001).
38. H.J. Sue, et al., *Colloid and Polymer Science*, **274**, 342 (1996).
39. Y.S. Thio, et al., *Polymer*, **43**, 3661 (2002).
40. Y.S. Thio, A.S. Argon, and R.E. Cohen, *Polymer*, **45**, 3139 (2004).
41. I.L. Dubnikova, S.M. Berezina, and A.V. Antonov, *Journal of Applied Polymer Science*, **94**, 1917 (2004).
42. J. Lee, *Polymer*, **41**, 8363 (2000).
43. W.Y. Jung and J.I. Weon, *Journal of Materials Science*, **48**, 1275 (2013).
44. S.M. Zebarjad, M. Tahani, and S.A. Sajjadi, *Journal of Materials Processing Technology*, **155-156**, 1459 (2004).
45. Z. Bartczak, et al., *Polymer*, **40**, 2347 (1999).
46. H. Yang, et al., *Polymer*, **47**, 2106 (2006).
47. J.-Y. Lee, J. An, and C.K. Chua, *Applied Materials Today*, **7**, 120 (2017).
48. P. Stavropoulos and P. Foteinopoulos, *Manufacturing Review*, **5**, 2 (2018).
49. J.R.C. Dizon, et al., *Additive Manufacturing*, **20**, 44 (2018).
50. X. Wang, et al., *Composites Part B: Engineering*, **110**, 442 (2017).
51. S.C. Ligon, et al., *Chemical Reviews*, **117**, 10212 (2017).
52. S.C. Ligon-Auer, et al., *Polymer Chemistry*, **7**, 257 (2016).
53. V.O.E. Väyrynen, J. Tanner, and P.K. Vallittu, *The Journal of Prosthetic Dentistry*, **116**, 811 (2016).
54. J.Z. Manapat, et al., *Macromolecular Materials and Engineering*, **302**, 1600553 (2017).
55. D. Arencón and J.I. Velasco, *Materials*, **2**, 2046 (2009).
56. D. Lin, et al., *Nanotechnology*, **26**, 434003 (2015).
57. U. Kalsoom, et al., *RSC Advances*, **6**, 38140 (2016).
58. Z. Weng, et al., *Composites Part A: Applied Science and Manufacturing*, **88**, 234 (2016).
59. Y. Li, et al., *Chemical Engineering Journal*, **394**, 124873 (2020).
60. J. Guit, et al., *ACS Applied Polymer Materials*, **2**, 949 (2020).
61. R. Bagheri and R.A. Pearson, *Polymer*, **41**, 269 (2000).
62. R. Bagheri, B.T. Marouf, and R.A. Pearson, *Polymer Reviews*, **49**, 201 (2009).
63. F.J. Guild, A.J. Kinloch, and A.C. Taylor, *Journal of Materials Science*, **45**, 3882 (2010).
64. C. Declet-Perez, L.F. Francis, and F.S. Bates, *Macromolecules*, **48**, 3672 (2015).
65. C.B. Bucknall, D.S. Ayre, and D.J. Dijkstra, *Polymer*, **41**, 5937 (2000).
66. W. Heckmann, G.E. McKee, and F. Ramsteiner, *Macromolecular Symposia*, **214**, 85 (2004).
67. P. Vijayan P, et al., *Materials Science and Engineering: R: Reports*, **116**, 1 (2017).
68. A.S. D5045, ASTM International.
69. C.Y.C. Lee and W.B. Jones, *Polymer Engineering and Science*, **22**, 1190 (1982).
70. J.A. Hinkley, *Journal of Applied Polymer Science*, **32**, 5653 (1986).
71. M. Gurr, et al., *Advanced Functional Materials*, **18**, 2390 (2008).
72. N. Li, et al., *Materials Research Express*, **5**, 085306 (2018).
73. L.M. Robeson, *Polymer blends: a comprehensive review*, Hanser, Munich, 2007.

74. J. Liu, et al., *Macromolecules*, **41**, 7616 (2008).
75. J. Zhu, et al., *Nature Communications*, **4**, 2297 (2013).
76. A. Cho, et al., *Macromolecules*, **50**, 3234 (2017).
77. G.C. Evans, P. Desbois, and A.J. Lesser, *Journal of Applied Polymer Science*, **135**, 46823 (2018).
78. C.B. Bucknall and D.R. Paul, *Polymer*, **50**, 5539 (2009).
79. R. Bagheri and R.A. Pearson, *Polymer*, **37**, 10 (1996).
80. A.S. D6068, ASTM International.
81. C.B. Bucknall, et al., *Macromolecular Symposia*, **101**, 265 (1996).
82. K. Chockalingam, et al., *The International Journal of Advanced Manufacturing Technology*, **29**, 79 (2006).
83. D. Ambrosio, et al., *The International Journal of Advanced Manufacturing Technology*, **106**, 265 (2020).
84. N. Alharbi, et al., *Materials Technology*, **34**, 12 (2019).
85. F. Meng, S. Zheng, and T. Liu, *Polymer*, **47**, 7590 (2006).
86. R. Francis and D.K. Baby, *Colloid and Polymer Science*, **294**, 565 (2016).
87. J.F.M. Mirabella and J.S. Barley, *Journal of Polymer Science Part B: Polymer Physics*, **32**, 2187 (1994).
88. M. Pawar, UMass Amherst2018, Vol. Ph.D.
89. I. Blaszczyk-Lezak, M. Hernández, and C. Mijangos, *Macromolecules*, **46**, 4995 (2013).
90. J.C. Lötters, et al., *Journal of Micromechanics and Microengineering*, **7**, 145 (1997).
91. L. Yao, et al., *Journal of Applied Polymer Science*, **134** (2017).
92. P. Jia, et al., *Journal of Cleaner Production*, **206**, 838 (2019).
93. R. Alasfar, et al., *Journal of Applied Polymer Science*, **137**, 49545 (2020).
94. H.G.H. van Melick, L.E. Govaert, and H.E.H. Meijer, *Polymer*, **44**, 2493 (2003).
95. K. Chockalingam, et al., 10.
96. H.G.H. van Melick, L.E. Govaert, and H.E.H. Meijer, *Polymer*, **44**, 3579 (2003).
97. R.N. Haward, *Polymer*, **28**, 4 (1987).
98. A.T. Detwiler and A.J. Lesser, *Journal of Applied Polymer Science*, **117**, 1021 (2010).
99. P.R. Ware and A.J. Lesser, *Journal of Applied Polymer Science*, **131**, n/a (2014).
100. J. Janzen, *Polymer Engineering and Science*, **32**, 1242 (1992).
101. J.-Z. Liang and F. Wang, *Polymer Bulletin*, **72**, 915 (2015).
102. Y. Chen, et al., *Polymer Engineering & Science*, **59**, 757 (2019).
103. J.C. Halpin and J.L. Kardos, *Journal of Applied Physics*, **43**, 2235 (1972).
104. C.Y. Li, *Polymer*, **211**, 14 (2020).
105. P.A. Moysey and M.R. Thompson, *Chemical Engineering Science*, **62**, 3699 (2007).
106. P.A. Klonos, et al., *Soft Matter*, **15**, 1813 (2019).
107. N. Uthaman, A. Majeed, and Pandurangan, *e-Polymers*, **6** (2006).
108. C.J. Christopher, et al., *International Journal of Fracture*, **148**, 361 (2007).
109. J.Z. Liang and R.K.Y. Li, *Journal of Applied Polymer Science*, **77**, 409 (2000).
110. F. Chen, et al., *Polymer*, **65**, 81 (2015).
111. E. Jia, et al., *Journal of Applied Polymer Science*, **135**, 45714 (2018).

112. J. Richeton, et al., *Polymer*, **46**, 6035 (2005).
113. B. Lotz, J.C. Wittmann, and A.J. Lovinger, *Polymer*, **37**, 4979 (1996).
114. S.C. Tjong, J.S. Shen, and R.K.Y. Li, *Polymer*, **37**, 8 (1996).
115. J.Z. Liang and R.K.Y. Li, *2000*, **77**, 409.
116. J. Xu, V. Mittal, and F.S. Bates, *Macromolecules*, **49**, 6497 (2016).
117. A.N. Wilkinson, M.L. Clemens, and V.M. Harding, *Polymer*, **45**, 5239 (2004).
118. N. Fanegas, et al., *Polymer Engineering & Science*, **48**, 80 (2008).
119. Q.-X. Zhang, et al., *Polymer*, **45**, 5985 (2004).
120. J.I. Weon, et al., *Journal of Applied Polymer Science*, **99**, 3070 (2006).
121. R.H. Olley, A.M. Hodge, and D.C. Bassett, *Journal of Polymer Science: Polymer Physics Edition*, **17**, 627 (1979).
122. R.H. Olley, *Science Progress (1933-)*, **70**, 17 (1986).
123. F. Luo, et al., *Macromolecules*, **42**, 9325 (2009).
124. H. Du, et al., *Polymer*, **55**, 5001 (2014).
125. K. Trongtorsak, P. Supaphol, and S. Tantayanon, *Polymer Testing*, **23**, 533 (2004).
126. F.X. Espinach, et al., *Composites Part B: Engineering*, **47**, 339 (2013).
127. A.N. Wilkinson, et al., *Polymer*, **40**, 4971 (1999).
128. Z. Cheng and Q. Wang, *Polymer International*, **55**, 1075 (2006).
129. T.J. Hermel-Davidock, et al., *Journal of Polymer Science Part B: Polymer Physics*, **45**, 3338 (2007).
130. H.G.B. Premalal, H. Ismail, and A. Baharin, *Polymer Testing*, **21**, 833 (2002).
131. Y.W. Leong, et al., *Journal of Applied Polymer Science*, **91**, 3315 (2004).
132. W. Qiu, K. Mai, and H. Zeng, *Journal of Applied Polymer Science*, **77**, 4 (2000).
133. J.-Z. Liang, *Journal of Applied Polymer Science*, **83**, 1547 (2002).
134. R.J.M. Borggreve, R.J. Gaymans, and J. Schuijer, *Polymer*, **30**, 71 (1989).
135. X.c. Ren, et al., *Journal of Macromolecular Science, Part B*, **46**, 411 (2007).
136. X. Guo, J. Zhang, and J. Huang, *Polymer*, **69**, 103 (2015).
137. M. Berer, G. Pinter, and M. Feuchter, *Journal of Applied Polymer Science*, **131**, n/a (2014).
138. P. Liu and S. Bai, *Journal of Vinyl and Additive Technology*, **24**, 147 (2018).
139. W.-J. Sun, et al., *ACS Applied Polymer Materials*, **1**, 2741 (2019).
140. K.L. Lam, A.A. Bakar, and Z.A.M. Ishak, *Polymer Engineering & Science*, **45**, 710 (2005).
141. Y. Liu, et al., *Polymers for Advanced Technologies*, **25**, 760 (2014).
142. W. Yang, et al., *Polymer Engineering & Science*, **58**, 1127 (2018).
143. J. Qiu, et al., *Macromolecules*, **46**, 5806 (2013).
144. S.-J. Kim, et al., *Polymer*, **42**, 4073 (2001).
145. M. Mari and C.W. Macosko, *Journal of Polymer Science Part B: Polymer Physics*, **40**, 346 (2002).
146. J. Zhang, T.P. Lodge, and C.W. Macosko, *Macromolecules*, **38**, 6586 (2005).
147. H. Li and X.-M. Xie, *Polymer*, **108**, 1 (2017).
148. S. Wacharawichanant, P. Amorncharoen, and R. Wannasirichoke, *Advanced Materials Research*, **1052**, 220 (2014).
149. J.C.H. Affdl and J.L. Kardos, *Polymer Engineering and Science*, **16**, 344 (1976).
150. S. Joseph and S. Thomas, *Journal of Polymer Science Part B: Polymer Physics*, **40**, 755 (2002).

151. B. Bilyeu, W. Brostow, and K.P. Menard, *Journal of Materials Education*, **21**, 281 (1999).
152. Y.L. Liu, *Polymer*, **42**, 3445 (2001).
153. W. Zhang, X. Li, and R. Yang, *Polymer Degradation and Stability*, **96**, 2167 (2011).
154. R.M. Perez, et al., *Journal of Materials Science*, **41**, 341 (2006).
155. Z. Weng, et al., *Journal of Applied Polymer Science*, **133**, 43367 (2016).
156. A. Dasari, et al., *Progress in Polymer Science*, **38**, 1357 (2013).
157. F. Laoutid, et al., *Materials Science and Engineering: R: Reports*, **63**, 100 (2009).
158. R.E. Lyon and T. Emrick, *Polymers for Advanced Technologies*, **19**, 609 (2008).
159. R.E. Lyon, N. Safronava, and R.N. Walters, in *UMass CUMIRP*2019.
160. G. Chai, et al., *Advanced Composites Letters*, **28** (2019).
161. B. Schartel, et al., *Journal of Applied Polymer Science*, **104**, 2260 (2007).
162. B. Schartel, et al., *European Polymer Journal*, **44**, 704 (2008).
163. U. Braun, et al., *Polymer*, **47**, 8495 (2006).
164. M. Hussain, et al., *Journal of Applied Polymer Science*, **91**, 1233 (2004).
165. S. Yang, et al., *Polymer Degradation and Stability*, **115**, 63 (2015).
166. C.-Q. Wang, et al., *Polymer Engineering & Science*, **54**, 2497 (2014).
167. W. Xu, G. Wang, and X. Zheng, *Polymer Degradation and Stability*, **111**, 142 (2015).
168. H. Zhi, et al., *Journal of the Chinese Institute of Engineers*, **38**, 93 (2015).
169. S. Liu, et al., *RSC Advances*, **6**, 5288 (2016).
170. H. Yang, et al., *Polymers for Advanced Technologies*, **29**, 2917 (2018).
171. X. Chen, J. Li, and M. Gao, *Polymers*, **11**, 78 (2019).
172. A.S. Zerda and A.J. Lesser, *Journal of Applied Polymer Science*, **84**, 302 (2002).
173. R.A. Riggleman, J.F. Douglas, and J.J. de Pablo, *The Journal of Chemical Physics*, **126**, 234903 (2007).
174. W.J. Jackson and J.R. Caldwell, *Journal of Applied Polymer Science*, **11**, 211 (1967).
175. A.J. Lesser, K. Calzia, and M. Junk, *Polymer Engineering & Science*, **47**, 1569 (2007).
176. A.S. Zerda and A.J. Lesser, *Polymer Engineering and Science*, **44**, 2125 (2004).
177. C.F. Kins, G. Brunklaus, and H.W. Spiess, *Macromolecules*, **46**, 2067 (2013).
178. B.-Y. Ryu, et al., *Polymer*, **50**, 767 (2009).
179. M.W. Szyndler, et al., *Polymer*, **55**, 4441 (2014).
180. L. Zhang, et al., *RSC Advances*, **5**, 87609 (2015).
181. X. Hu, et al., *Journal of Applied Polymer Science*, **135**, 45904 (2018).
182. X. Hu, et al., *Journal of Applied Polymer Science*, **134**, 455370 (2017).
183. D7309-19A, ASTM International.
184. D3801, ASTM International.
185. R. Ganguly, et al., *Polymer*, **116**, 27 (2017).
186. A. Jumahat, et al., *Journal of Materials Science*, **45**, 5973 (2010).
187. T. da Costa Dias, et al., *Materials Today: Proceedings*, **8**, 847 (2019).
188. K.J. Calzia and A.J. Lesser, *Journal of Materials Science*, **42**, 5229 (2007).
189. R.A.C. Deblieck, et al., *Polymer*, **52**, 2979 (2011).
190. C.F. Kins, et al., *Macromolecules*, **43**, 7200 (2010).

191. M.J.P. Harger, *Journal of the Chemical Society, Perkin Transactions* 2699 (1983).
192. A. Chworoś and L.A. Woźniak, *Tetrahedron Letters*, **40**, 9337 (1999).
193. A.K. Gupta, et al., *Journal of Chemical Research*, 328 (2007).
194. M. Bujard, V. Gouverneur, and C. Mioskowski, *The Journal of Organic Chemistry*, **64**, 2119 (1999).
195. E1641, ASTM International.
196. Y. Li, et al., *RSC Advances*, **9**, 3128 (2019).
197. J.M. Cogen, T.S. Lin, and R.E. Lyon, *Fire and Materials*, **33**, 33 (2009).
198. H. Guo, R.E. Lyon, and N. Safronava, *Journal of Testing and Evaluation*, **46**, 1090 (2018).
199. R.E. Lyon and R.N. Walters, *Journal of Analytical and Applied Pyrolysis*, **71**, 27 (2004).
200. R.E. Lyon, N. Safronava, and R.N. Walters.
201. R.E. Lyon, et al., *Polymer Degradation and Stability*, **186**, 109478 (2021).
202. S. Bourbigot and S. Duquesne, *Journal of Materials Chemistry*, **17**, 2283 (2007).
203. A.S. D, ASTM International.
204. S.V. Levchik and E.D. Weil, *Journal of Fire Sciences*, **24**, 345 (2006).
205. Z. Huang and W. Shi, *Polymer Degradation and Stability*, **92**, 1193 (2007).
206. B. Schartel, *Materials*, **3**, 4710 (2010).
207. K.A. Salmeia and S. Gaan, *Polymer Degradation and Stability*, **113**, 119 (2015).
208. P. Wang, L. Chen, and H. Xiao, *Journal of Analytical and Applied Pyrolysis*, **139**, 104 (2019).
209. C. Saraf, et al., *Macromolecular Materials and Engineering*, **306**, 2000567 (2020).
210. S. Timoshenko, *Theory of elasticity*, McGraw-Hill1951.